THESIS FOR THE DEGREE OF DOCTOR OF PHILOSOPHY

Nanostructures of Graphite and Amorphous Carbon - Fabrication and Properties

Hans Fredriksson

Department of Applied Physics
CHALMERS UNIVERSITY OF TECHNOLOGY
Göteborg, Sweden 2009

Nanostructures of Graphite and Amorphous Carbon -
Fabrication and Properties

ISBN 978-91-7385-307-1

Doktorsavhandlingar vid Chalmers tekniska högskola
Ny serie nr 2988
ISSN 0346-718X

Department of Applied Physics
Chalmers University of Technology
SE-412 96 Göteborg
Sweden
Telephone + 46 (0)31-772 1000

Cover:
Optical extinction spectra from amorphous carbon nanostructures with decreasing sizes and SEM images of nanostructured graphite samples with three different feature sizes.

Printed at Chalmers Reproservice

Göteborg, Sweden 2009

ABSTRACT

Nanoscience is a well-established research area, which concerns properties and fabrication of objects with typical dimensions on the 1-100 nanometer length scale. A central issue has been the development of techniques for fabrication and characterization of nanometer sized objects, which have contributed considerably to progress in both practical applications and fundamental research. Still, a standing challenge in nanofabrication is to further decrease the size limit and increase the precision in structure fabrication, with a simultaneous increase in reliability and cost-efficiency. Other goals are to facilitate fabrication of nanostructures in a variety of materials, with different geometries and spatial distributions. Examples of practical applications of nanofabrication are, electronic devices, nanoparticle reinforced composite materials, materials for extraction and storage of energy, sensors and biomedical applications.

In this thesis, the development and application of a nanofabrication technique termed hole-mask colloidal lithography (HCL) is described. The technique is based on self-assembly of nanospheres in combination with spin coating and thin film evaporation to produce supported nanostructured masks for etch and/or deposition processes. HCL relies on a parallel process and uses relatively simple laboratory equipment. Therefore it is fast and cost-effective and can be used to structure large surface areas in a reasonable time. Furthermore, HCL is suited for fabrication of nanostructures with a variety of different shapes, with well-defined sizes and in a large variety of different materials. Demonstrated examples include discs, ellipses, bi-metallic particle pairs, cones and inverted ring structures in Au, Ag, Cr. Specifically, the use of HCL to fabricate nanostructures in three different carbon materials, highly oriented pyrolytic graphite (HOPG), glassy carbon (GC) and amorphous carbon, is described. Such nanostructured materials are relevant both in technical applications and in model studies of e.g. soot particles. The manufactured nanostrucutres have been characterized with respect to their geometrical, mechanical, and optical properties, using microscopy and spectroscopy techniques, and their reactivity towards oxidation has been explored.

From studies of such samples, it is concluded that the etch rate in oxygen plasma is different for HOPG and GC, which influences the resulting size and shape of the nanostructures after the applied oxidation treatment. It is also shown that the atomic arrangement of the HOPG nanostructures is similar to that of the bulk material. Investigations of the optical properties reveal resonant absorption and scattering of light for nanostructures in all three materials, i.e. peak position, amplitude and width of the measured optical spectra are shown to correlate with the nanostructure sizes. This correlation is used to optically monitor oxidation, and the resulting decrease in volume, of carbon nanostructures under high temperature oxidation conditions and is proposed as a general sensing method to study oxidation/combustion of soot and other carbon nanostructures.

Keywords: Nanofabrication, carbon, HOPG, GC amorphous carbon, oxidation, optical resonance, optical spectrum, Raman spectrum.

LIST OF PUBLICATIONS

This thesis is based on the work contained in the following papers:

Paper I. Hole-mask colloidal lithography
H. Fredriksson, Y. Alaverdyan, A. Dmitriev, C. Langhammer, D. S. Sutherland, M. Zäch and B Kasemo
Advanced Materials, 2007. **19** (23): p. 4297

Paper II. Patterning of highly oriented pyrolytic graphite and glassy carbon surfaces by nanolithography and oxygen plasma etching
H. Fredriksson, D, Chakarov and B. Kasemo
Carbon, 2009. **47:** p. 1335

Paper III. Resonant optical absorption in graphite nanostructures
H. Fredriksson, T. Pakizeh, M. Käll, B. Kasemo and D. Chakarov
Journal of Optics A; Pure and applied Optics, 2009. **11,** in press

Paper IV. Raman spectroscopy of nanostructured graphite
H. Fredriksson, J. Cardenas, B. Kasemo and D. Chakarov
Submitted to Nanotechnology

Paper V. Oxidation of lithographically prepared amorphous carbon soot models monitored by optical spectroscopy
H. Fredriksson, T. Pakizeh, D. Chakarov and B. Kasemo
Manuscript in preparation

Peer reviewed paper, produced during the thesis period, that is not included in this thesis:

Enhanced nanoplasmonic optical sensors with reduced substrate effect
A. Dmitriev, C. Hägglund, S. Chen, H. Fredriksson, T. Pakizeh, M. Käll and D. S. Sutherland
Nano Letters, 2008. **8** (11): p. 3893

My contribution to the papers included in the thesis:

Paper I. Contributed with the idea and developed the fabrication technique after discussions with Bengt Kasemo. Performed most of the experimental fabrication work. Principal author of the paper.

Paper II. Contributed with all the experimental work and data analysis. Principal author of the paper.

Paper III. Contributed with all the experimental work and the major part of the data analysis. Principal author of the paper.

Paper IV. Contributed with all fabrication work, part of the optical measurements and the major part of the data analysis. Principal author of the paper.

Paper V. Contributed with all the experimental work and the major part of the data analysis. Principal author of the paper.

Table of Contents

1 Introduction

1.1 *Nanoscience*

Since the dawn of time, by curiosity as well as for practical reasons, man has been driven to explore and to look closer at nature. Especially the extremes have always fascinated; the extremely large, distant, strong or small. An impressive amount of creativity and thought have been invested into developing instruments and aids to facilitate investigations beyond the capabilities of our senses.

For the study of objects that are too small to apprehend, so small that the human eye cannot resolve their position and shape, a multitude of tools have been constructed. From simple magnifying glasses, via optical microscopes, to today's electron- and scanning probe microscopes, with which single atoms can be observed. The access to such characterization tools has opened up for a research field dedicated to study nature on an extremely small scale.

The study of objects with sizes conveniently expressed in nanometers (10^{-9} m or equivalently one millionth of a millimeter) is termed nanoscience. This size regime concerns objects with sizes from 1 - 1000 nm (often the upper limit is given as 100 nm). Objects with these characteristic sizes have always been present in our environment. For example, biological nanoscale objects such as viruses and proteins as well as inorganic aerosols have sizes in this regime and already in the mid 19th century colloidal solutions containing nanospheres were prepared intentionally for scientific purposes [1].

For esthetical and practical reasons as well as for amusement, miniaturization has also been a long-standing fascination for mankind. From a practical point of view it is obvious that scaling down size of useful gadgets can be very convenient. An example from the past is manufacturing of portable wrist- or pocket- watches, which are clearly more convenient to bring along than a standard wall clock. A later and even more elucidating example is the miniaturization of components used in computers, which in the beginning were large enough to fill entire rooms (fig.1.1).

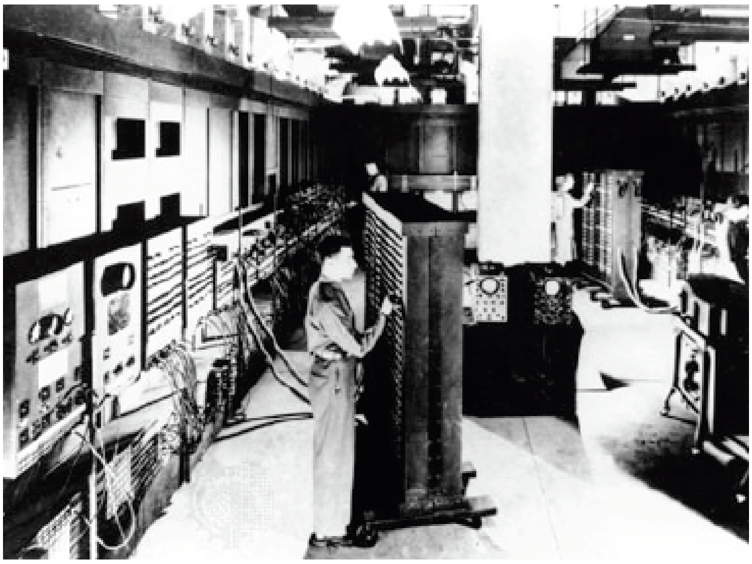

Figure 1.1 One of the first computers, ENIAC, weighing 30 tons and occupying a 15x9 m large room, was built in the 1940s, before nanofabrication techniques were available.

Investigations of nanosized objects have been going on in parallel with the efforts to design and manipulate matter on a similar scale. For the purpose of fabrication, techniques developed to study nanoscale objects have been adjusted to also facilitate manufacturing. With both characterization and fabrication tools capable of handling the nanometer size regime, it is now possible to systematically manufacture devices with desired nanoscale dimensions, examine the result of the fabrication process and to carefully characterize the nanodevice properties. In this manner, the influence of nanostructure size on the mechanical, electrical, optical, magnetic and chemical properties (to name a few) for a multitude of materials have been investigated[2, 3]. Such investigations provide valuable information about fundamental physics and contribute to the general understanding of nature, as well as laying the foundation for a variety of new technological products.

1.2 Applied nanoscience

Nanoscience and fabrication is applied in a variety of contexts. Careful investigations of functionality of catalysts, which are of enormous practical importance, can be undertaken with a combination of nanofabrication and characterization[4] techniques. Also in the challenge of meeting future demands on sustainable energy, nanoscience is predicted to play an important role, e.g. in the design of efficient and affordable solar cells and in photochemical devices for splitting water to create hydrogen (fig.1.2)[5]. Another research field of current interest, where nanoscience is of crucial importance, is climate modeling and monitoring. The international panel on climate change (IPCC) has identified aerosols (naturally occurring, airborne micro and nanostructures) as important contributors to the thermal balance of earth’s atmosphere[6].

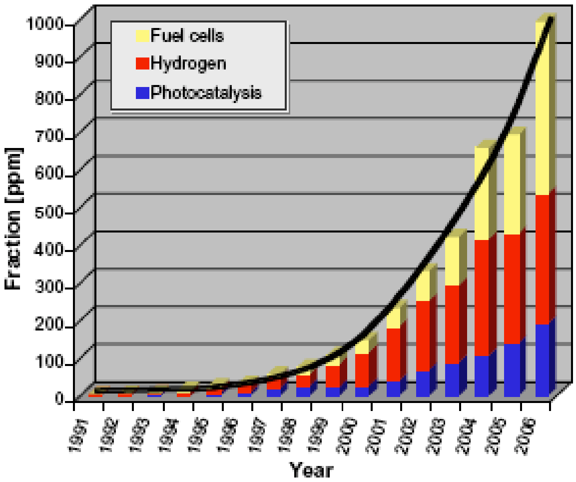

Figure 1.2 The number of publications using nanoscience in three different research fields, taken from [5].

Not only have nanostructures been fabricated and studied for the purpose of investigating their physical properties, but fabrication and investigation of nanosized objects are also of great interest in commercial applications. One of the most highly developed commercial uses of nanotechnology is found in the electronics industry. Fabrication of both semiconductor components and magnetic storage devices relies on - and helps developing - nanofabrication techniques. Therefore, computers and mobile electronics are examples of applications where nanofabrication is the key requirement for the enormous development that has occurred since the end of the 20th century. Other commercial fields where nanotechnology is applied are medicine, composite material engineering, security and crime investigations (fig.1.3) [7-11].

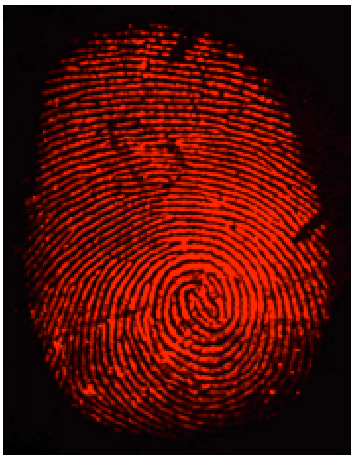

Figure 1.3 Thumbs up for nanoscience. A fingerprint detected using anti-body functionalized nanoparticles, taken from [10].

1.3 Carbon nanostructures

It is not only the size, but also the material in a nanostructure, that determines its physical properties. Therefore, different materials are more or less well suited for specific applications. In this thesis, the material of choice has been carbon, which is well motivated for a number of reasons. The importance of carbon is indisputable, not only due to its abundance (by number density the fourth most abundant element in the universe[12]), but also for its appearance in technical applications as well as for forming the backbone of organic matter. In nature, carbon appears in pure forms as graphite, diamond and in the amorphous phase, all of which are important in technical applications such as metal alloys and diamond for tools, composite materials, plastics, lubricants, protective coatings and high temperature applications. It also appears in atmospheric gases and pollutants (e.g. CO_2 and soot) in fuels (hydrocarbons and coal) and in space (interstellar dust). Furthermore, it is suggested that carbon will play an important role in future electronics applications and synthetic materials[3, 9]. Therefore, the vast research efforts that have been and still are undertaken, in order to characterize the properties of carbon-based matter, are well motivated.

In addition to the naturally occurring carbon materials (graphite and diamond) discussed above, carbon also forms two nanostructure allotropes. One is the Buckminster fullerene[13] and the other is carbon nanotubes[14]. Since the early 1990s the single most studied nanostructure is the carbon nanotube (CNT) and much effort has been invested into characterizing this fascinating material as well as into developing applications. Because of their exceptional mechanical strength in combination with semi-conducting or metallic as well as optical properties, CNT's have been used to fabricate nanoelectronic components (like transistors)[3, 15], composite materials with high strength and electrical conductivity[9] and efficient light absorbers[16].

Multitudes of other carbon nanostructures prevail and are being investigated with similar and other applications as for the CNT's in mind. However, in addition to the usefulness of carbon nanostructures in different applications, their unintended presence can cause big problems. In many processes, especially combustion of carbon-based fuels in power plants, diesel engines and open fires, soot is generated. Soot consists predominantly of carbon, forming particles with sizes in the nanometer regime. Because of their abundance and impact on the environment and health it is important to know and understand their physical and optical properties. Smog pollutes and decreases visibility in our everyday environment. Soot in the atmosphere can also contribute to global warming via the strong absorption of light (which eventually is turned into heat)[17-21]. However, the contribution from carbon-based aerosols to the atmospheres energy balance is still under debate and there is currently no consensus on their net effect on global warming[6]. Another aspect on airborne carbon nanostructures is their toxicological properties. Investigations of these (as well as for other nanpoparticles) have shown that negative health effects can be expected[7, 8]. It is also believed that carbon nanostructures are responsible for the optical absorption at ~220 nm observed in astrophysical studies[22, 23].

1.4 Scope and motivation of the thesis:

The work presented in this thesis is divided into two major parts; development of a nanofabrication technique and application of this technique, in particular for fabrication and investigations of carbon nanostructures.

1.4.1 Development of a nanofabrication technique

The first part treats nanofabrication in general and the further development of a very useful self-assembly based technique, colloidal lithography (CL), into a new and more versatile version named hole-mask colloidal lithography (HCL). CL is a relatively simple and flexible nanofabrication technique, with modest demands for advanced laboratory equipment, but with excellent control over fundamental nanostructure properties. Since it uses self-assembling colloidal spheres to define nanostructure size, shape and spatial distribution it is also well suited for upscaling to patterning of surface areas of several tens of cm^2. It is therefore well suited both for fabrication of samples for various applied and fundamental research projects and for commercially useful nanostructures. All these advantages are shared between the conventional CL technique and the further developed version HCL.

The objective of developing the HCL technique was to further expand the applicability and versatility of CL. One of the numerous benefits with the HCL technique is the plethora of nanostructure geometries that can be achieved, using the same basic fabrication approach. Furthermore, it should be noted that the fabrication technique is essentially independent of the used substrate- and nanostructure- materials, which makes it robust and easy to adapt to different requirements. Another advantage, which was also a direct goal with developing the HCL technique, is that no reactive oxygen treatment of the nanostructured samples is needed, which is often the case for the previous colloidal lithography approaches. This is very useful for the fabrication of nanostructures of oxygen sensitive materials such as carbon and ruthenium.

1.4.2 *Fabrication of carbon nanostructures*

The second part of the thesis concerns applications of the developed nanofabrication technique for fabrication and investigation of various nanostructures and their fundamental properties. The first objective here was to demonstrate the versatility of the HCL-technique by fabrication of gold and silver nanostructures with different geometries and their applications for investigations of optical properties. Both gold and silver nanostructures are known to exhibit extraordinary properties both for absorption and scattering of visible light and as substrate in investigations of adsorbed molecules in surface enhanced Raman spectroscopy (SERS). The optical properties of nanostructures are very sensitive to their shape and size. Therefore, a set goal that has also been achieved was to demonstrate that HCL facilitates control over these relevant properties. A number of following publications also prove the usefulness of the developed nanofabrication scheme for fabrication of nanostructures in other materials and for other applications[24-30]. However, the bulk part of the present thesis concerns fabrication and investigation of carbon nanostructures.

1.4.3 *Investigation of carbon nanostructure properties*

In this thesis, applications of HCL for fabrication of nanostructures in different types of carbon materials are demonstrated. Only carbon of graphitic character was used, including amorphous graphitic carbon, glassy carbon and synthetic graphite. The other three carbon allotropes, diamond, fullerenes and carbon nanotubes were not considered. It is demonstrated that HCL can be used to fabricate anything from crystalline graphite to amorphous carbon nanostructures with good control over distribution and size. Samples with carbon nanostructures covering several cm^2 and with sizes ranging from a few tens up to several hundreds of nanometers have been fabricated for applications in different experiments. These experiments investigate and compare the physical properties of nanostructures in the different types of carbon materials, and correlate these with structure size and shape.

Two main properties of the fabricated carbon nanostructures have been investigated; their optical properties and their reaction with oxygen. The optical properties were studied in detail, to achieve fundamental knowledge and for the use in specific applications. Especially the dependence of optical properties on nanostructure size, shape and carbon quality has been investigated. Optical techniques were also used to investigate the mechanical and thermal properties of the fabricated nanostructures.

Oxidation of carbon nanostructures is the other central property that was thoroughly studied. The response of different nanostructured carbon materials, both to molecular oxygen and to oxygen plasma, was studied. These studies provide information on the tendency of oxidation for different carbon materials under different conditions. Conclusions from these experiments provide information that is useful in many practical situations, e.g. durability of carbon containing materials, combustion of coal, exhaust cleaning and climate modeling. As a specific example, combinations of the results from the different studies have been used to study combustion of lithographically prepared, nanosized carbon structures, by means of their optical properties.

2 Nanofabrication

A multitude of different nanofabrication approaches have been developed throughout the years based on different fundamental ideas. This chapter will only provide a brief discussion of the different aspects of the major techniques, but several excellent reviews and books are available for the interested reader[31-34]. The nanofabrication methods presented here can be divided into three major classes; pattern writing, pattern replicating and self-assembly techniques. Each of these has individual advantages and limitations.

2.1 Pattern writing techniques

- Electron beam lithography (EBL)
- Focused ion beam patterning (FIB)
- Scanning probe microscopy based lithographies (SPML)

These techniques are characterized by flexibility of the structure shapes and patterns that can be produced[33-36]. Virtually any two-dimensional pattern within the resolution limits can be "written" onto the surface. Resolution limits for EBL and FIB are on the order of ~10 nm whereas SPML techniques can position individual atoms and thus can be said to have a resolution below 1 nm. The processes are serial, i.e. one feature is written at a time, and the techniques are thus relatively slow and therefore not compatible with large area patterning, although various schemes for parallel writing are being developed to increase the speed of these techniques. However, for research applications that do not require samples with large surface areas and where the necessary (but often expensive) machinery is available, these techniques are well suited.

2.2 Pattern replicating techniques

- Photo lithography (PL)
- Nano imprint lithography (NIL)
- Ion projection lithography (IPL)

These techniques are used to reproduce predefined patterns from templates or masks. The methods are characterized by high throughput of structured surface area[34, 35, 37]. Therefore, these techniques are ideal for large scale, serial production. Limitations on resolution and throughput are steadily pushed forward (resolution is currently well below 100 nm), especially by the semi-conductor industry. On the other hand, the flexibility of these methods is relatively low and new masks and templates need to be fabricated for every new pattern configuration. For research applications where nanostructure size, separation and shape are important variables these methods are not very well suited. In addition, it is required that researchers have access to pattern defining equipments, such as EBL.

2.3 Self-assembly techniques

- Polymer self assembly
- Colloidal Lithography (CL)

Patterns and structures are here determined by inherent properties of the lithography mask constituents. By altering the process parameters, some control over the produced patterns can be attained. Therefore these methods are normally more flexible than the pattern replicating techniques but less flexible than the pattern writing methods[38-40]. Simplicity of the required equipment and large area compatibility are also trade-marks of the self-assembly based methods. Therefore, these methods are very useful for studies where sample surface areas from ~1 cm^2 are required, and where structural parameters of the nanostructures are being investigated. These techniques are also useful for large-scale fabrication processes, where exact distribution and/or shape of the nanostructures are not of central importance.

CL is the category to which the fabrication method presented in this thesis belongs and the subject will be treated in the following chapter[38, 40, 41]. Lithography using nanosize spheres to pattern surfaces can be seen as an intermediate between the pattern writing nanofabrication methods such as EBL, FIB and SPML and the pattern replicating methods PL and NIL. The method is based on self-assembly of nanospheres on surfaces and either the gaps between close packed spheres or the spheres themselves are then used as an etch- or evaporation mask. By choosing the colloidal particle size, separation and processing conditions, it is possible to control the size, separation, distribution and even shape of the resulting structures with an astonishing flexibility.

Colloidal lithography can routinely produce structures with sizes down to a couple of tens of nanometers and has proven able to fabricate structures not easily achievable with EBL like sharp edge particles and hollow cylinders[38, 42]. Furthermore, it is a relatively simple method with little demands for advanced machinery and it is a parallel method, well suited for patterning large surface areas, which distinguishes it from the previously described lithographic methods (EBL, FIB, and STML). Contrary to the pattern replicating methods (PL, NIL), CL requires no other lithographic technique to pre-define structure characteristics but possesses intrinsic control over the pattern parameters.

2.4 Challenges and limiting factors

There are several challenges to be met in the further development of nanofabrication methods. From a commercial point of view increasing fabrication speed and decreasing structure size and number density at competitive costs, are the most central ones.

Since methods like STML can already reach the ultimate size limit for “atomic materials”, the challenge there is rather to simplify the techniques and to make them routinely available to a broader group of users. If commercial applications shall be reached, they also need to be made both faster and cheaper.

FIB and EBL are already highly mature techniques capable of defining structures with sizes down to 5 nm. However, the serial nature of these methods will probably restrict their broader applications, for quite some time, to the fabrication of masks to be used in pattern replicating techniques.

Developments in PL with the present techniques used commercially are estimated to be able to reach down to ~45 nm in inter-particle distances. Furthermore, other versions of photolithography utilizing extremely short wavelength synchrotron radiation and interference gratings instead of conventional photolithography masks have already been demonstrated and are predicted to reach even better resolution[37].

Imprinting techniques are ultimately limited by the graininess of matter but can theoretically fabricate structures down to the single nm regime. In practice however differences in thermal expansion properties of the involved materials, difficulties to align different stamps used in subsequent process steps and extreme demands on surface flatness over large areas, limit its applicability on a larger scale.

From a scientific point of view, requirements on nanofabrication methods are often quite different, compared to those imposed by the semiconductor industry or other present or future large scale applications. Flexibility of the method, i.e. adjustability to different user needs, is often an important property since the influence of different nanostructure properties such as shape, size, distribution and material on physical properties is of obvious scientific interest. Examples are quantum effects in small particles, optical scattering by sub wavelength structures or biological functionality of nanostructures. In these contexts the pattern replicating techniques are not very suitable since often only small series of samples with identical properties need to be fabricated. The more flexible techniques like EBL or STML meet the requirement that structure properties can easily be changed but are on the other hand expensive and complex methods. For patterning of surface areas of several cm^2 they are also slow.

Self-assembly methods, such as CL, are well fitted to meet the demands for a flexible, affordable and large surface area compatible nanofabrication technique. Important current limitations of the self-assembly based methods are that they do not offer precise spatial positioning of structures, which hinders synchronization of sequential process steps, and some lack of versatility regarding shapes of the structures that can be fabricated.

Since each nanofabrication technique is associated with different advantages and limitations it is often convenient to combine two or more techniques to achieve the desired nanostructure patterns. For example, PL can be used to define structures on larger length scales, such as electrodes, while CL is used to define nanopatterns in the regions between the electrodes. CL can also conveniently be used to make guiding studies to find relevant sample parameters, like nanostructure size, shape and inter-particle spacing. Once the parameter intervals, where the nanostructures exhibit the most interesting properties for a certain application, are identified, more costly and time-consuming techniques, like EBL, can be used to fine-tune the nanostructure geometries and distributions within the relevant regimes.

3 Hole-mask colloidal lithography (HCL)

The nanofabrication technique described in this thesis, hole-mask colloidal lithography (HCL), is a variation of colloidal lithography and relies on techniques that are already frequently used in other nanofabrication methods:

- Spin coating of polymer films
- Self-assembly of colloidal spheres (nanospheres)
- Thin film deposition
- Reactive Ion Etching (RIE)

In this chapter the focus is entirely on the HCL technique, which is described and discussed in detail.

3.1 Colloidal lithography

Colloidal lithography (CL) is currently used in many different versions, each with its own specific advantages and limitations[38, 40]. A frequently used version, developed by van Duyne et.al., has been named nanosphere lithography (NSL). It uses nanospheres in hexagonally close packed monolayers as etch or evaporation masks[43]. Since the nanospheres are arranged on the surface in a close packed crystal pattern, structures fabricated with this method are also arranged in long range ordered patterns, i.e. forming a lattice. Spherical particles, even when packed as closely as possible leave gaps in between adjacent entities. For the case of close packed spheres, these gaps have triangular shapes, with each side constituted by a circle segment. In its simplest form, NSL uses the nanosphere monolayer crystal as an evaporation mask, thus forming triangular nanostructures replicating the gaps in between the spheres. Several simple variations of the fabrication process, such as tilting and rotating the sample, have been demonstrated to significantly alter the shape, separation and arrangement of the nanostructures that can be fabricated using this method[44].

3.2 Sparse colloidal lithography

In an alternative method, which will be referred to here as sparse colloidal lithography (SCL), nanospheres are dispersed on surfaces from colloidal solutions, not in a close packed pattern but in a sparse monolayer, i.e. with separation between the individual spheres. This method, previously described in detail in several publications, has up to now mainly been used to define etch masks for ion milling processing[41, 45]. Below, the SCL method in its simplest form, producing supported nanodiscs with well-defined diameter, thickness and average separation, will be reviewed.

First a thin film of the material of choice for the nanostructures is deposited onto a flat surface. Already here, the nanostructure thickness is determined. The thin film is then covered with an adhesive layer of molecular thickness, consisting of a polyelectrolyte film, onto which a sparse layer of nanospheres is adsorbed. The polyelectrolyte film is used to provide the surface with a charge state opposite to that of the colloidal particles, which in turn facilitates their adsorption on the substrate. Ion milling, using high-energy ions, is then used to transfer the nanosphere pattern into the thin film initially deposited on the surface. The nanospheres act as a protective etch mask, so that only the material between them is etched away. Residues of the spheres are finally removed using a reactive oxygen treatment (UV-ozone, or oxygen RIE). By changing the order in which the process steps are performed and by varying the process conditions during film deposition and/or ion milling, e.g. the etch- or evaporation angle, this method can easily be used to fabricate alternative structures such as nanorings, crescent or extended films with nanoholes[42, 46, 47]. The development of hole-mask colloidal lithography (HCL) described below, is based on the SCL technique and can be seen as an extension of SCL to increase its versatility and applicability.

3.3 Hole-mask colloidal lithography

The HCL technique, described in Paper I, uses a sacrificial layer to separate the nanosphere mask from the surface to be patterned, which gives rise to many advantages and possibilities. The lithography can be thought of as composed of three major process steps, i) fabrication of a supported, patterned mask, ii) transfer of the mask pattern through etching and iii) transfer of the mask pattern through material deposition.

3.3.1 Fabrication of a supported, patterned mask

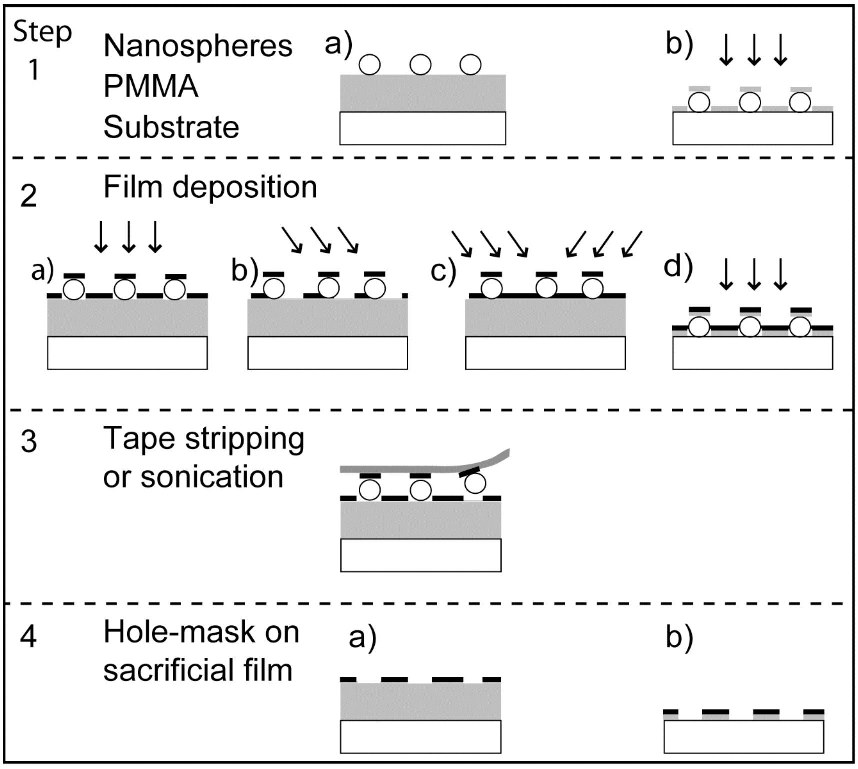

Figure 3.1 Schematic description of mask fabrication: 1) PS nanospheres supported on a) a polymer film or b) directly on the substrate surface are used as an evaporation mask. In b) the sacrificial layer is deposited subsequent to the polystyrene spheres. 2) Depending on deposition angle the resulting holes in the deposited mask are a & d) round and replicate the sphere diameter, b) elliptical with the long axis larger than the sphere diameter or, c) round or elliptical with diameter smaller than the nanospheres. 3) The nanospheres are removed using tape stripping or ultrasonic cleaning. 4) The final result is a hole-mask supported on a sacrificial layer.

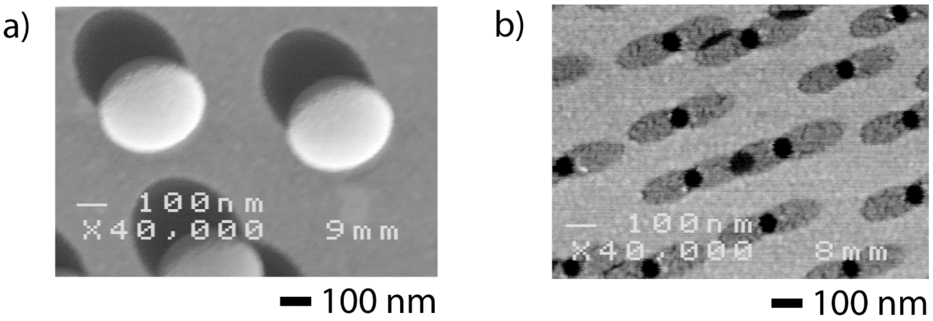

Figure 3.2 SEM images of a) Au-mask supported on a polymer film, deposited from an angle 45° from the surface normal, before tape stripping away the 190 nm diameter nanospheres. The holes in the mask, appearing black in the image, are partly covered by the remaining (white) spheres. The shape of the holes is clearly elliptical. b) Au-mask resulting from sequential deposition from two opposite angles 60° from the surface normal, after tape stripping. The holes (black) are slightly elliptical and with roughly half of the diameter of the used 110 nm nanospheres. The elliptical grey areas represent regions where the mask is thinner than in the bright grey areas, due to shadowing of the evaporation from one of the angles. Occasionally shadows deriving from evaporation from opposite angles overlap, which shows up as darker grey areas (e.g. near the centre of the image).

Fig.3.1, Step 1: a) The initial process step, is deposition of a sacrificial layer, conveniently achieved by spincoating a thin polymer film onto the surface, a process already well established and used for PL and EBL processing. The polymer film is briefly treated in an oxygen plasma (5 s., 50 W, 250 mTorr), which decreases the hydrophobicity of the polymer surface. This is important in order to avoid spontaneous de-wetting of the surface during subsequent deposition of polyelectrolyte and nanospheres, which in turn is important to get a high quality, homogeneous surface distribution of the spheres. A water solution containing a positively charged polyelectrolyte is pipetted or poured onto the polymer film. The next process step is deposition of negatively charged nanospheres onto the adhesive, electrolyte-covered polymer surface and subsequent drying under an intense N_2-gas jet. To increase the stability of the adsorbed pattern of nanospheres, the samples can be dipped in a hot fluid, which promotes adhesion between the colloids and the polyelectrolyte and polymer film[48].

b) Alternatively, the nanospheres can be deposited directly onto the substrate surface, in which case a thicker (triple) polyelectrolyte layer should be used[48]. The sacrificial layer is then evaporated onto the surface, prior to the mask layer deposition. A convenient choice of sacrificial layer for many applications is Cr, but other materials can of course also be useful. The main concern is that it should be possible to selectively disolve the sacrificial layer, leaving the substrate and the fabricated nanostructures unchanged.

Fig.3.1, Step 2: In the following step a thin film, resistant to oxygen plasma, is deposited onto the surface. This layer is referred to as the hole-mask and depending on deposition angle, it is possible to control the shape and size of the holes in the mask as demonstrated in fig.3.2. A requirement on the deposited film is that it is thinner than about half the nanosphere diameter and thick enough to be continuous.

Fig.3.1, Step 3-4: Subsequently, the nanospheres can be removed by simply attaching a piece of tape to the surface. As the tape is removed the spheres, sticking harder to the tape than to the polymer surface, are removed as well. Alternatively the nanospheres can be removed by cleaning the sample in an ultrasonic bath and iso-propanol. At this stage the polymer supported thin film has holes in it where the spheres were covering the surface during the deposition process. The number density and diameter of these holes correspond to the shadows of the nanospheres on the polymer film. By the salt concentration and size of the nanospheres in the deposited colloidal solution, the number density and diameter of the holes in the mask can easily be tuned[48]. Changing the angle from which the thin film is deposited can also alter the shape and size of the holes (fig.3.2). Deposition from any angle other than the surface normal results in stretched out shadows and thus elliptical holes in the mask. On the other hand, if two or more opposite angles are applied, material is deposited in under the nanospheres, resulting in holes in the mask, which are smaller than the sphere diameters.

3.3.2 Transfer of the mask pattern through reactive ion etching

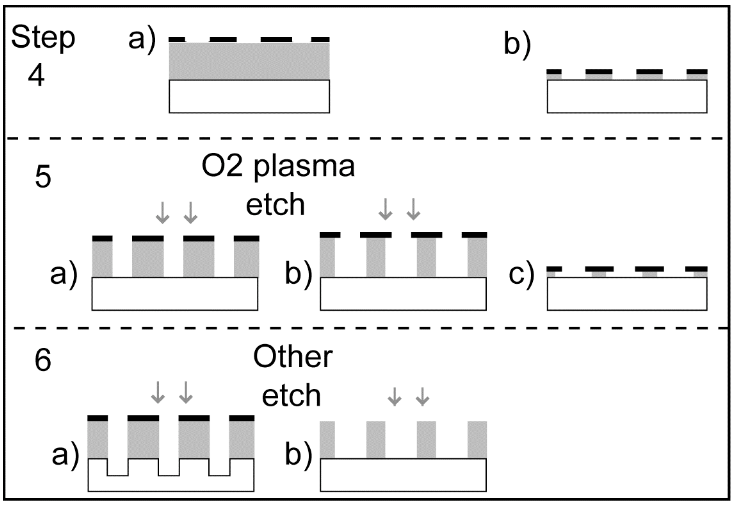

Figure 3.3 Pattern transfer into the sacrificial polymer layer using oxygen plasma. The duration of the pattern-transferring plasma-etch determines the degree of undercut. 5) A short oxygen plasma treatment gives a) little or no undercut and b) extended etching gives a controlled undercut. c) For the example with a Cr sacrificial layer a wet-etch in Cr-etch is required to achieve undercut and a good liftoff later on. 6) A second etch process can be applied to further a) transfer the pattern into the substrate or b) to remove the hole-mask prior to further processing.

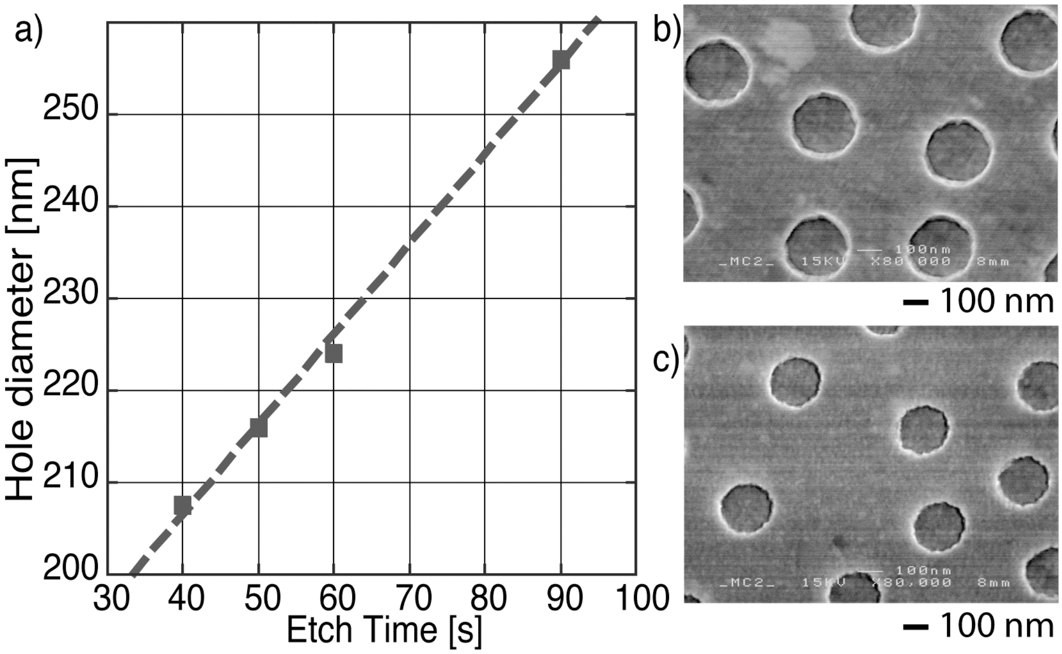

Figure 3.4 a) Size of the holes in an undercut polymer film as a function of applied oxygen etch time starting with 190 nm holes in the mask. The SEM images display 80 nm thick polymer films after oxygen RIE (50 W, 250 mTorr) and subsequent removal of the hole-mask, corresponding to the longest b) (90 s) and the shortest c) (40 s) etch times presented in the graph.

Fig.3.3, Step 5: The subsequent process steps aim at transferring the thin film hole-pattern into the sacrificial layer. When a polymer film is used, this is easily achieved using oxygen RIE. The plasma conditions can be chosen so that all of the polymer exposed under the mask holes is removed while the polymer covered by the film is unaffected. Due to the directionality of the RIE process the polymer film is etched predominantly in the forward direction. Once the polymer is completely etched through vertically, the etching will continue in the lateral direction thus creating an undercut into the polymer film. The degree of undercut varies linearly with applied etch time and can be controlled to within a few nanometers. For the Cr-film sacrificial layer, on the other hand, the hole pattern already extends all the way down to the substrate. However, a slight undercut is always beneficial for subsequent material deposition and liftoff processing. A suitable undercut can be achieved by wet-etching in a Cr-etchant (e.g. 10 s. in Nickel-Chrome etch, 711.21 Sunchem electrograde products).

Fig.3.3, Step 6: If the hole-mask is selectively removed prior to further processing, the polymer film alone will constitute the lithographic mask and the undercut can be used to continuously increase the structure diameter. This is demonstrated in fig.3.4 where a 80 nm thick polymer film covered with a gold hole-mask has been etched in an oxygen plasma at 50 W, 250 mTorr for different times. After pattern transfer into the sacrificial layer, the hole-mask pattern can be transferred further into the surface by choosing the proper etching conditions for the surface at hand. An example, which has been demonstrated in Paper I, is that of etching into a TiO_2 surface using CF_4 RIE. Care has to be taken so that the thin film mask material is resistant to both of the etching processes applied to penetrate the sacrificial layer and to extend the etching into the substrate.

3.3.3 Transfer of the mask pattern through deposition

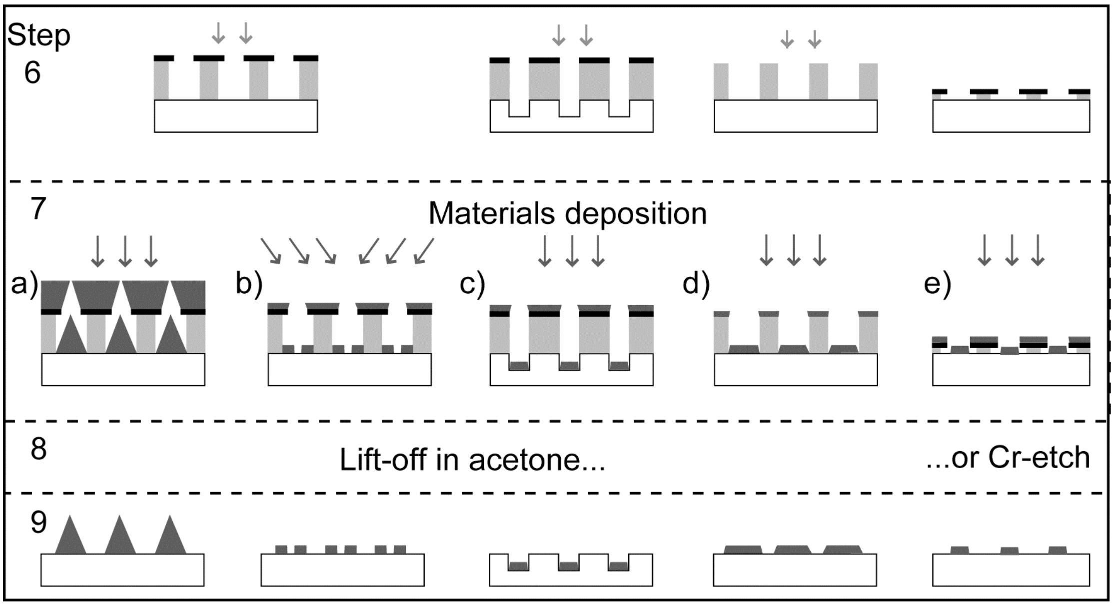

Figure 3.5 Applying different deposition parameters, many different structure shapes and distributions can be obtained. 7) a) Deposition of a thick layer of nanostructure material results in cone shaped features. b) Using two different polar angles to deposit materials yields particle pairs. c) Deposition of materials through a mask where the pattern has already been transferred into the substrate surface (by etching) results in nanodiscs buried into the etch pits. d) Evaporation through a mask where the top layer hole-mask has been selectively removed (without significantly affecting the polymer mask) gives structures with a diameter replicating the undercut in the polymer film. e) Deposition through the Cr-supported hole-mask gives particles with similar diameters as the hole-mask. 8) Liftoff is achieved by immersing the sample in a solution, suitable for the particular sacrificial layer.

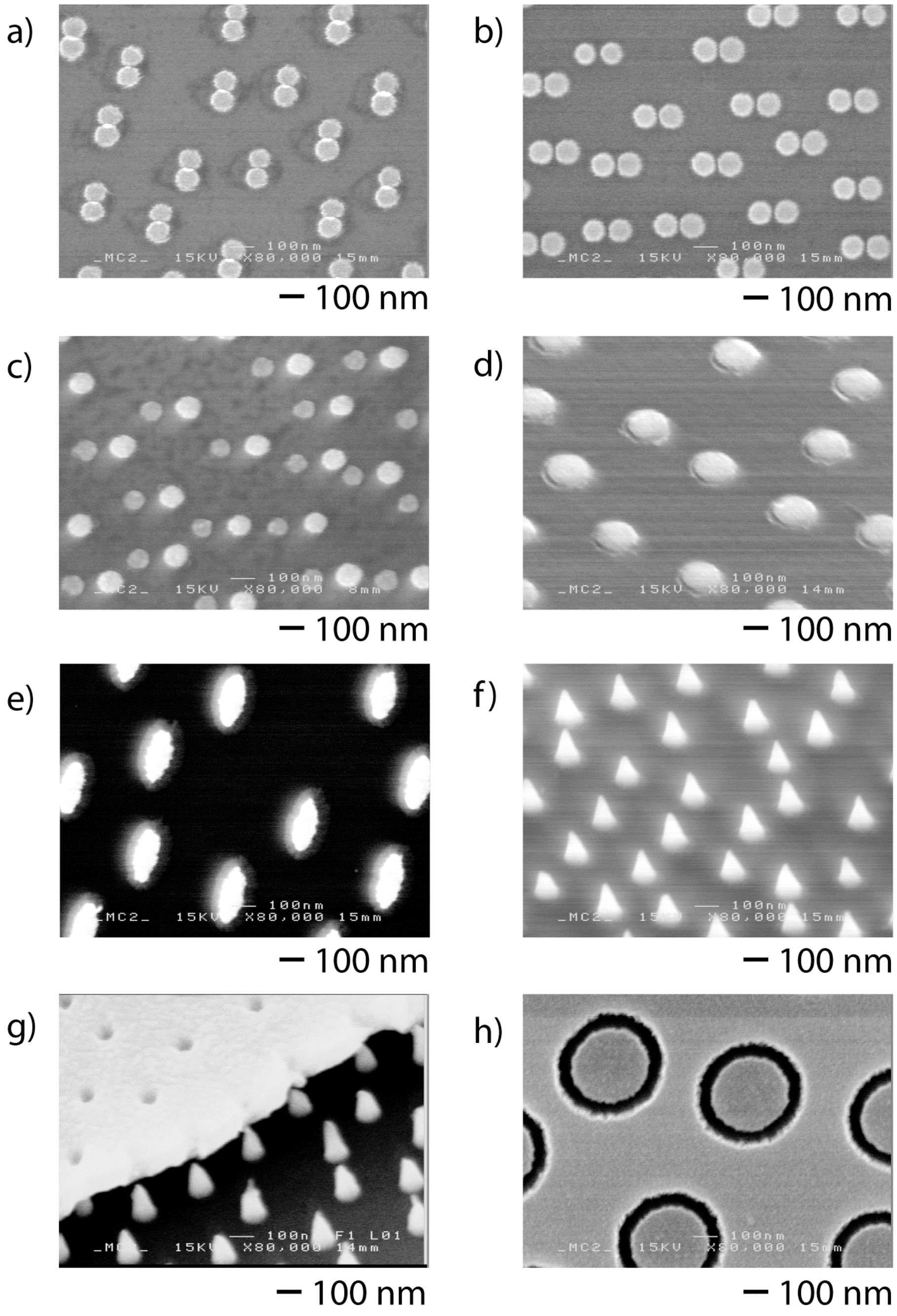

Figure 3.6 SEM images illustrating some of the different structures fabricated with HCL. a) and b) show particle pairs with different separations; just overlapping and separated by ~10 nm respectively. These structures were fabricated using identical deposition conditions and hole-masks while different polymer film thicknesses were used to alter the particle separation. c) Particle pairs made up of two different materials (Au and Ag). d) Nanodiscs in holes etched into the surface. e) Elliptical, layered structures of Au on top of SiO_2. f) Nanocone array. g) Nanocones and mask after partial liftoff. h) Inverted ring structure, Cr on Si.

Fig.3.5, Step 7: The process steps described so far have resulted in a thin film hole-mask, supported on a sacrificial layer with a similar pattern. This double layer mask can then be conveniently used as an evaporation mask to yield a variety of nanofeatures as demonstrated in fig.3.5 & fig.3.6. Collimated deposition of materials from a source positioned along the surface normal results in structures on the surface with a shape replicating the holes in the thin film mask (fig.3.5e). If the hole-pattern has already been transferred into the surface, the structures will end up at the bottom of these holes (fig.3.5c & fig.3.6d). In this way nanostructures can be incorporated into a surface film rather than just placed on top of it.

Deposition of materials from a source positioned anywhere off the surface normal results in structures laterally displaced with respect to the centre of the mask hole. Choosing two opposite polar angles to deposit materials from thus results in a pair of structures (fig.3.5b). Both the thickness of the double layer mask and the deposition angles can be used to control the separation between the two structures in the pair. It is however preferable to alter the thickness of the mask and keep deposition angles constant to avoid shape aberrations that may be introduced by deposition from steep angles (>20° from the surface normal). Using the same strategy it is also possible to fabricate three or more structures from each hole in the mask.

If thick layers are deposited through the mask the structures growing on the surface will gradually attain a noticeably smaller diameter. This is related to the deposition of materials on top of and on the rims of the mask-holes, which tend to gradually decrease the diameter of the holes. When depositing particle pairs, this has the consequence that if the different particles corresponding to different deposition angles are fabricated sequentially, the first structures will attain a larger diameter than the second ones (fig.3.6c). This can be avoided by frequently altering between the two chosen deposition angles (fig.3.6a & b). Another consequence of the shrinking mask-holes is that extended deposition through circular holes in the mask result in cone-shaped structures on the surface (fig.3.6f & g). The rate at which the holes close is dependent on the deposited material, which means that thick structures composed of different materials, will have a different side-wall angle at different parts of the cone. This can be used to place discs of different sizes on top of each other, separated by a spacer layer[27].

If the mask material is properly chosen it can be selectively removed prior to material deposition (using for example wet etching), leaving only the polymer mask on the surface. This has the advantage that the under-etch of the polymer then can be used to fine-tune the diameter of the structures that are produced (fig.3.5d). Another example where the hole-mask rather than the sacrificial layer is removed is demonstrated with the Cr sacrificial layers. Deposition of Cr through a Au hole-mask, after a short under-etching into the Cr-layer and removal of the hole-mask using a suitable wet etchant (Au-etch), results in an inverted Cr ring structure (fig.3.6.h) (or equivalently, Cr discs in holes in a Cr-film). This fabrication strategy can of course be altered to include two, between themselves different materials, e.g. Pt discs in a Cr hole-film.

Fig3.5, Step 8: In the last process step the sacrificial layer can be removed using an appropriate solvent. Usually acetone works well for polymers and Cr-etch for Cr- sacrificial layers. It should be pointed out that the thickness of the sacrificial layer film should be chosen to be comparable to or thicker than the nanostructures intended for fabrication. With a too thin sacrificial layer, nanostructures deposited through the mask will stick up through and into the hole-mask, which may result in partial removal of the structures due to establishment of physical contact with the hole-mask.

3.3.4 Limitations and extensions

The above described method, with a polymer sacrificial layer works well for fabrication of discs, ellipses, particle pairs or cones of any material that can be deposited from a reasonably collimated source, on most surfaces flat enough to spin coat and that are not very sensitive to oxygen RIE. A great advantage of always using the same sacrificial layer material is that the deposition of nanospheres onto the surface is standardized. Therefore, the deposition process will not suffer from variations due to intrinsic properties of the surface and thus will be substrate independent. Using patterned polymer masks also has the advantage that it is a well-established technique, already used for a long time in EBL and PL, which means that deposition and liftoff procedures can simply be adopted from existing processes. In addition, polymer liftoff can be done in acetone or similar mild solvents, which is compatible with most nanostructure materials and surfaces. Another obvious advantage of the method is that, like other self-assembly based techniques, it is a parallel process and thus suitable for patterning of large surface areas.

Although polymer films are very versatile as sacrificial layers, certain situations may benefit from the use of other materials. For example, fabricating nanostructures on a surface that is oxidized and etched requires the use of a sacrificial layer that can be etched without the aid of oxygen plasma. Another situation where Cr-films are preferred over polymers is when the masks are exposed to high temperature and/or intense irradiation prior to liftoff, since such conditions can damage the polymer and prevent liftoff. As usual, the hole-mask has to be chosen to resist the sacrificial layer etchant. For Cr-films, Au hole-masks fulfils this criterion.

A limitation of the method, at present, is the lack of long-range order and the limits in particle separation that can be achieved. Long-range ordering can be achieved for example with templated deposition or printing methods, but the lack of ordering can also be an advantage. Since the structures are not ordered in crystal like patterns collective effects like optical interference tend to cancel out. The typical nanosphere coverage that can be achieved with electrostatic self-assembly has been shown to range between 12 and 52 % (projected surface area)[48]. Although the upper limit is not easily overcome without causing agglomeration of the particles, the lower limit can be pushed by some simple tricks. Starting with larger spheres and shrinking the holes in the mask by deposition from off-normal angles is one way to decrease surface coverage.

Additional to this, the nanospheres can be treated in oxygen plasma, for a short time, prior to hole-mask deposition, to further shrink the structure sizes. Mask holes with diameters smaller than the nanospheres is also possible to achieve from sputter deposition of the hole-mask[49].

The size dispersion of the fabricated nanostructures is largely determined by the size dispersion of the masking nanosperes, which is generally in the 5 % range for spheres with average diameters of 50 nm and larger. For colloidal solutions containing smaller particles (commercially available), size dispersions are considerably worse (10 % or more) and thus set a lower limit for the size of structures that can be fabricated with reasonable conformity of the achieved diameters. However, this applies to commercially available colloidal solutions, and for applications where narrower size distribution are crucial, this can be achieved e.g. by chromatographic methods.

Furthermore, it is worth mentioning that preparation of nanostructures via evaporation of materials through a supported mask depends on the collimation of the atomic beam. In deposition techniques as sputtering, chemical vapor deposition or laser ablation, which operate at higher pressure, the deposited atoms are frequently scattered by the process gases resulting in poor collimation. This results in nanostructures with ill-defined, blurry edges. In addition, due to the anisotropic deposition conditions, materials are deposit on vertical walls as well as on the horizontal surfaces. Under such conditions, a continuous film, connecting the mask and the nanostructures can be formed, which in turn can result in poor liftoff performance.

3.4 Applications of HCL to fabricate carbon nanostructures

This section describes the specific application of HCL to the fabrication of nanostructured carbon materials as demonstrated in Papers II-V. Two different strategies where adopted, one for etching out carbon nanostuctures from bulk carbon surfaces and another for fabrication of amorphous carbon nanostructures on various surfaces. The former technique utilizes HCL to prepare etch masks on carbon surfaces and subsequent oxygen RIE to define the nanostructures, whereas the latter employs a sacrificial Cr-layer and subsequent e-beam evaporation of carbon. Details and considerations related to the two fabrication processes are discussed below.

3.4.1 Carbon nanostructures from bulk materials

One of the benefits of using bulk materials and etch out the nanostructures from these is that the structures inherit the physical properties of the original material. Using this approach it is therefore possible to fabricate, e.g. crystalline graphite nanostructures. To achieve this, the specific strategy employed in this work (Paper II-IV) was to first fabricate gold nanodiscs on the carbon surface using HCL, and then to use the gold discs as etch masks in an extended oxygen RIE process to transfer the pattern onto the underlying surface. The manufacturing of gold discs on the carbon surface can be performed according to the processes described in the previous sections, with some minor differences in some of the process steps.

After spin coating, deposition of nanospheres and deposition of the hole-mask film as usual (fig.3.1, step1 & 2). the nanospheres needs to be removed. This is preferably done using a mild ultrasonic cleaning in IPA. Particularly for graphite this method is preferred over tape stripping since the bonds between adjacent planes of a graphite crystal are very weak. Tape stripping, exerting forces perpendicular to the surface, risks to break the bonds between the graphite sheets, rather than between the nanospheres and the polymer surface, thus lifting off the uppermost surface layers together with the mask instead of just the spheres.

Another step that requires extra attention is pattern transfer into the polymer film (fig.3.3, step 5) since the underlying carbon surface is also sensitive to oxygen plasma, although much less so than the polymer. Prolonged oxygen RIE after complete penetration of the polymer film might lead to damage of the carbon surface although such effects can be minimized by choosing a proper plasma etch duration. After gold deposition and liftoff, leaving gold discs on the surface, the pattern can be transferred into the carbon surface via oxygen RIE.

The response of carbon materials to oxygen plasmas is in itself an interesting and complex topic that has been thoroughly investigated in the past and will be discussed further in Chapter 4[50-54]. As demonstrated in Paper II, the response to oxygen RIE varies for different carbon materials. To exemplify, the etch rates in a 50 W, 250 mTorr plasma (generated in the system described in Chapter 6) are given for the three carbon based materials PMMA, GC and HOPG. The etch rate in the lateral direction, causing etching under a mask supported on a 80 nm PMMA film is 1.25 nm/s (derived from the graph in fig.3.4). In GC and HOPG the corresponding values are 0.15 and less than 0.015 nm/s respectively. It has to be noted that the comparison between etch rates in the polymer film and the pure carbon materials is somewhat unfair since the former value is derived from a situation where the etching has already reached the inert substrate surface and thus there is no forward etching. Under these conditions more oxygen is available for etching in the lateral direction and the value of the etch rate in the lateral direction is overestimated. The relations between the etch rates in the forward direction for the considered materials are similar to the lateral rates, although significantly higher in absolute numbers due to the more efficient supply of oxygen. For the PMMA film the forward etch rate is more than 2 nm/s whereas corresponding values for GC and HOPG are 0.65 and 0.19 nm/s respectively.

3.4.2 Evaporated carbon nanostructures

In many situations it is desirable to be able to choose different materials to support the nanostructures. Measurements of optical properties, for example, are simplified by the use of transparent substrates. For such purposes, carbon nanostructures can be fabricated using the standard HCL technique, described in the previous section, on any substrate. However, since deposition of carbon through evaporation requires very high temperatures of the carbon target material, some problems may be experienced using polymer films as liftoff layers. High temperatures, accompanied with emission of UV radiation is known to change the properties of polymers, inducing cross-linking, which in turn can influence the possibility to dissolve the sacrificial layer. Even for cases where liftoff is successful, unwanted residues can be observed on the surface (fig.3.7). An alternative explanation for the observed residues is that carbon from the evaporation process deposits on the polymer film side-walls thus creating the observed residues.

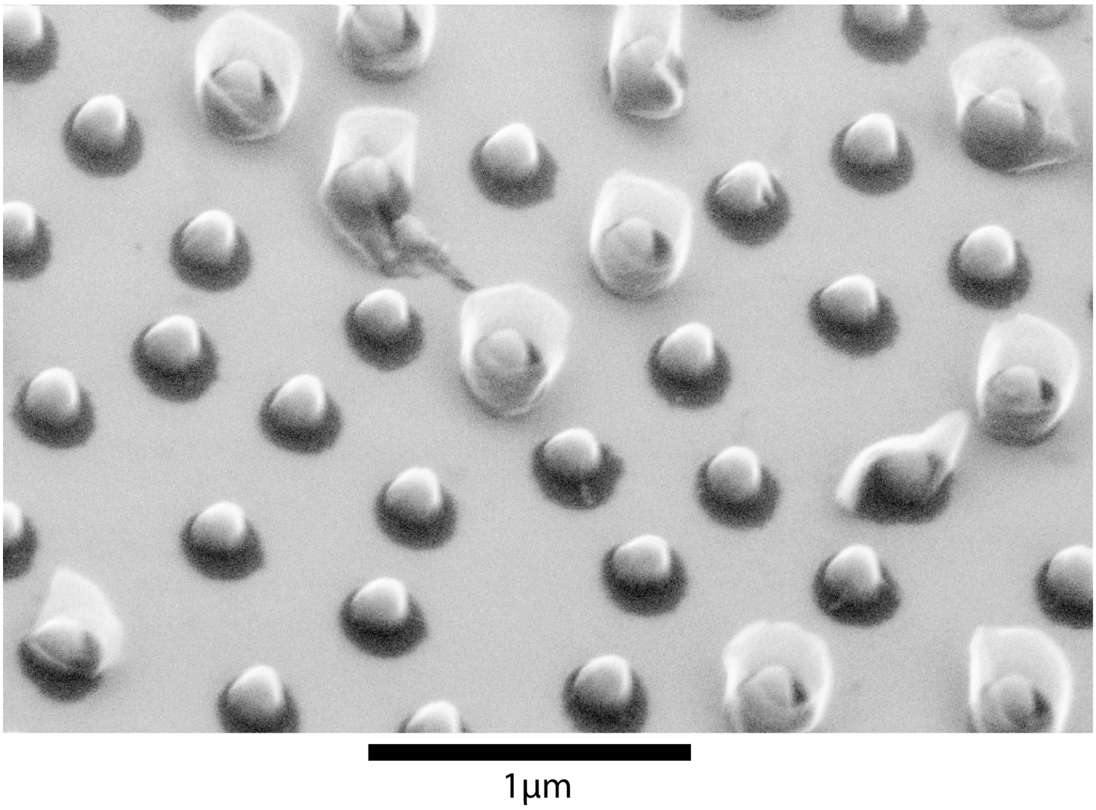

Figure 3.7 Amorphous carbon nanostructures on a fused silica substrate. The sample was prepared by evaporation of carbon through a polymer sacrificial layer. Slow liftoff is observed as well as residue material around several of the nanostructures.

Even though the effect with residue halos around the nanostructures can potentially be exploited, it is necessary to be able to avoid it. Using the Cr-sacrificial layer instead of polymers circumvents this problem. Cr has the benefit of not being as sensitive to high temperatures and UV-irradiation as polymers. As demonstrated in Paper V, this approach can be used to achieve large surface areas covered with amorphous carbon nanostructures on fused silica.

3.5 Other applications of HCL

As demonstrated in this thesis, HCL is useful for fabrication of nanostructures in several different types of applications. In addition to these, many other examples can be found in a large variety of research fields. Optical properties of cylindrical nanostructures in Pt, Pd, Ag, Au, Al have been prepared for studies of their optical properties both with near- and far- field techniques[24, 26, 28, 55, 56]. Tri-layer sandwich structures in Au-SiO_2-Au have been prepared for investigations of their optical and magnetic properties[27]. Furthermore, Au, Pd and Pt nanostructures have been fabricated for research targeting applications in optical sensing, hydrogen storage and electrochemistry[25, 29, 30, 57]. These applications further demonstrate the usefulness of the developed HCL technique and many opportunities still remain unexploited.

4 Carbon

This chapter will give an overview over the properties of solid state carbon, focusing on graphitic materials. Starting from the properties of a single carbon atom the general physical and structural properties of graphite will be described. More detailed discussions on the properties of three types of material follows; crystalline graphite, glassy carbon and amorphous carbon. In particular, optical properties, Raman scattering and oxidation in molecular and atomic oxygen for each of these carbon materials will be described and discussed in some detail.

4.1 Atomistic origin of different phases

A carbon atom has a nucleus containing six protons and consequently six electrons. In the ground state configuration these six electrons are described by the quantum numbers $1s^2 2s^2 2p^2$ where the numbers *1* and *2* denote principal quantum number, the letters *s* and *p* denote angular momentum quantum number and the superscripts denote the number of electrons with these quantum numbers. The *2s* electrons, by necessity, have opposite spins while the *2p* electrons have parallel spins. In the ground state configuration the carbon atom has only two valence electrons that can participate in binding, contrary to what is commonly seen in nature, where carbon atoms frequently form tetravalent molecules (e.g CF_4, CH_4 or diamond). However, upon bonding to other atoms, the ground state orbitals can be mixed to form hybridized states. By lifting one of the *2s* electrons to a *2p* orbital the s-orbital is hybridized with one, two or three of the p-orbitals resulting in *sp*, sp^2 and sp^3-hybridization respectively.

The *sp*-hybridization, where the *2s*-orbital hybridizes with one of the *2p*-orbitals, is found in linear or diagonal molecules like C_2H_2 (acetylene). In graphite and aromatic compounds the carbon atom orbitals hybridize into the sp^2-configuration where the *2s* orbital is hybridized with two of the *2p*-orbitals. sp^2-hybridization result in three identical electron orbitals forming a plane. The angle between the sp^2-orbitals is 120° (fig.4.1) and an unhybridized *p*-orbital, perpendicular to the plane, gives a total of four valance electrons. Strong, covalent C-C bonds can then be formed via overlap of sp^2-orbitals, as for example in the six member carbon rings of aromatic molecules. In sp^3-hybridized carbon atoms the angles between the four orbitals are such that a regular tetrahedron is formed. In this configuration, found in e.g. diamond and CF_4, the *2s*-orbital has hybridized with all three *2p*-orbitals to form four identical states, resulting in the cubic crystal structure (or, much less common, hexagonal) of diamond.

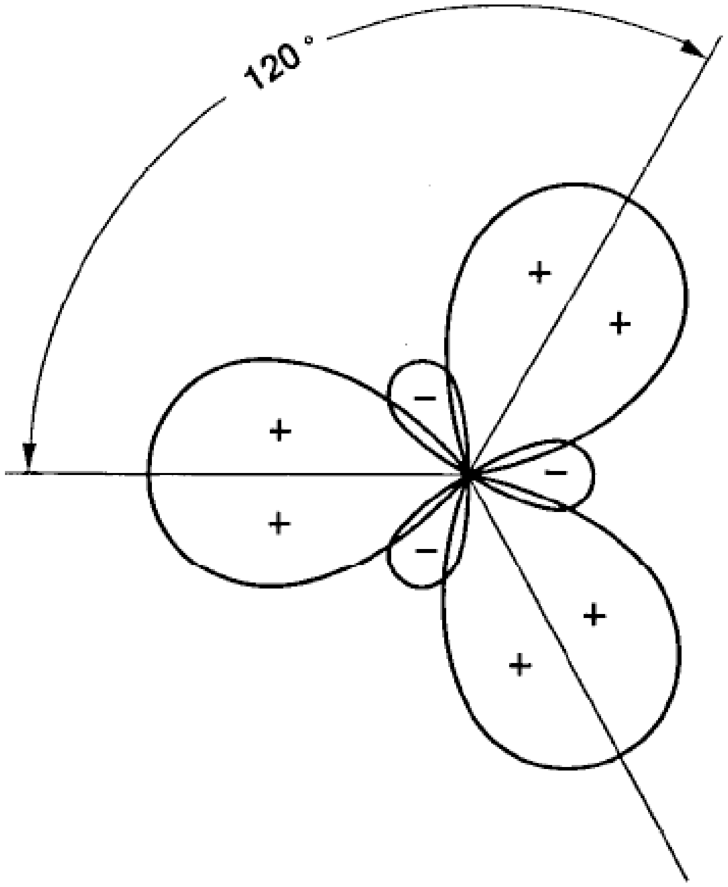

Figure 4.1 In-plane view of *sp*^{2}-hybridized orbital in a carbon atom, taken from [12]

The hybridized states are energetically less favorable than the ground state. However, both the *sp*$^{2-}$ and *sp*^{3}-hybridized orbitals are asymmetric thus facilitating the formation of strong bonds with other atoms, which compensates the hybridization energy cost. As a consequence the cohesive energy of a carbon atom in a graphite or (especially) in a diamond lattice is very high.

Only two carbon allotropes are found in nature, as minerals; diamond and graphite. In addition, there are the synthetic allotropes; carbon nanotubes and the Buckminster fullerene, which will be discussed in Chapter 5. In the form of diamond, carbon is extremely hard and dense, with high melting point, thermal conductivity and specific heat. Furthermore, diamond is an electrical insulator, chemically inert and transparent to visible light. Due to all these properties, diamond is frequently used in tools and machinery where extreme mechanical, thermal and/or optical transparency is needed. However, the focus of the rest of this chapter will be on graphite and graphitic materials.

4.2 Crystalline graphite

4.2.1 Crystal structure

Graphite is the more common, naturally occurring carbon allotrope. It consists of sp^2-hybridized carbon atoms, each atom forming a bond with three other atoms in the sp^2 bond plane. This binding results in hexagonal carbon rings linked together into atomically flat layers, referred to as graphene sheets (fig.4.2). The sheets are terminated, either by zig-zag or arm chair edges. The lattice vectors parallel to the bond-planes are termed a and b and this plane is therefore usually referred to as the ab- or basal- plane. It is also convenient to define the c-direction, perpendicular to the ab-plane. Several graphene layers, stacked upon each other and linked together by weak van der Waals forces, induced by the *2p* electrons, form a graphite crystal with a hexagonal structure. The strong bonds between atoms in the ab-plane and the weak bonds in the c-direction make it easy to cleave crystals along the ab-planes, yielding large areas of very flat surface. This simplicity, with which large, atomically flat surfaces can be obtained, is one of the main reasons for graphite's popularity as experimental model systems.

Several different types of natural graphite exist, distinguished mainly by the purity and stacking properties. The thermodynamically most favorable stacking sequence is the so-called "ABAB". The letters A and B denote single, identical graphene sheets in a graphite crystal with different orientation relative to the c-axis. The successive graphene sheets are stacked with their surfaces in parallel, but with an lateral offset such that half of the atoms in one plane (A) have a neighboring atom along the c-direction in the adjacent plane (B) while the other half are neighbors to the center of the hexagonal rings in the neighboring layer (fig.4.2). Every second plane (A) then has identical orientation, with respect to the c-axis, thus motivating the term ABAB-stacking.

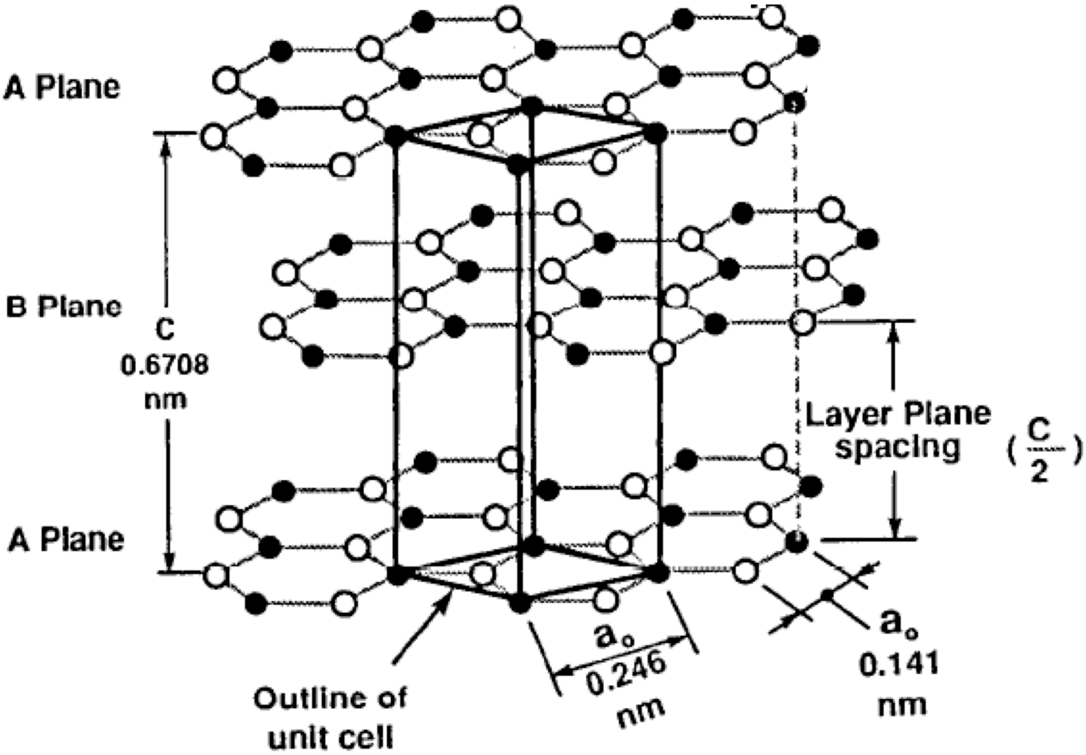

Figure 4.2 Three stacked graphene layers in the ABAB-sequence characteristic for hexagonal graphite. The nearest neighbor distance, a_0 is 0.141 nm and the distance between two adjacent layers along, c/2 is 0.335 nm. Arm-chair edges runs from left to right in the picture, perpendicular to the zig-zag edges. Picture taken from[12]

Apart from the thermodynamically most stable "ABAB" stacking, where every second graphene layer has the same orientation relative to the c-axis, there are the rhombohedral and turbostratic stacking sequences. The former is also referred to as ABC-stacking, where the nearest (B) and second nearest plane (C) is offset in opposite directions relative to the c-axis and the latter is characterized by the lack of stacking order.

Because only three of the electrons participate in strong bonds, and because these are arranged in long-range ordered planes, the crystal properties are strongly anisotropic. In the direction of the ab-planes, graphite is mechanically strong and a good electrical and thermal conductor, whereas in the direction perpendicular to the graphene layers, it is weakly held together and a poor electrical and thermal conductor. Some of the physical properties of graphite and graphitic materials will be treated in greater detail in the following chapters.

4.2.2 Band structure

Electron orbitals of individual molecules are split into energetically broad energy bands when many molecules are brought together to form a solid. The quantum mechanically allowed energies for electrons with a certain momentum (corresponding to different positions in the Brillouin zone) are described in band structure diagrams. At absolute zero temperature, electrons occupy the electronic states with the lowest energy, the ground state. The energy of the most energetic of these electrons is termed the Fermi energy, which can be taken as the zero-energy of the system. The difference in energy between two electron states (in the same or in two different bands) corresponds to the energy required to excite an electron from the lower energy state to the higher. Excitations from electron states in the same band are called intra-band transitions while transitions between different bands are termed inter-band. In the former case, the energy required for an electron excitation can be arbitrarily small while in the latter the smallest energy is determined by the energy difference between the top of the lower band and the bottom of the upper band. From the information contained in a band structure diagram, it is possible to predict electrical and optical properties of a solid material.

The band structure of graphite, shown in fig.4.3 [58], displays bonding and anti-bonding σ- and π– bands corresponding to the p and *sp*^{3} electrons respectively. For physical events involving energies below ~5 eV (such as absorption of visible light), the electron bands closest to the Fermi energy are the most interesting ones. As can be seen in the band structure diagram, these are the bonding π- and the anti-boning π*- bands. These bands approach and even intercept the Fermi energy near the K-point in the Brillouin zone. Therefore, at room temperature the π-band is almost, but not completely, filled and the π* band has a fraction of filled states. Electrons in partly filled bands, with energies close to the Fermi energy, can undergo transitions with arbitrarily small energy changes within the band (intra-band transitions). These electrons are essentially free to move around in the crystal and are the reason for the semi-metallic character of graphite. The fact that there are much fewer electrons available for intra-band transitions in graphite as compared to a metal gives it semi-metallic, rather than metallic properties.

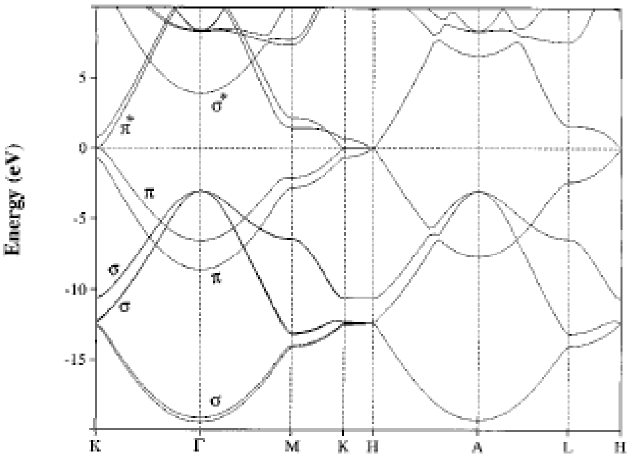

Figure 4.3 Band structure of graphite from reference [58]. The different bands are marked in the figure.

Following the π and π* bands along the Brillouine zone from the K-point towards the M-point, it can be seen that the energy of the π-band decreases, whereas the π*-band energy increases. Transitions between two different bands (like the π and π* bands) are termed inter-band transitions. Since the separation of these two bands starts from zero separation and increases continuously, inter-band transitions between the π-bands are allowed for all energies. This results in the strong optical absorption observed for graphite.

Since the σ-bands are far from the Fermi energy level and since the energy separation between the bonding and anti-bonding bands are large, only inter-band transitions are possible between these. Because of the large separation of these bands, they become important only for higher energy processes. There are some discrepancies between the literature values of the σ-band separation and values from 5 up to 12 eV can be found[58-60].

4.3 Graphitic carbon materials

There are a multitude of synthetic carbon materials available in addition to the naturally occurring minerals. Examples are high-pressure synthesized diamond, diamond like carbon (DLC), soft amorphous carbon, highly oriented pyrolytic graphite (HOPG), glassy carbon, fullerenes and carbon nanotubes (CNT's). Out of these, all but the first two are mainly graphitic. In general they are synthesized from carbon rich precursors such as carbo-hydrides or polymers and heated to high temperatures. This work concerns carbon materials dominated by *sp*^{2}-hybridized carbon, referred to as graphitic carbon. Therefore a more detailed description of the relevant materials follows below.

4.3.1 Crystalline graphite, synthetic and natural

In addition to the natural graphite crystals discussed above, several types of synthetic graphite are available. The carbon material coming closest to the ideal graphite crystal is highly oriented pyrolytic graphite (HOPG). Therefore the two materials share physical properties and a discussion of the physical properties of the former material naturally also concerns the latter. HOPG is synthesized from carbon rich gases, decomposed and adsorbed onto a surface (pyrolysis), subsequently heated to high temperatures (~3000 K) under high pressure (several atmospheres). The fabricated material consists of large graphitic domains (several μm) with an angular variation of the c-axis direction of less than one degree, hence the term highly oriented. Because of its properties being close to the ideal graphite crystal, with a low defect density and highly anisotropic properties, HOPG is frequently used as a model system in research. To name a few application contexts, it is being used as calibration references in scanning probe microscopy (SPM) and X-ray diffraction measurements, as substrate in temperature programmed desorption (TPD) experiments or as a source of graphene devices [12, 61, 62].

4.3.2 Glassy carbon

Glassy carbon (GC) is fabricated from precursors consisting of long polymer chains, which are treated at high temperatures (typically 1300 K up to 3000 K), thereby being relieved of non-carbon materials and graphitized. The fabrication process leads to a material structure composed of entangled, micro-sized strips, with a graphite structure[12, 63-65]. The main constituents of GC materials are sp^2-hybridized carbon atoms although in between the graphitic domains there are domains of amorphous carbon. The entangled graphite domains are randomly orientated and therefore, GC is essentially isotropic. However, since the graphitic domains are very small (a couple of nanometers) and since amorphous domains are also present, GC generally has a higher content of edge and defect located carbon atoms than crystalline graphite.

The term "defect" refers to a collective set of carbon atom arrangements that are not in the ordered graphitic structure, i.e. where the atomic surrounding deviates from that in a perfect graphite crystal. Such defects can be edge sites of several kinds, missing atoms in the graphite lattice or just arrangement of carbon atoms that do not have the same local or semi-long range arrangement as in crystalline graphite.

Many of the spectacular properties exhibited by GC are attributed to the random ordering of the graphitic strips. First of all, because GC is completely isotropic the physical properties of the material are not different for different directions in the solid. The density is significantly lower than for graphite yet the permeability to gases is very low and the material is chemically inert. This is often ascribed to the pores in the material being closed and thus impermeable to gases[12]. Another consequence of the porous structure is poor thermal conductivity and a low thermal expansion coefficient. Like graphite GC is very durable to high temperatures and is mechanically stable at temperatures as high as 3000 K.

4.3.3 Graphitic amorphous carbon

Amorphous carbon films can be fabricated in several different ways, resulting in fundamentally different compositions and properties of the materials depending on the hybridization state of the constituting carbon atoms. Much attention has been devoted to the fabrication of diamond-like thin films due to their useful properties, such as extraordinary hardness and chemical inertness. These films can conveniently be prepared by chemical vapor deposition (CVD) techniques and are characterized by a significant concentration of sp^3 bonds.

By altering the process conditions in the CVD-process or using a graphite source to evaporate carbon by e.g. laser ablation or electron beam irradiation in high vacuum (~10-6 Torr), thin films with preferentially sp^2-hybridized carbon can be prepared. Under these conditions a graphitic, amorphous carbon film is grown on the surface. At very similar process conditions, the properties of the carbon film can vary slightly, but the main properties are those of a material dominated by sp^2-bonds as confirmed by electrical conductivity, XPS, and Raman measurements[66, 67]. These films are also desirable in many practical contexts, e.g. where strong optical absorption is wanted, or in high-temperature applications. In addition, deposition of thin films has been used to prepare graphene layers on surfaces, with the ambition to facilitate large-scale production of this scientifically and technically interesting material.

4.4 Optical properties of crystalline graphite

Due to the anisotropy of graphite crystals, the optical properties vary strongly depending on the polarization of the irradiating light. Selection rules apply differently for light polarized along the ab-planes and the c-axis, allowing different electronic transitions. Several theoretical and experimental studies have been devoted to map out the optical properties for both crystal directions[58, 60, 68-76] and reasonable consensus has been reached for the ab-direction. For light polarized parallel to the c-axis, on the other hand, observations are more scattered. This is related to the quality of the surfaces that can be prepared for the two crystal directions. Perfect ab-plane surfaces are easy to prepare due to the strong bonds in the ab-direction and the weak inter-planar bonds, whereas perfect surfaces parallel to the c-axis are difficult to prepare, for the same reasons.

4.4.1 Parallel to the ab-plane

Fig.4.4.a shows an optical reflectance spectrum from a pristine HOPG surface in the wavelength interval 2500 – 200 nm (~0.5 – 6.2 eV). The measurement is done with a spectrophotometer, equipped with an integrating sphere detector and with the light polarized parallel to the basal plane surface (ordinary polarization). This spectrum agrees, qualitatively, well with previously published results[71, 72] and the main features that can be observed are a continuous decay in reflectance from the longest wavelengths and a sharp peak at ~250 nm (~5 eV).

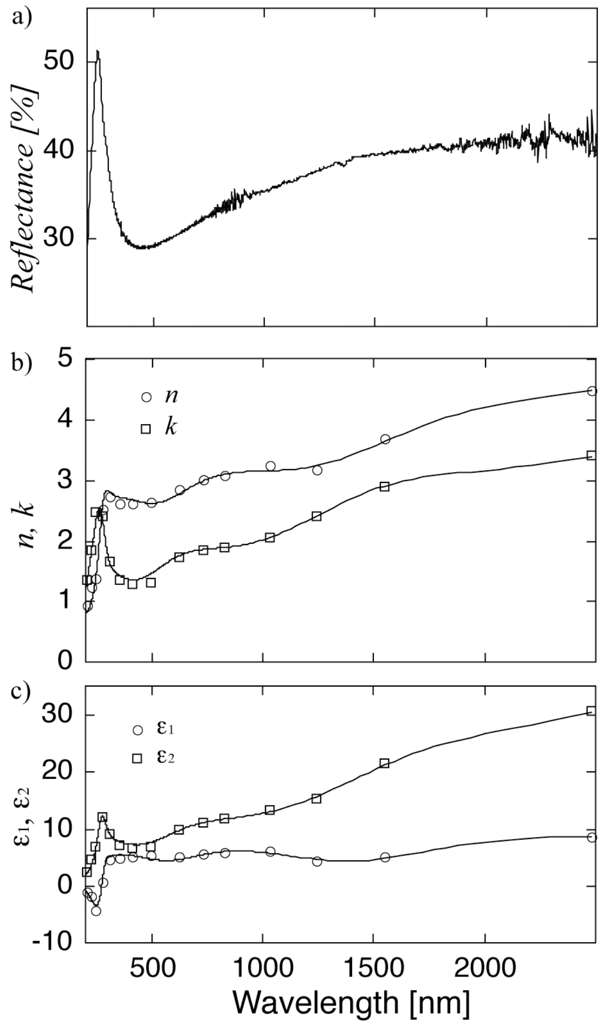

Figure 4.4 a) Reflectance, b) refractive index and c) dielectric function for light polarization parallel to the graphite basal plane (taken from Paper III).

For light polarized parallel to the ab-plane, selection rules are in favor of optical transitions between states with similar symmetry (π-π* or σ- σ*). Since σ-σ* transitions have a large band gap, optical properties for wavelengths longer than ~200 nm are believed to derive predominantly from transitions within or between the π-bands[60, 72]. At very low energies (below ~1 eV) both intra-band (free electrons) and inter-band transitions play important roles for the optical properties. Hence, the reflectance of graphite drops sharply from close to 100% at very long wavelengths (due to the free electrons) to significantly lower values in the near-IR and visible part of the spectra.

Since π-π* inter-band transitions are allowed already at very low energies, graphite absorbs and reflects light all the way from the near IR, through the visible and into the UV-region. A saddle point in the (π-π*) band structure, close to the M-point, then gives rise to stronger optical transitions for light with ~300-250 nm wavelength (~4.1 – 5 eV). This is the reason for the observed reflectance maximum at ~250 nm in fig.4.4a.

The complex refractive index, $n_r = n + ik$, and the dielectric function, $\varepsilon = \varepsilon_1 + i\varepsilon_2$, can be calculated from the reflectance spectrum. In fig.4.4.b and c, experimental and theoretical values for these constants for graphite are displayed (taken from Paper III). The imaginary parts of the dielectric function and the refractive index, k and the ε_2 respectively, exhibit high values throughout the whole spectral region, which is characteristic for strong inter-band transitions and consequently strong optical absorption. Both values also exhibit peaks for slightly longer wavelengths (263 and 277 nm, or ~4.5 and 4,7 eV respectively) than the reflectance, as expected from the presence of the strong optical transition at these wavelengths[58, 68, 70, 77].

In addition to the intra- and inter-band transitions in graphite, three different plasmons are observed; one at very long wavelengths >6.2 μm (~0.2 eV) and two in the UV at ~177 and 50 nm (~7 and 25 eV)[68, 69, 72, 73, 78]. These plasmons correspond to collective oscillations of the free π-electrons, all π-electrons and all the valance electrons (π and σ), respectively, and coincide with zero values in the ε_1 parameter. The presence of the π-plasmon (all π-electrons) can be anticipated in fig.4.4.c, where ε_1 attains negative values at ~273 nm (~4.5 eV), traverses a minimum and increases again towards the plasmon wavelength.

4.4.2 Perpendicular to the ab-plane

The optical properties of graphite irradiated by light polarized parallel to the c-axis (extraordinary polarization) are not as well established as those for the ab-plane. However, most researchers report a fairly constant and weaker optical activity in the 2500 – 200 nm wavelength region for the former polarization[58, 68, 70, 71]. Although peaks are observed at similar positions as for the ab-polarized light, these are much less pronounced than for ordinary polarization.

For extraordinarily polarized light, selection rules are in favor of transitions between bands with different symmetry. Therefore the most important features of the optical properties for this crystal direction derives from π-σ^* transitions. However, the π-π* transitions are believed not to be strictly forbidden, only less probable, and it has been suggested that the structure observed in the near-UV are due to the same π-π* saddle point transition as that responsible for the peak in the basal plane spectra[58, 68].

The optical properties, as described by the refractive index and dielectric functions for the extraordinary polarization, are similar to those of the ordinary polarization direction. The difference is that both the real and imaginary parts of both functions are much smaller. In addition, all four parameters are positive for the wavelength interval 2500 – 200 nm. In summary, the optical properties of graphite irradiated by light polarized parallel to the c-axis are those of a transparent material, or at least much less absorbing than the basal plane graphite.

4.5 Optical properties of glassy carbon

There is considerably less work addressing the optical properties of GC as compared to crystalline graphite. However, since this material predominantly consist of graphitic domains, without preferential orientation, it is not surprising that the optical properties of the two materials are similar. GC also exhibits high reflectance for wavelengths in the IR-part of the electromagnetic spectrum, somewhat lower reflectance for visible wavelengths and a peak followed by a sharp drop in the near-UV. Overall, the reflectance of GC is weaker than that of basal plane graphite. In addition, the reflectance peak is shifted to slightly longer wavelengths for the isotropic carbon material[72, 79, 80]. These observations agree well with what would be expected from a material with intermediate, or mixed, optical properties between those of basal plane- and c-axis graphite.

4.6 Optical properties of amorphous carbon

Optical properties of amorphous carbon films, like most other properties, vary with the composition of the films[81-83]. However, for graphite-like amorphous carbon films, optical properties are reminiscent of those of GC. The main features are strong reflectivity (dropping from ~100%) for long wavelength light (IR), weaker reflectance (less than 20%) in the visible regime followed by a sharp drop for UV wavelengths (~200 nm).

4.7 Raman spectrum of crystalline graphite

Several different vibrational spectroscopy techniques that facilitate characterization of the bond strength and type in graphite materials are at hand, each with its own pros and cons. A technique, with the benefit of being non-destructive, versatile and with an excellent lateral resolution (~ 1 μm) is Raman spectroscopy. In a Raman scattering event a photon is in-elastically scattered, either creating or annihilating a phonon (quantized lattice vibration). The two scattering events are termed Stokes and anti-Stokes scattering, respectively. The requirement for Raman scattering to occur is that a dipole moment is induced in the material during irradiation. Subject to this selection criterion, there are two fundamental modes that are Raman active in graphite, which give rise to peaks termed G (for graphite) and D (for defect). These two modes correspond to Raman scattering with phonons of E_{2g} and A'_1 symmetry respectively (fig.4.5)[84, 85]. In the molecular picture, these correspond to the stretch- and breathing-modes in the carbon rings.

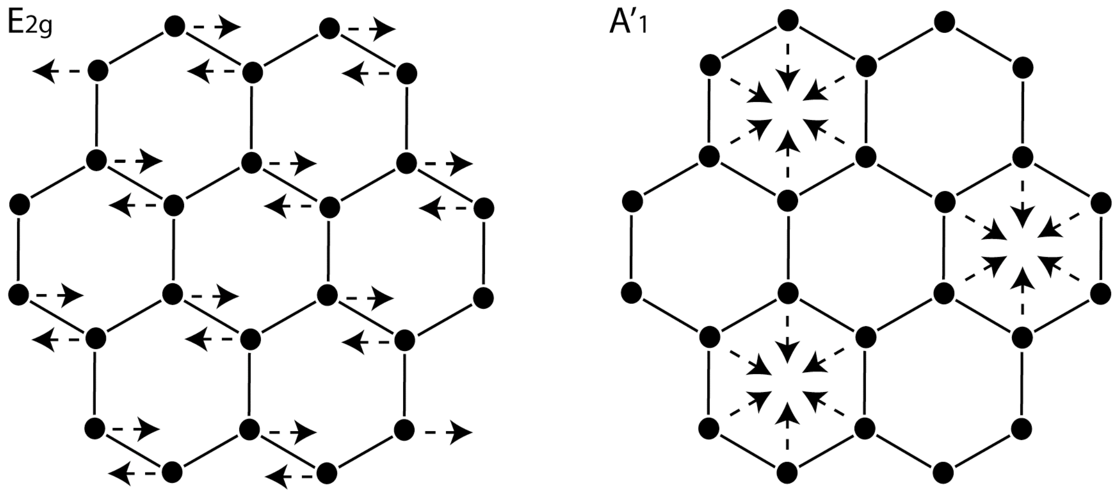

Figure 4.5 The G and D-peaks in graphite stems from the fundamental modes with E_{2g} and A_1' symmetry (reproduced after [86]).

In a perfect graphite crystal, the only fundamental mode that is excited is the G-mode. The elementary steps behind this Raman mode consists of the excitation of an electron-hole pair and subsequent excitation of an optical phonon at the Γ-point in the Brillouin zone (corresponding to low momentum) before re-emission of the photon [84, 87]. This scattering event fulfils the fundamental Raman selection rule, given by the momentum conservation condition, $q \approx 0$, where q denotes the phonon momentum. The wavenumber of the Raman shift is 1582 cm^{-1} (196 meV), which is a comparatively high value, reflecting the strength of inter-atomic bonds in graphite. Due to the high energy associated with the in-plane vibrations, there are few phonons excited at ambient temperatures. This is the reason for the excellent thermal conductivity of graphite in direction of the basal planes. The G-peak in graphite, under normal conditions has the shape of a narrow single Lorentzian function (see fig.4.6).

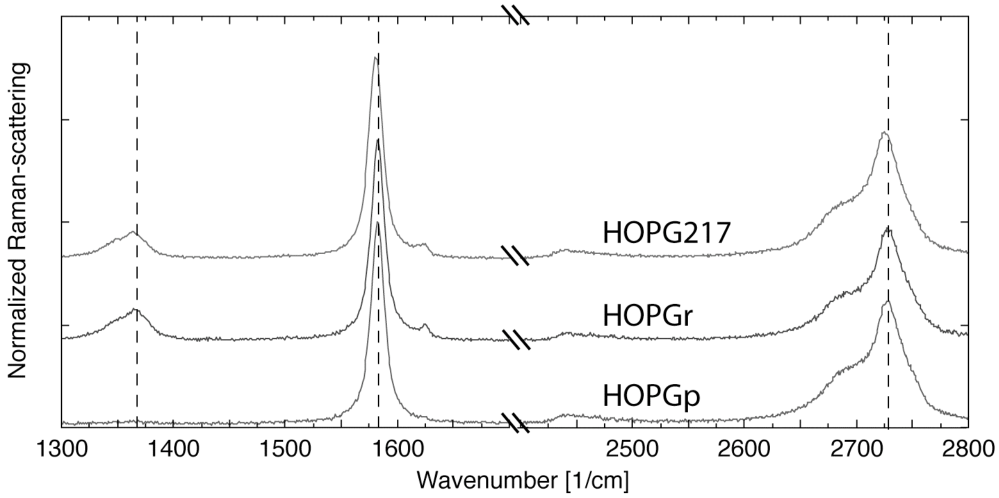

Figure 4.6 Raman spectrum from pristine (HOPGp), defect (HOPGr) and nanostructured graphite (HOPG217) from Paper IV. Single lorentzian G-peak at 1582 cm^{-1}, and the split D, D' and G'-peaks at ~1350, 1620 and 2700 cm^{-1} respectively.

The D-peak is only observed for defect graphite (fig.4.6). The reason is that it stems from a double resonance process[84, 85, 87] schematically described in fig.4.7. Initial excitation of an electron hole-pair constitutes the first of the two resonances. Secondly an optical phonon, around the K-point in the Brillouin zone, scatters the excited electron to another allowed electronic state around the K-point or the K'-point. Since the phonon scatters the electron to another allowed state, this process is also resonant, hence a double resonance process. The electron is finally scattered back to the original state and re-emits a photon. Depending on the inelastic electron phonon scattering event, the wavenumber for the D-peak is ~1350 cm^{-1} or ~1620 cm^{-1}. In the former case the electron is scattered to the K' vicinity and the corresponding peak is termed D and in the latter case, for scattering to the K-point vicinity, it is termed D'. However, due to the double resonance character, both the D- and the D'-peaks are linearly dispersive with the energy of the exciting laser. This means that, depending on what laser wavelength is used to cause the initial excitation, phonons with different energies are excited. For the D-peak this is manifested as a gradual shift of phonon energy from ~1300 cm^{-1} to 1400 cm^{-1} when the wavelength of the laser light is changed from 825 to 350 nm (1.5 – 3.5 eV)[84].

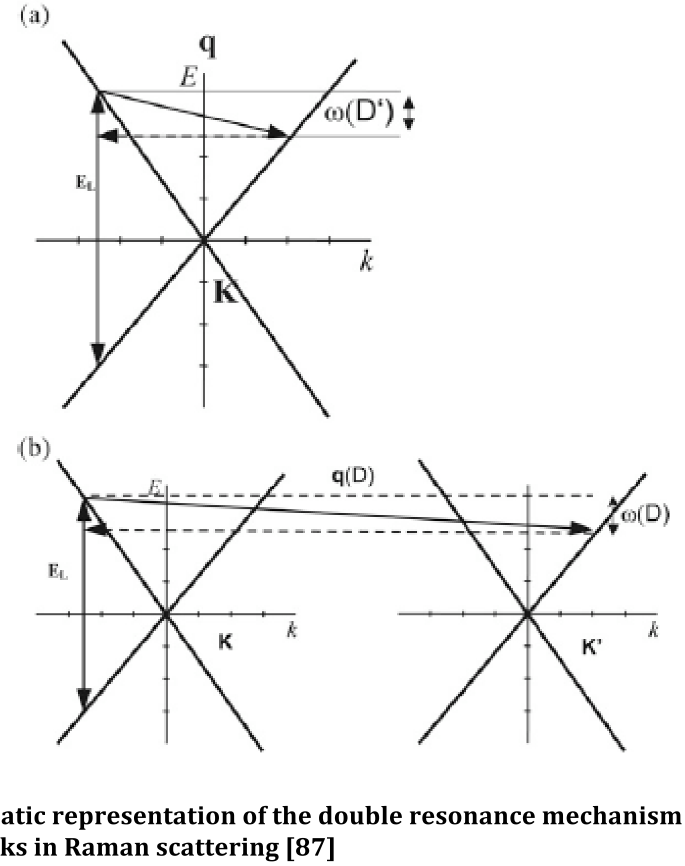

Figure 4.7 Schematic representation of the double resonance mechanism behind the (a) D'- and (b) D-peaks in Raman scattering [87]

The third major Raman peak observed for graphite is the G'-peak (alternatively referred to as the 2D-peak) at around 2700 cm^{-1}. This peak is attributed to a similar process as the D-peak, with the exception that two phonons, with opposite momentum, are involved in the electron scattering process. Therefore, this second order mode does not require the presence of defects and is observed also for pristine graphite, with a wavenumber twice that of the fundamental D-mode. Because the mechanisms behind the G'- and D-peak are similar, the G'-peak is also linearly dispersive with the laser energy although with a two times bigger shift, since two phonons are involved.

In addition to the peak shift with shifting laser energy, the G'-peak is also split into several overlapping Lorentzian peaks. This is attributed to the split of the π-bands and the phonon bands, due to interaction between adjacent layers. Therefore, the shape of the G'-peak contains valuable information about the stacking of a graphite material. A distinctly split peak is the signature of a well-ordered stacking sequence as demonstrated in fig.4.6. In turbostratic graphite and in single layer graphene, on the other hand, a single G'-peak is observed. A similar behavior can be observed for the D-peak.

Since defect scattering is required in order to conserve momentum in the scattering process responsible for the D-peak, this peak is only observed for graphite with a substantial amount of disorder. This requirement can be used to determine the degree of disorder in a graphitic material[84, 88, 89]. An increasing amount of impurities or lattice defects shows up as an increasing intensity of the D-peak relative to the G-peak. This has been used to estimate the size of crystallites in graphite materials via the equation:

$$L_a = \frac{560}{E_l^4}\left(\frac{I_D}{I_G}\right)^{-1} \qquad \textbf{Eq. 4.1}$$

where, L_a is the lateral size of the crystallites (in nm) E_l is the energy of the exciting laser light (in eV) and I_D and I_G are the integrated area of the D- and G-peaks respectively[88]. Such an analysis provides an estimate of the average crystallite sizes of the entire volume being probed by the laser and assume that the material have a uniform morphology.

In addition to the shifts of the Raman peaks due to the rather exotic double resonances discussed above, other more general shifts are frequently observed in Raman spectroscopy. Reasons for such shifts can be changes in the chemical environment close to the probed bond[90]. In addition, Raman peaks can shift substantially due to application of external forces (e.g. electric or mechanical) or temperature changes in the material [85, 91, 92]. The latter effect is reversible and attributed to softening of the phonons due to population of higher energy phonon-modes in combination with decreasing bond strength upon thermal lattice expansion.

These peak shifts are described by the equation

$$\Delta\omega = (\chi_V + \chi_T) \cdot \Delta T$$ **Eq. 4.2**

where, $\Delta\omega$ is the shift in phonon wavenumber, χ_V and χ_T are the temperature coefficients and ΔT is the change in temperature. The two temperature coefficients are attributed to the temperature-driven volume expansion and to the pure temperature change, without volume expansion but with population of higher order phonon states, respectively.

For graphite, temperature changes have been shown to affect Raman spectra, giving rise to substantial shifts in the positions of all Raman peaks[93-96]. However, the Raman active phonon-modes are associated with in-plane lattice vibrations, but thermal expansion along this crystal direction is very small. Therefore temperature shifts of the peaks are attributed, predominantly, to the pure thermal effect described by the χ_T-parameter while the χ_V-coefficient for graphite is practically zero. Although somewhat different values of the χ_T-coefficent have been reported, calibrations done with a well-controlled external heat source indicates that χ_T = -0.031 cm^{-1}/K for the G-peak shift in graphite[96].

Thermal peak shifts in Raman spectroscopy are useful, not only for determination of the material's global temperature, but also for the local temperature. Since intense laser light is used in Raman spectroscopy, there is always a concern that the laser beam might locally heat up the material during measurements. Temperature sensitive materials can undergo unwanted structural and chemical changes due to the laser induced heating. For pristine graphite this is considered to be a minor problem though, both because graphite is a relatively inert and temperature-stable material and because the thermal conductivity is high along the basal plane directions. Therefore, laser induced heat can easily be dissipated to material outside of the irradiated region, giving rise only to a modest temperature change in a larger part of the crystal.

4.8 Raman spectrum of glassy carbon

The main features of the Raman spectra for GC-materials are the same as those of defective graphite; the G-peak at 1582 cm^{-1} and the D-peak at ~1350 cm^{-1}. However, the exact peak positions and widths vary considerably between different GC samples depending on the fabrication process, particularly on the annealing temperature. A general observation for amorphous, graphitic carbons however, is that the peaks are much broader than in pristine graphite. For GC, the D- and G-peaks are still clearly resolved but the D'-peak appearing at ~1620 cm^{-1} is merged with the G-peak, which thus appears shifted to higher wavenumbers (~1590 cm^{-1})[97, 98]. The width of all the Raman peaks in GC decreases significantly as a result of annealing temperatures, as does the intensity ratio I_D/I_G. Both of these changes derive from the increasing order and growing size of the graphitic domains in the material[98].

In addition to the fundamental Raman modes, GC also displays the overtones, observed for graphite above 2300 cm^{-1}. However, since there is no ordered stacking of the graphitic domains in this material, there is no well-defined inter-planar coupling giving rise to splitting of the Raman D- and G' modes as in crystalline graphite. Therefore these appear as single, broad peaks as in turbostratic graphite.

4.9 Raman spectrum of amorphous carbon

For graphitic amorphous carbons the two main Raman peaks, G and D are always present. In similarity with GC, the observed Raman peaks for other amorphous carbons also have significantly broadened peaks as compared to graphite. This peak broadening is a signature of the disorder in the material, especially the D-peak width. For highly disordered amorphous carbon, the peak broadening is large enough so that the two main peaks merge together.

In addition to the broadening, shifts in the positions of both G- and D-peak are observed for amorphous carbons. The position of these peaks also depends on the wavelength of the exciting laser. This is in contrast to the observations for graphite and glassy carbon, where only the D-peak is dispersive[84, 99]. The reason is that for very small graphitic clusters, the electronic and vibrational properties are influenced because the de-localized π-electron gets a more localized character[99]. Graphitic clusters of different size therefore have different electronic and vibrational properties, and therefore different size clusters are selectively excited by different wavelength light. Both G- and D-peaks shift to lower wavenumbers for longer wavelengths.

The intensity ratio I_D/I_G is another characteristic feature of amorphous carbons[66, 84, 99]. For carbons that consist essentially of crystalline graphite, the ratio increases with increasing number of defects since I_D derives from Raman scattering with the breathing mode of carbon rings, allowed due to the double resonance process involving scattering with lattice defects. However, at a point where the defect density becomes so high that many of the carbon rings are destroyed, the D-peak intensity starts to decrease again. Hence, for crystalline graphite with few defects, the G-peak is more intense than the D-peak. In GC, which has relatively large crystalline graphite domains but a high concentration of defects, the D-peak dominates. For amorphous carbons on the other hand, where the graphitic clusters are very small and defects are common, the G-peak can again dominate over the D-peak. Therefore, the I_D/I_G–ratio has to be interpreted carefully and with some basic knowledge of the microstructure of the investigated material.

Graphitic amorphous carbon materials are composed of sp^2 -hybridized atoms with some contributions of sp^3-carbon. Therefore, one would expect to get a contribution to the Raman spectra from vibrational modes attributed to these bonds, at ~1060 cm^{-1} and ~1332 cm^{-1}. However, the cross section for excitation of these modes with visible light is about 55 times lower than the modes attributed to sp^2-hybridized carbon and therefore they are not easily distinguished unless the material has a significant amount of diamond-like carbon[84]. In addition to these sp^3-attributed peaks, frequently a peak at around ~1500 cm^{-1} is observed for amorphous carbons[66, 100]. However, the origin of this peak is somewhat unclear.

4.10 Oxidation of crystalline graphite

Crystalline graphite is a chemically inert material, resistant to most acids, alkalies and corrosive gases. However, at defects and step edges, surface compounds can be formed and reactions may occur. In addition, foreign species can be intercalated in between the atomic layers of graphite[12, 59]. The main exception to the chemical resistance of graphite is its reactivity towards the column VI elements. Of these, the by far most important reaction is that with oxygen and oxygen containing species. A major part of today's energy production derives from the combustion of coal, which in essence is oxidation of graphite. Therefore, the oxidation of carbon with gaseous species is one of the most important chemical reactions for modern (and ancient) society and a detailed understanding of the mechanism very valuable. Consequently an extensive amount of research has been conducted, aiming at clarifying the mechanism behind oxidation of graphitic carbon by gaseous species [51, 53, 101-109]. Although consensus has not been reached regarding the exact microscopic details of this reaction there are fundamental properties that are well known.

4.10.1 Experimental observations

Experimental observations show that graphite is oxidized preferentially at step edges or near lattice defects, where higher electronic densities are available and the atoms are more weekly bound to the surrounding lattice. Under the proper conditions (gas pressure, temperature etc.) the oxidized carbon atoms near steps and edges can desorb into the gas phase as CO or CO_2 causing etching or combustion of the graphite material. The preferential attack of edge- and defect-located carbon atoms is manifested as higher etch rates in directions parallel to the basal plane surface than in the perpendicular direction. This leads to lateral motion of defect lines from point defects, to form circular or hexagonal pits and migration of step edges over the surface[53, 103, 110]. In general, the pits are wider than they are deep, as a result of the anisotropic etch rates, and their detailed shapes depend on the gas used in the oxidation process. Hydrogen-containing gases tend to form hexagonal pits while etching in hydrogen-free gases result in circular shapes. This difference is believed to derive from the preferential adsorption of hydrogen atoms to the zig-zag edges of the graphite planes, which passivate these sites. Consequently arm chair edges are preferentially etched leading to the hexagonal shape of the pits[102].

In addition to the different shapes of surface defects observed for different gases, it has also been observed that reaction rates are different for different gases. Comparison between etch rates in H_2O and CO_2 and the etch rate for pure O_2 exhibits significantly higher rates for the latter gas[102]. There is also a distinct difference between etching in molecular oxygen-containing gases and in atomic oxygen (e.g in RF or microwave oxygen plasma). For oxygen plasmas, etching is observed already at temperatures around ~400 K, whereas etching in molecular oxygen occurs at appreciable rates at temperatures above ~900 K [51, 53, 101, 111]. In addition, etching in molecular gases is more anisotropic than the corresponding process with atomic oxygen. In the latter case, the number of pits and the overall surface disorder increases steadily with the applied etch time, whereas molecular oxygen preserves the number of pits and the ordered surface structure[53]. Only at elevated temperatures (above ~1150 K), where molecular oxygen can decompose to atomic oxygen at a significant rate, are new defects in the basal plane graphite induced in molecular oxygen[103].

4.10.2 Theoretical considerations

Several detailed theoretical studies have been devoted to explaining the oxidation of graphite theoretically[102, 104, 105, 112-118]. Although not presenting complete agreement on the various details, some general conclusions can be drawn from these studies. The fundamental steps of the reaction are: i) Adsorption of oxygen, ii) formation and re-arrangement of surface carbon-oxygen complexes and iii) desorption of the reaction products CO or CO_2.

It is commonly agreed that oxidation of graphite is favored at step edges and defects in the lattice. At these sites, adsorption of both molecular and atomic oxygen is an exothermic process, with low or no activation barriers. Adsorbed molecular oxygen can then, depending on the adsorption site and temperature, either stay in molecular form, or dissociate due to charge transfer from the graphite. Therefore, oxygen complexes are preferentially formed at or near these edge sites. However, while molecular oxygen requires a defect or step edge to adsorb and dissociate, the more reactive atomic species adsorbs readily even on the defect-free basal-plane surface. Because carbon atoms at step edges and defects bind oxygen more strongly than basal plane carbon, these sites are oxidized first. For the oxidation process to continue, the oxygen complexes need to be desorbed, as CO or CO_2, to create new active sites for further adsorption and dissociation of oxygen.

While oxygen adsorption and dissociation are reported to be exothermic and with low or no activation energy at defect sites, desorption of the reaction products is a highly endothermic process. Therefore, many authors claim the rate-determining step in graphite oxidation to be desorption of the reaction products as CO or CO_2[102, 104, 105, 112, 114, 116, 119]. There are many contributing components to this process. Firstly, the temperature of the sample plays an important role. At higher temperatures, thermal energy is available, which facilitate desorption of the species. A similar contribution comes from the exothermic energy associated with oxygen adsorption onto the surface. This energy is of course substantially higher when atomic oxygen is adsorbed, since the energy-cost associated with oxygen-dissociation is then paid by an external source. Another contributing component, to the rate of liberation of reaction products, is the local environment close to the desorbing species at edges or defects. Oxygen atoms adsorbed on adjacent edge or basal-plane surface sites can significantly lower the binding energy of the oxygen complexes and thereby lower the activation energy for oxidation[102, 104, 114, 120]. Since atomic oxygen readily binds to basal-plane sites, the latter argument also helps to explain why atomic oxygen etches graphite more easily than molecular species.

A mechanism for graphite oxidation in molecular oxygen, suggested by [114] is presented in fig.4.8

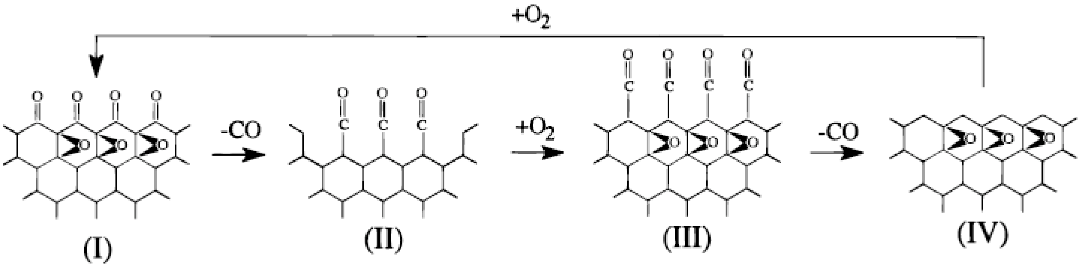

Figure 4.8 (I→II) Oxygen atoms adsorbed at edge sites, with adjacent basal plane adsorbed oxygen, desorb as CO. Surface oxygen flips over to the edge sites forming carbonyl groups. (II→III) Further oxygen adsorbs on the basal plane next to the carbonyl groups, which are (III→IV) desorbed as CO. With new reactive edge sites, oxygen can again adsorb to form the initial state I.

In addition to the ability to bind reactive species to basal plane graphite, oxygen plasma contains ionic species, which are accelerated towards the graphite surface by electric fields. These ions have a higher kinetic energy than those associated with the average thermal velocities, which adds an extra mechanism to the graphite oxidation in plasma, namely sputtering. Such effects can induce new point defects by the removal of basal plane atoms, or assist in desorption of the reaction products. Consequently, etch rates of graphite in an oxygen plasma depend both on the impingement rate and energy of the ions and on the presence of surface bound oxygen species.

4.11 Oxidation of glassy carbon

Glassy carbon, like graphite, is well known for being chemically inert. Similarly to crystalline graphite, it is not attacked by acids or halogens under ambient conditions. However, like graphite, GC is sensitive to molecular oxygen at elevated temperatures and atomic oxygen near room temperature. In molecular oxygen the two materials exhibit very similar etch rates, GC being slightly more inert than HOPG[51]. It should be noted though, that GC etch rates are very sensitive to the presence of impurities, which in turn is a sensitive function of the preparation conditions. Therefore, oxidation rates can vary significantly between different quality samples[12, 121]. In atomic oxygen, on the other hand, GC is etched 1.4 times faster than HOPG[51]. Naturally, this value also depends on the quality of the materials.

Since, GC-materials are isotropic, etch rates are equal for the different directions in the material. Different sub-domains, on the other hand, may exhibit differences on a microscopic level[63]. However, this mostly affects surface properties on the local, atomic scale whereas on the nano- and micro-meter scale the etching is still isotropic, as observed in Paper II and by others[122].

4.12 Oxidation of amorphous carbon

Chemical properties of amorphous carbons can vary significantly between different types of samples. Observations are that most sp^2 dominated amorphous carbons are oxidized more easily than both HOPG and GC when subject to molecular oxygen. In atomic oxygen, on the other hand, results are more scattered[51]. As discussed earlier in this chapter, lattice defects and edge sites are the most important sites for oxidation of graphite-like materials. However, new reaction pathways open up when atomic oxygen is present in the oxidizing gas. These rely on binding of oxygen to basal plane sites of the graphitic domains and on a larger exothermic energy being released in the adsorption of atomic oxygen, since the energy for dissociating the oxygen molecule is provided by an external source[106].

In addition to the different etch mechanisms for atomic and molecular oxygen, different types of carbon hybridization in amorphous materials are present. It is known that *sp*^{2}-carbon is preferentially etched over the *sp*^{3}-species[52]. Oxidation with molecular oxygen requires elevated temperatures and at temperatures where oxidation rates become appreciable a significant restructuring also sets in. This process converts amorphous carbon to more crystalline graphite and reduces the fraction of *sp*^{3}-hybridized carbons[123, 124]. Oxidation with atomic oxygen, on the other hand, can be performed already at room temperature and the *sp*^{2}-carbons are selectively etched. Therefore, the composition of the carbon materials influences the oxidation in molecular and atomic oxygen differently.

Another important factor for the oxidation rate of carbon materials is the porosity. A compact material tends to allow oxygen to penetrate only into the surface layer while porous materials can be oxidized deeper in from the surface. This effectively increases the active area and the number of defects accessible to oxygen and thus facilitate higher etch rates. On the other hand, pores may impose diffusion limitations to the etch process. This is actually a concern for all graphitic materials where pores are created during the oxidation process.

The rate of oxidation is observed to depend on oxygen pressure for many types of carbon[107, 108]. This is expressed as the reaction order in oxygen pressure, which is zero when there is no oxygen dependence and one when reaction rates scale linearly with oxygen pressure. Reaction orders ranging from zero to one are observed during different temperatures and oxygen pressure and for different types of carbon. For a reaction that is limited by oxygen adsorption, a reaction order of one is expected, while for a reaction that is entirely limited by desorption of reactants zero order oxygen dependence is expected. Therefore, different reaction orders point towards different reaction mechanism for various carbon materials and oxidation conditions and also towards different rate limiting steps. However, under circumstances where diffusion of oxygen to the surface or into the interior of the material is limiting the speed of the reaction, this can give a contribution to the observed oxygen pressure dependence, which is then termed apparent reaction order (as opposed to the true reaction order where no diffusion limitations are present). This is thus not a kinetics effect but a transport (of oxygen)effect.

5 Carbon Nanostructures

Carbon nanostructures appear in the universe in many different forms. Examples include interstellar dust, soot particles from different combustion processes, and lately synthetic carbon nanostructures used in different composite materials. Among the carbon nanoparticles, there are various degrees of crystallinity and varying relative concentrations of the different hybridization states of carbon atoms. Here the focus will be on nanostructures mainly consisting of sp^2-hybridized carbon, characteristic for graphitic materials.

5.1 Different types of carbon nanostructures

In amorphous carbon nanostructures, graphitic domains called basic structural units (BSU), with dimensions of a few nanometers are the main building blocks. Between the BSU domains there are regions with carbon atoms with different hybridization states and no preferential crystalline order. Similar to bulk amorphous carbon, the nanosized equivalents can have different relative abundance of disordered versus graphitic material. Most of the naturally occurring carbon nanostructures consist of amorphous carbon.

An important class of carbon nanostructures are soot particles, which are formed as unwanted by-products during combustion of carbon based fuels. The chemical composition and morphology of soot particles vary widely and depend on the details of the combustion process such as temperature and the type of fuel, but can generally be regarded to consist mostly of spherical amorphous carbon nanostructures with diameters in the 10-50 nm range[18, 19]. These amorphous carbon spherules, termed primary particles, are invisible to the naked eye but can agglomerate to form larger particles, which makes the soot visible as smoke.

Since graphite is the thermodynamically most favorable phase for carbon, sufficiently high combustion temperatures tend to drive the morphology of soot particles towards a state dominated by graphitic carbon. In addition to amorphous carbon, different amounts of other elements and compounds, such as hydrogen, sulfates, phosphates, and metal oxides can also be present in soot particles. The sources of these residues are either the original fuel or various additives or lubricants. Due to the large variation in morphology and chemical composition, these nanocarbons exhibit a large variation in physical properties. In particular, the electronic, optical, vibrational and chemical properties are affected by the difference in particle morphology and chemistry.

Another context in which amorphous carbon structures appear is astro -physics and -chemistry. Interstellar dust particles are for practical reasons not as well investigated as soot, other than with far-field optical techniques. However, based on the spectroscopic data, these are generally assumed to be pure carbon structures with a relatively high fraction of graphitic carbon and with diameters typically below 100 nm[22, 23].

In addition to the naturally occurring, or unintentionally generated nanocarbons discussed above, several different synthetic types are manufactured. One of these carbon nanomaterials is the Buckminster fullerene, which form a spherical structure of a graphite sheet, the most famous one consisting of 60 carbon atoms[13]. These structures can be considered as large molecule, rather than nanostructures and will not be considered further here. Closely related to the fullerenes are the carbon nanotubes, which have been subject to extensive research since their discovery (CNT's)[14]. These can be thought of as graphene layers, rolled up to form a tube. They consist of one or several layer walls and have different physical properties (metallic or semi-conducting) depending on the detailed morphology. CNT's are almost entirely graphitic, although some sp^3 hybridized carbons are suggested to participate, due to the shape curvature. Diameters of the tubes are typically one to a few nm, while lengths can extend for several μm.

Various schemes to fabricate nanostructures via nanofabrication strategies, such as EBL, PL and FIB have been demonstrated[125-128]. Conventional nanofabrication techniques have been used to prepare etch masks for reactive ion etching processes. Using this approach, nanostructures have been etched out of graphite, glassy carbon or amorphous carbon surfaces, thus forming structures with similar atomic arrangement as in the solid precursor material[122, 127, 129]. Other approaches that have been demonstrated are deposition of nanostructures from carbon-rich materials on a surface, and subsequent high temperature treatments to convert the precursor material to the desired carbon phase[126, 130]. CNT's are normally fabricated via decomposition of a carbon rich gas on supported catalyst particles. In many studies nanolithography is used to prepare these nanoparticles on which the CNT's grow. A similar technique has been utilized to fabricate carbon nanocones[131-133]. As a consequence of the different fabrication techniques and precursors used, nanofabricated carbon structures with many kinds of different morphologies have been demonstrated. In addition to all graphite-like nanocarbons, different types of diamond like structures are common. However, these will not be discussed here.

5.2 *Optical properties of nanostructures*

Several approaches to solve Maxwell's equations for nanosized objects have been demonstrated in the literature. A particularly important example is Mie-theory, which provides an analytical solution to the equations for homogeneous, spherical particles. These solutions provide a mathematical description of the extinction (absorption and scattering) of light by nanospheres[77]. For nanostructures with other than spherical shapes, simplifying approximations has to be done to find useful solutions to the equations. Alternatively the problem can be solved numerically, e.g. using finite difference time domain calculation (FDTD)[134] or the quasi-static dipole approximation[77]. In any of these methods, the dielectric properties of the nanostructures are an important parameter. Usually, it is assumed that these can be represented by the complex dielectric function derived from macroscopic samples.

Regardless of the applied theoretical approach, solutions to Maxwell's equations, with the proper boundary conditions, reveal optical resonances in nanostructures. These resonances result in different extinction probabilities at different wavelengths. The spectral position for the maximum of extinction depend on the size and shape, as well as on the dielectric properties of both the nanostructure itself and the surrounding material. For nanostructures that are small in comparison with the wavelength of the irradiating light, only the lowest order optical modes (dipole) are excited and the optical spectrum is fairly simple. For larger structures, higher order modes (quadropole, octupole et.c.) are also allowed and the spectrum become richer in details. In particular, it is observed that the spectral position of the optical peaks, shift to longer wavelengths for larger nanostructures. It is therefore possible to determine the size of a nanostructure of a known material by measuring its optical properties.

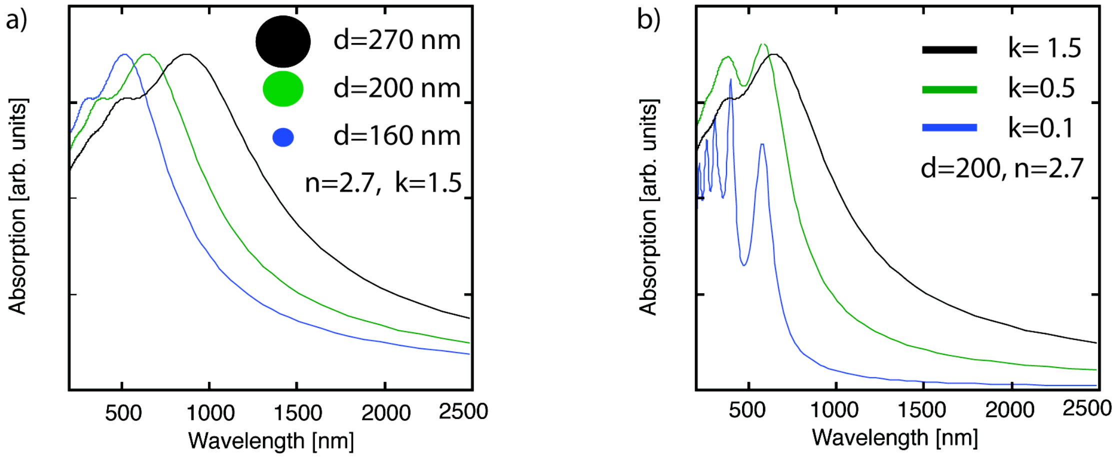

Figure 5.1. a) Mie-theory calculations of the absorption for nanospheres with different size. A constant refractive index corresponding to that for graphite at 640 nm was used (supplementary calculation for Paper III, by T. Pakizeh). b) Mie-theory calculations for nanospheres with diameter d=200 nm, real refractive index n= 2.7 and different values of the imaginary refractive index k. Taken from Paper III.

Fig.5.1.a demonstrates the pure size dependence in the optical spectrum for nanospheres. Calculations performed using a constant refractive index (corresponding to that of graphite at 640 nm[135]) shows that the absorption peaks shift to longer wavelengths for larger nanospheres. In addition to the main peaks, shoulders appear for shorter wavelengths corresponding to higher order modes.

In fig.5.1.b, the Mie-resonances dependence on the imaginary part of the refractive index, k, is demonstrated. Calculations for 200 nm diameter nanospheres, with a constant, real refractive index, corresponding to that of carbon at 640 nm, are shown. In Paper III, it is demonstrated that for a high k-value, corresponding to strong absorption of electromagnetic radiation, the peaks are wide and the different order modes overlap, being difficult to resolve. For the same nanostructures, but with a low k-value, on the other hand, each resonance mode is very sharp and can be clearly resolved[77, 136, 137]. Increasing k-values also result in an increase of the average amplitude of the absorption curve.

Another important nanostructure property that influences its optical properties is the shape. In general, spherical particles exhibit only a single peak per allowed optical mode, regardless of the polarization and direction of the irradiating light. For structures with a lower symmetry, on the other hand, the optical properties depend on the polarization of the light. For example, an elliptical particle exhibit different optical properties for light polarized along the long and the short axes respectively. Therefore, the optical properties of a nanostructure also contain information about its shape and orientation with respect to the incoming light.

5.3 Optical properties of carbon nanostructures

Because of the large variety of nanocarbon compositions, their optical properties also exhibit great diversity. However, a common observation for a large number of different carbon nanostructures is strong optical extinction of UV and visible light[19, 22]. Calculations and measurements regarding structures of different size and shape, and in different types of carbon, exhibit some variations in position and shape of the extinction peak. For spherical structures with diameters around 50 nm and that consist mainly of graphite, the peak maximum is observed for wavelengths between 200 and 300 nm[22, 138]. For other sizes and symmetries of the nanostructures, shifts and splitting of the extinction peaks are observed. There is also a strong influence on the extinction from the type of carbon material constituting the nanostructures. A less graphitic and more amorphous character of the carbon results in a significant broadening of the peak and a shift towards visible light wavelengths.

As seen from the spectroscopic measurements and calculations presented in Papers III and V, our nanofabricated carbon structures exhibit similar optical properties. Fig.5.2 displays measured and calculated spectra of absorption in disc-like graphite nanostructures (published and supplementary data for Paper III). It can be seen that the nanostructures with diameters below 100 nm (the rough surface in fig.5.2.a can be regarded as agglomerations of nanostructures with diameters < 10nm) absorb some light in the visible but with the maximum value between 200 and 300 nm in similarity with what is observed for spherical graphite nanostructures. Larger structures, on the other hand, absorb light more efficiently for wavelengths in the visible and near-IR part of the spectrum.

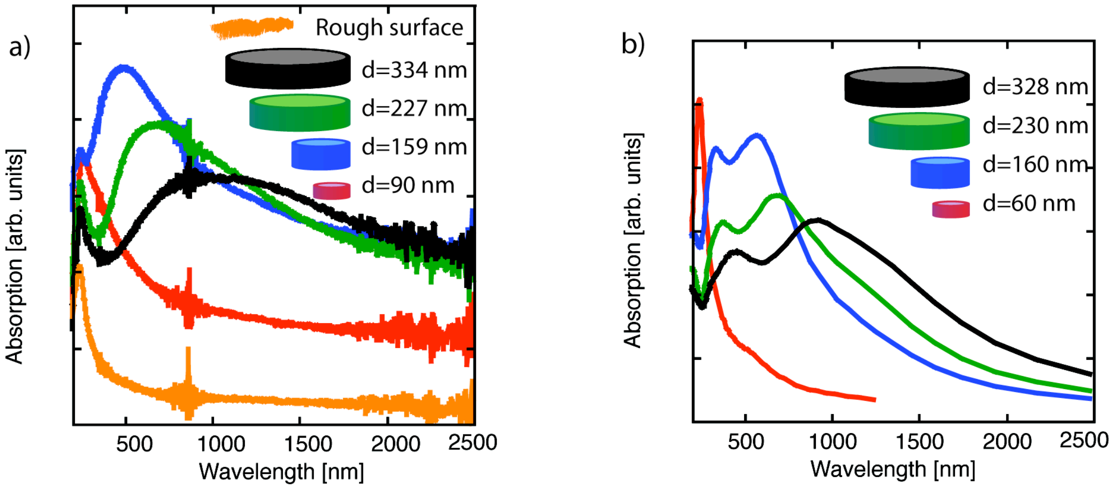

Figure 5.2 Optical absorption of supported graphite nanostructures, a) spectrophotometer measurements and b) FDTD calculations (supplementary data to Paper III).

The observed absorption peaks for carbon nanostructures are often attributed to the intrinsic electronic properties of the material. Indeed, graphite exhibits a reflectance peak at around ~250 nm due to the strong optical activity associated with the π-π* transitions. Therefore, the intensity of the optical resonances observed for carbon nanostructures depend on the relative content of graphite to amorphous carbon constituting the structures. A pure graphite nanostructure would show a stronger and sharper optical activity than a more disordered analog, containing a smaller fraction of hexagonal carbon rings.

Although the electronic properties are influenced by the size of nanostructures, especially for structures with diameters below ~10 nm, the optical properties governed by the electronic structure of the carbon material do not provide the whole explanation of positions and shapes of the extinction peaks. As discussed in the previous section, the optical properties are modulated by the finite size and shape of nanostructures, described by the geometrical resonances in the nanostructures (for spheres, Mie-resonances). In calculations of the geometrical resonances, the material dependence, and hence the strong activity of the π-π* transition, is included via the dielectric function of the material. In such calculations it is assumed that the material properties correspond to those of the bulk material. The calculations shown in fig.5.2.b, predict substantial shifts of the absorption peak maximum and amplitude, as a function of size, in agreement with the experimentally observed trends. Several papers report estimations of the particle size distribution, derived from measurements of scattered or absorbed light in combination with Mie-theory calculations[137, 139, 140].

An additional complication in the analysis of optical properties of graphitic nanostructures is the inherent anisotropy of the material and the accompanying anisotropy of the dielectric functions. For graphite nanostructures with a well-defined orientation and the irradiating light polarized parallel to the graphite basal plane, the anisotropy can be disregarded. The comparatively well-established dielectric function for light polarized parallel to the basal plane surfaces can then be used. If, on the other hand, light is polarized perpendicular to the basal plane, or an amorphous material is considered, the optical properties for the perpendicular direction has to be included. These are not as well established and some variations are found in the reported literature values. For amorphous nanaostructures an average over the lattice directions can be used. Alternatively, dielectric properties derived directly from an amorphous carbon material can be used. However, since the optical properties of carbon materials are closely related to the microscopic properties of the material, care has to be taken to choose an amorphous carbon reference material with a microscopic structure representative for the actual material under study.

5.4 Raman scattering by nanostructures

Electronic and vibrational surface states play an increasingly important role for small nanostructures since the surface to volume ratio increases with decreasing size. In addition, due to confinement of the phonons to a small volume, the fundamental Raman selection rule, $q \approx 0$, where q denote the phonon momentum, is relaxed. This allows for excitation of other phonons than those close to the Brillouin zone centre, Γ, that are excited for samples with macroscopic dimensions. These effects become important for particles with diameters of ~25 nm or smaller and result in shifts of the resonance frequencies[141, 142]. All of these properties are of fundamental importance for the Raman scattering process and therefore Raman spectra for nanostructures can differ significantly from that of a bulk sample of the same material.

In addition to the static changes of physical properties in nanostructures, the limited size of a nanostructure also imposes different transient Raman scattering properties. As discussed in Chapter 4, it is well known that the temperature of a material influences the frequencies and intensities of Raman modes. Both positive and negative frequency shifts can be observed, depending on the mechanism dominating the process in the studied material (volume expansion or pure thermal effect).

Depending on how a supported nanostructure system is heated, significantly different temperature gradients can be observed from the structure to the support material. For the case where the nanostructures are heated via direct absorption of light, the thermal properties of both the nanostructures and their surrounding become important. A nanostructure, suspended in a host material or supported on a surface, exchanges heat with its surrounding effectively via conduction. Therefore, a nanostructure that readily absorbs the laser light used in a Raman measurement, and which is supported on a poor heat conductor, can attain a higher temperature than the support under irradiation. This can be seen as a larger shift of the Raman peaks for nanostructures supported on poor thermal conductors than for identical structures on good conductors[143]. It should be mentioned that the exchange of heat can go the other way as well, from a strongly absorbing matrix material to the nanostructures. In this case the opposite trends for Raman shifts, for nanoparticles supported on substrates with different thermal conductivities, are observed.

In addition, because the surface atoms constitute a significant fraction of the total number of atoms in a nanostructure, the surface properties become increasingly important for decreasing size. The elastic constant for surfaces generally differs from those of the bulk and therefore, thermal expansion properties of nanostructures are different from those of bulk matter[144]. Depending on the elastic constants of the surface bonds, thermal expansion may increase or decrease with nanostructures size. Consequently Raman shifts for nanostructures as a result of temperature changes may differ from that of bulk matter.

As mentioned earlier in this chapter, the cross section for light absorption is drastically different for nanostructures compared to extended samples of the same material. Sharp resonances in the optical absorption spectrum can lead to selective excitation of Raman active modes. The Raman intensity is enhanced if the optical resonance matches the irradiating laser wavelength and/or the wavelength of the scattered light[136, 145]. Therefore, different modes can be enhanced with different strengths depending on how well the energy of the Raman scattered light matches the nanostructure resonance. In addition, if the rate at which the excited vibrations exchange energy with other modes is slower than the rate of excitation, the occupation of phonon modes during irradiation may not correspond to thermal equilibrium. Under such circumstances, material properties derived from relative intensities of different Raman modes (e.g. temperature derived from anti-Stokes/Stokes-ratios), may not be accurate[146].

5.5 Raman scattering by carbon nanostructures

Raman spectra of graphitic carbon nanostructures resemble those of bulk carbon materials[91, 132, 147], the main features being the G- and D-peaks at ~1582 and ~1360 cm^{-1} and their overtones (fig.5.3). However, due to their limited size, the D-peak is present even for nanostructures with nearly perfect graphite order. The exact positions and relative intensities of the different peaks vary with the type of carbon, from mainly amorphous to crystalline graphite, constituting the nanostructures. In addition to the main peaks, several other, less intense peaks are observed for lower wavenumbers, corresponding to modes that are either specific for the nanostructure geometry[148] or Raman active as a consequence of relaxation of symmetry related selection rules [132].

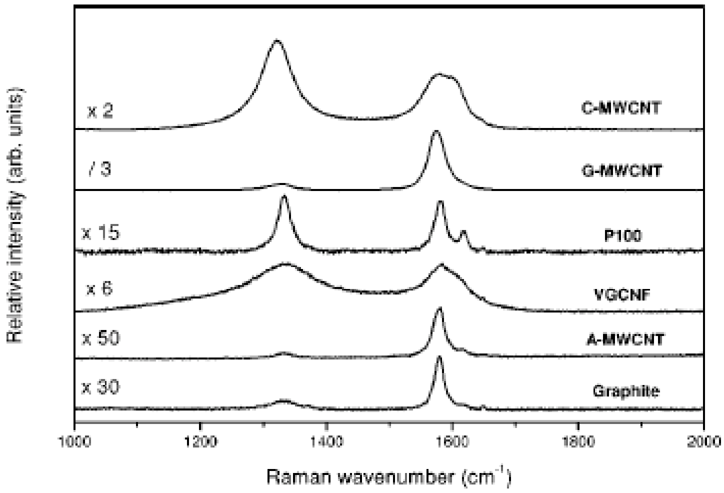

Figure 5.3 Raman spectra for several different carbon structures taken from[91]. Three types of multi-wall carbon nanotubes (names ending with MWCNT), catalytically grown (C-) graphitized (G-) and arc-grown (A-). The other three spectra come from a carbon fiber (P100), vapor grown nanofibers (VGCNF) and crystalline graphite.

Furthermore, Raman spectroscopy has been used to provide information about reversible processes, specific to various nanocarbons. Thermally induced peak shifts have been demonstrated for graphite ribbons, CNT's and carbon fibers and are generally larger than for bulk carbons[93, 96]. At high laser intensities during Raman measurements, peak shifts of several tens of cm^{-1} have been observed. For nanocarbons supported on carbon substrates, preferential heating of the structures by the irradiating laser can be induced. In addition to poor thermal contact with the supporting medium and different thermal expansion properties this can then result in a split of the observed Raman peaks, one corresponding to the temperature of the nanostructure and one corresponding to the support material [149, 150]. Similarly, it has been shown that CNT's suspended over trenches exhibits large peak shifts upon increasing laser power, whereas identical tubes in contact with the support exhibit no shifts under similar irradiation conditions. This is attributed to less effective heat transfer to the support from the free hanging tubes, as compared to the supported ones[151]

Since the population of different phonon modes is related to the temperature of a material, the anti-Stokes/Stokes-ratios (aS/S) can be used to evaluate its temperature. However, for nanocarbons with sharp optical resonances, like CNT's, it is well known that this relation cannot easily be used to determine absolute temperatures[148]. For a given laser power, it has been shown that the maximum intensity of the anti-Stokes scattered light occurs for lower laser energies than for the Stokes light[145]. Therefore, the aS/S-ratio changes with excitation energy and the simplest theory for converting the measured ratios to absolute temperatures will predict different temperatures for different laser energies. Hence, for optically heated, resonant systems, more advanced models are required to deduce the correct temperature taking into account the different cross sections for anti-Stokes and Stokes scattering[146].

5.6 Oxidation of carbon nanostructures

Apart from being interesting from a purely scientific point of view, the stability of carbon nanostructures towards oxidation is relevant in practical applications. For composite materials, containing carbon nanostructures, resistance to oxidation is often desired. Another important topic where nanocarbon oxidation is of outmost importance is in exhaust gas cleaning. Creation and oxidation of soot particles is an important topic and has long been subject to massive research[18, 152, 153]. The main objective is to reduce the content of polluting soot particles in exhaust gases. This is conveniently achieved using particle filters[18]. However, after extensive use, filters are filled with soot particles and start to significantly influence the performance of the combustion process. Therefore, particle filters needs to be emptied on a regular basis. This can be achieved by temporarily switching the conditions in the filter (temperature, gas composition etc.), such that the soot is rapidly combusted to CO and CO_2 (and H_2O, since soot usually also contains hydrogen), leaving the filters themselves intact.

5.6.1 Experimental observations

As for macroscopic carbon materials, the microscopic structure of carbon nanomaterials plays a dominating role for the materials oxidation-resistance. Therefore, activation energies for oxidation of carbon nanostructures are similar to those of bulk carbons. Typical activation energies for combustion of solid carbon materials (chars and graphites) in molecular oxygen are 180 kJ/mol while for nanocarbon materials, values between 140 and 170 kJ/mol are frequently reported[107, 152]. However, as for macroscopic carbons, large variations of microscopic composition in different carbon nanostructures exist and therefore large variations in oxygen resistance are also observed. An illustrative example of this is provided by experiments aiming at purifying samples of CNT's.

Depending on the fabrication method different amounts of carbon by-products are generated. The by-product carbons are amorphous, while the CNT's are mainly graphitic. Therefore, the former carbon nanostructures are more easily oxidized than the latter. As a consequence amorphous carbons can be removed from mixtures with CNT's by oxidation at suitable temperatures. At temperatures up to ~1000 K, amorphous carbons are combusted while it is possible for CNT's to remain essentially intact[131]. However, only a small fraction of the tubes remain, since defects in the samples and presence of catalyzing agents facilitate oxidation. Nevertheless, this example nicely demonstrates that crystalline nanocarbons are more resistant to decomposition in oxygen than amorphous structures. In addition, it can be noted that the tips and sidewalls of CNT's with small diameters are more easily oxidized than the walls of tubes with large diameters. The higher curvature of the former surfaces is responsible for their enhanced sensitivity towards oxidation, which further emphasizes the importance of morphology for oxidation of carbon structures.

Oxidation of soot particles is another topic where a vast amount of information is available[18, 152]. Since the morphology of soot particles depend strongly on the combustion conditions during which they are created (type of fuel, mixing with oxygen, exhaust temperature), particles that are generated under realistic conditions exhibit large variations in oxidation rates. In addition, the presence of other species than oxygen, e.g. OH-groups, NO_2 or a catalyst such as V_2O_5 can influence the reactivity of soot particles. Here, the focus will be on non-catalyzed oxidation in oxygen at temperatures below 1100 K, which is the temperature range that is relevant for oxidation of soot in diesel exhaust systems.

5.6.2 Theoretical considerations

Models describing the mechanisms behind oxidation of nanosized graphitic carbon structures usually consider small sections of a single sheet of graphite, a BSU. This is in complete analogy with the theoretical modeling for oxidation of graphite, discussed in Chapter 4, and it is therefore not surprising that the mechanisms proposed for oxidation of carbon nanostructures resemble those of macroscopic carbon samples. Oxygen molecules and atoms bind exothermically and dissociatively to edge and defect sites of the BSU and desorb as CO or CO_2. The energy required to desorb reaction products from the edge sites is lowered by oxygen bound to adjacent edge and out-of-plane basal-plane sites[104, 114]. Since both adsorption of oxygen and desorption of the reaction products take place at edge and defect sites, a high density of these sites lead to a high reactivity. It is commonly agreed that the most important property for the oxidation rate of soot particles is the number of active sites available for oxidation[18]. However, the active sites also have to be accessible to the oxygen molecules, which is true also for porous macroscopic carbon material, as discussed in Chapter 4.

Nanostructures, because of the large surface to volume ratio, naturally expose a larger fraction of surface area to the surrounding gas than bulk materials. It is well known that oxidation of soot particles take place not only on the surface of the structures, but also in the interior of the particle[18, 152, 153]. The interior of the particle is reached by oxygen via diffusion into the nanostructure pores. These pores open up and expand during oxidation and frequently the active surface area increases with prolonged oxidation. In competition with this effect, at elevated temperatures, amorphous carbon tends to graphitize, thus decreasing the number of active sites. In summary, all these factors influence the reactivity of soot particles and direct correlations between microscopic properties and oxidation rates are not easily deduced.

In view of the discussion above, models describing the reaction rates of soot particles should include the number of active sites as well as the partial pressure of the oxidant. For soot oxidation in oxygen, the temperature dependent reaction rate can be written as

$$r(T) = N \cdot k_0 \cdot e^{\frac{E_a}{R \cdot T}} \cdot p^n \qquad \textbf{Eq. 5.1}$$

where N is the number of active sites, k_0 is the pre-exponential factor, E_a is the activation energy, p is the oxygen pressure and n is the reaction order[18]. Experiments at different temperatures can give accurate values for the activation energy of the reactions, under the condition that the other terms, n, N and p in eq.5.1 remain constant during the reactions. The activation energy is conveniently achieved by taking the logarithm of eq.5.1 and plot *ln(r)* as a function of *1/T*. Such a plot represents the familiar Arrhenius plot and the slope of the curve corresponds to the activation energy of the reaction. However, due to the complicated behavior during soot oxidation, with pore opening and gas diffusion possibly limiting the reaction kinetics, the N and n values are not easily determined. During many oxidation experiments, the number of active sites changes over time due to opening of pores or decrease of size of the nanostructures. In addition, different reaction orders, ranging from close to zero up to one, have been observed for carbon structures with different morphology and size and under different process conditions[107, 152, 154]. This illustrates how complicated the processes of carbon nanostructure oxidation is and how important it is to have good control over the different parameters involved, for proper interpretation of experimental results. Therefore, fabrication of supported arrays of nearly identical nanostructures, whose properties can be precisely controlled and systematically varied, is an advantageous approach. This has been demonstrated in Paper V.

6 Experimental

The focus of this thesis is on fabrication, oxidation and optical characterization of carbon nanostructures. Since the fabrication technique, hole-mask colloidal lithography (HCL) constitutes a large part of the experimental work, it has been described separately, in Chapter 3. In this chapter, additional techniques and experimental equipment of central importance are described. These include, two different systems used for carbon oxidation; an oxygen reactive ion etcher (RIE) and a quartz tube flow reactor. Optical properties have been characterized with spectrophotometry and Raman spectroscopy.

6.1 Oxidation systems

6.1.1 Reactive Ion Etching, RF glow discharges

A plasma is an atomic or (partly) dissociated molecular gas, where a fraction of the electrons are separated from their nuclei. More specifically it is comprised of a mix of atomic, molecular, radical, ionic, excited and neutral species and free electrons. Although locally polarized a plasma is electrically neutral on the macroscopic scale[155]. In lab environments they are frequently applied in etching and deposition processes. An example is the etching of carbon materials, which was discussed in Chapter 4 & 5. Here we will give a short technical description of the used system.

The plasma assisted etching processes presented in this thesis were performed using a commercially available system (Plasma Therm RIE 95m) schematically described in fig.6.1. This is a RIE system operating at RF (13.56 MHz) with the top electrode (the anode) and chamber walls connected to ground and the water cooled bottom electrode (cathode), serving as substrate stage, coupled to the RF generator via a capacitor. Plasma powers up to 500 W and pressures up to 500 mTorr can be applied. The main chamber can be evacuated using a turbopump. Process gases (O_2, Ar or CF_4) are continuously supplied to the system through several small holes in the top electrode to achieve a homogeneous plasma and thus homogeneous etching conditions. There is no explicit temperature control on the system, but temperatures reached in similar systems are typically below 400K. The system is biased only by the natural charge build-up on the cathode, which is due to the higher velocity of free electrons as compared to ions. Self-induced potentials are typically around 160 V under the process conditions applied in this work.

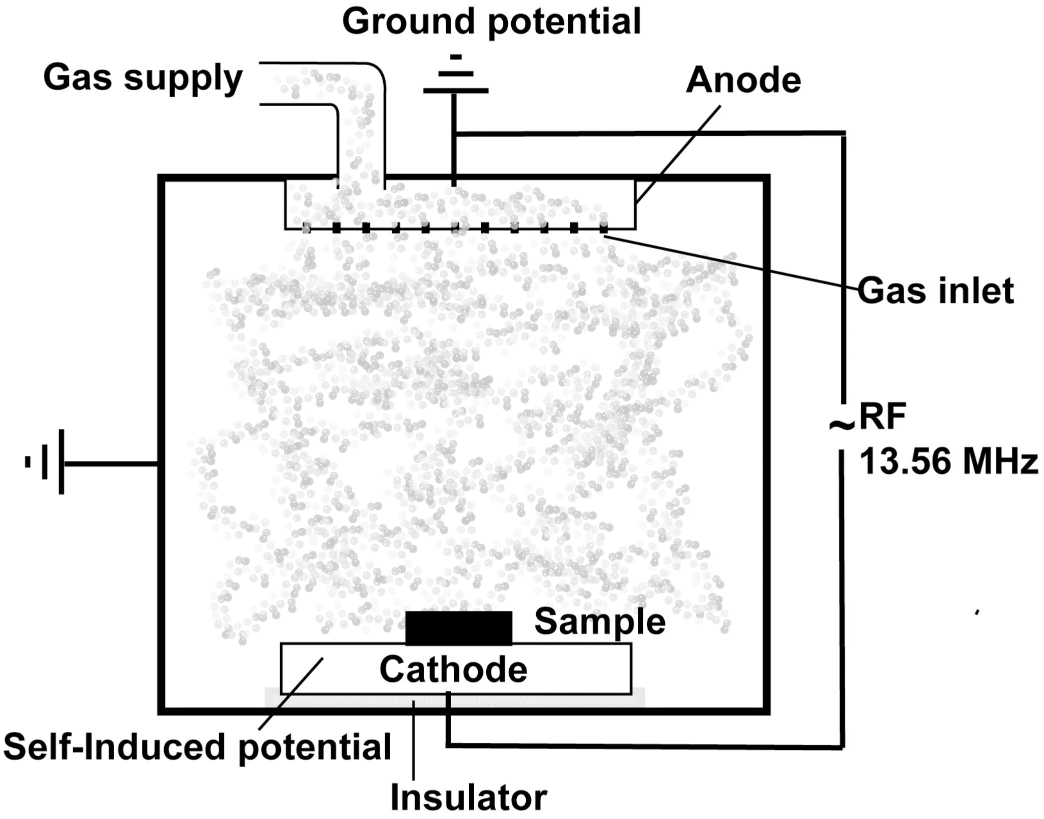

Figure 6.1 Schematic description of the oxygen RIE system used to oxidize the carbon samples.

6.1.2 Gas-flow reactor

The system used to oxidize carbon samples in molecular oxygen at elevated temperatures is a conventional gas-flow reactor (fig.6.2). It consists of a quartz tube (25 mm diameter), which can be heated via a kanthal coil, wrapped around it. Temperatures inside the quartz tube is monitored with two thermocouples and temperatures up to 1000 K can easily be reached. The process gases are introduced into the reactor using gas-flow regulators, and various combinations of gases can be applied. In our experiments we have used 10 % oxygen in Argon. Gas compositions can be analyzed using a mass spectrometer coupled to the gas outlet via a capillary leak. Inside the quartz tube, nanostructured samples are mounted in a vertical position on an oxidized aluminium holder.

6.2 Optical characterization

6.2.1 On-line optical extinction spectroscopy

In addition to the conventional gas flow reactor components, a fiber spectrometer is attached to the gas-flow reactor system shown in fig.6.2. White light spanning the spectral interval between 1100 and 276 nm (Avantes, AvaLight-DH-S-BAL) is brought to the sample through an optical fiber (Avantes, FC-UV400-2), which is terminated with a collimating lens. The fiber is positioned in front of an opening in the heater coil that surrounds the reactor. Since the reactor consists of quartz glass it is transparent to all wavelengths delivered by the lamp and light is readily transmitted.

On the backside of the quartz tube, light transmitted through the reactor and sample is collected using another optical fiber. The fiber is coupled to an array detector (Avantes, AVA-spec 2048) covering the wavelength interval 276-1100 nm. For accurate determination of the optical properties deriving from the nanostructures, reference spectra are taken through the quartz tube with a pristine substrate, identical to that supporting the nanostructures, inserted into the optical path.

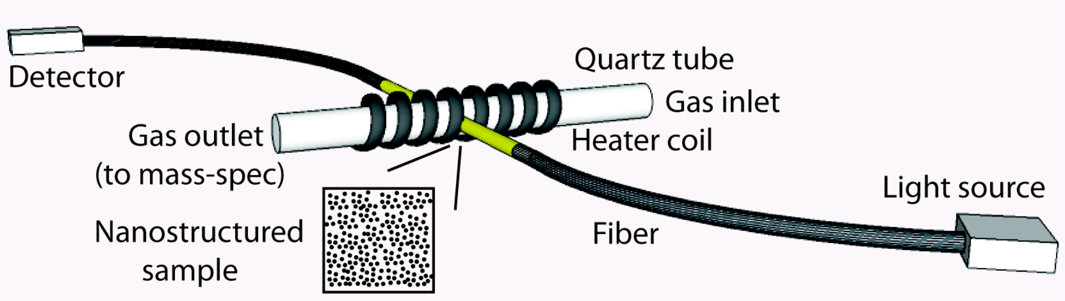

Figure 6.2 Quartz tube gas-flow reactor with online optical spectroscopy.

For the optical characterization with the fiber spectrometer, a white light source is used to irradiate the sample. After passing through the nanostructured sample, the different wavelengths of the transmitted light are dispersed onto separate pixels on an array detector. Any change in intensity, as compared to the reference measurement reflects the extinction caused by the nanostructures. Extinction is, by definition, the sum of light absorption (A) and scattering (S). From a single measurement, it is not possible to separate the two contributions to the measured extinction. However, extinction measurements of nanostructures exhibit similar spectral characteristics as the absorption spectrum and can therefore conveniently be used to characterize the supported nanostructures during oxidation conditions.

6.2.2 Off-line optical extinction spectroscopy

Similar measurements have been performed ex situ, in a commercial system (Varian, Cary 500). This system covers a broader spectral range (2500-200 nm) and in contrast to the fiber spectrometer setup, spectral resolution is achieved using a grating to spectrally separate the irradiating white light. Therefore, the sample is irradiated with monochromatic light in this kind of spectrophotometer. As with the fiber spectrometer described above, reference measurements of bare samples are taken and extinction data can be extracted.

For the case where the nanostructures are supported on non-transparent substrates, as is the case for all samples etched out of bulk carbon, extinction measurements using the transmission geometry is not feasible since even quite thin carbon films completely absorb light in the wavelength interval of interest. Therefore, these samples have been characterized in reflectance mode. The basic working principle is the same as in the transmission mode but instead of detecting the transmitted beam all reflected light is collected. This can be done using an integrating sphere detector. The detector consists of a spherical cavity, whose inside surface is coated with a highly reflective, non-absorbing material. The sample is positioned at the exit slit and any light reflected (back scattered) from the surface will be redirected into the sphere where it scatters from the reflecting walls and onto a detector positioned inside the sphere. The integrating sphere detector can also be operated with the sample positioned at the entrance aperture in order to measure the magnitude of light scattered in the forward direction. Reference measurements are taken from a surface covered with the same high reflecting material as the inner wall of the sphere and from flat carbon surfaces without nanostructures.

6.2.3 Raman spectroscopy

Raman scattering is the inelastic scattering of a photon by a molecule or solid through exchange of rotational or vibrational energy. While the majority of photons are scattered elastically (Rayleigh scattering), i.e. without change of frequency, a fraction of them will generate or annihilate a rotational and/or vibrational quanta. The former case is termed Stokes scattering and the latter anti-Stokes (fig.6.3). By analyzing the shift in photon frequency, and the relative intensities of the scattering events, information about the transition energies between the involved states and the population of these can be deduced. Relative intensities of the anti-Stokes and corresponding Stokes lines carry information about the temperature of the sample, since anti-Stokes lines derive from excited states, which are populated to a larger extent at high temperatures.

The systems used in this work are commercially available Raman spectrometers consisting of a laser light source and a microscope through which the samples are irradiated. The microscope is also used to collect the light to a detector, equipped with a grating, for analysis of the spectral distribution of the Raman scattered light.

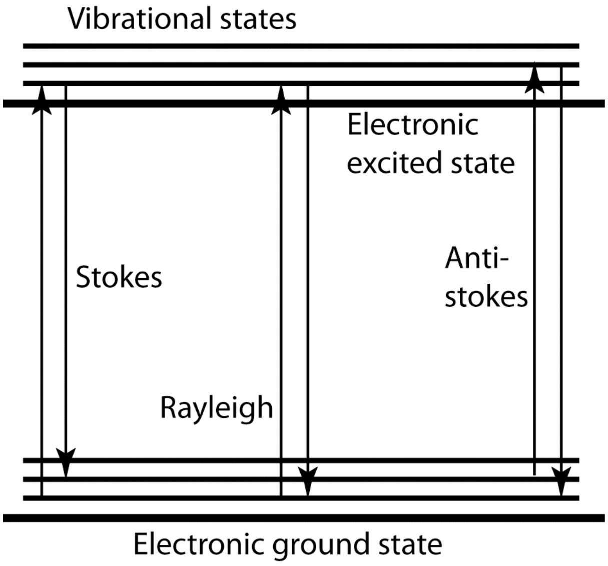

Figure 6.3 Schematic description of resonant Raman scattering.

Raman scattering cross sections are in general small (less than 1% of the scattered light) and observation of the process requires irradiation with relatively intense laser light. However, the cross sections are dramatically enhanced if the laser light matches a resonance in the irradiated system. It can be either an electronic transition in a Raman scattering molecule or solid (resonant Raman scattering, fig.6.3) or an optical resonance in the support, onto which the scattering molecule is adsorbed (surface enhanced Raman scattering (SERS). In the former case, the enhancement is a result of the increased cross section for light scattering for real- as compared to virtual- transitions. In the latter case, SERS is observed for molecules adsorbed onto any surface sustaining optical resonances, but is strongest for rough metal surfaces[136]. In this case, the reason for the enhanced scattering cross section is a combination of electro-magnetic field enhancement and chemical enhancement[156]. The electromagnetic field impinging on a metallic surface can, under specific conditions, excite the electrons collectively, an excitation termed surface plasmon. If the frequency of the exciting light is matched to the plasmon resonance, molecules adsorbed on the metal surface experience a significantly stronger field than they would in the gas phase thus significantly increasing the probability of a scattering event. The other, much weaker, chemical enhancement mechanism is due to creation of electronic states upon adsorption. If these states facilitate resonant electronic excitations this induces an increased probability for Raman scattering. SERS is frequently used to characterize vibrational states in adsorbed molecules.

7 Results and discussion

This chapter provides a compact summary of all the work presented in this thesis. It consists of an overview, which elucidates the "red thread" of the work and describes the relation between the different parts of the work, followed by a short summary of the content of the appended papers. Finally it contains a discussion of the achieved results and an inventory of possible interesting extensions and further applications of this work. Since the previous chapters are based on relevant literature studies as well as the results presented in the appended papers, this chapter will, by necessity, repeat some of the observations and discussions already presented.

Paper I, describes the development of, and possibilities with, the nanolithographic technique, hole-mask colloidal lithography (HCL) that is used throughout the work presented in the subsequent papers. Paper II demonstrates how this fabrication technique can be applied to fabricate nanostructures out of bulk carbon materials and that these nanostructures exhibit optical properties, which depend on their size. In Paper III, these optical properties are investigated in detail, both experimentally and theoretically and the correlation between nanostructure size and optical absorption is further established. Paper IV, then uses Raman spectroscopy to investigate the vibrational properties of the nanostructured samples. The previously observed enhancement of optical absorption, induced by the nanostructures, is exploited in the Raman studies. In addition to a slight enhancement of the Raman scattered light intensity, substantial heating of the nanostructures is observed, as an effect of the applied laser irradiation. The subsequent manuscript, Paper V, exploits the knowledge collected during the work with all the four previous papers. HCL is further developed and utilized to prepare amorphous carbon nanostructures on fused quartz. The optical properties of these nanostructures are then investigated and a correlation between these and the structure size is established. This correlation is then used to monitor the oxidation of the carbon nanostructures in-situ, providing an excellent approach to investigate the combustion of carbon nanostructures, with relevance for many practical applications.

7.1 Summary of papers

7.1.1 Paper I. Hole-mask colloidal lithography

This first paper presents a detailed description of the development of a novel nanolithography technique, demonstrations of its usefulness for fabrication in general and in two practical applications. The detailed fabrication scheme presented is thoroughly described and discussed in Chapter 3, Hole-mask colloidal lithography, and will not be repeated here. Briefly, self-assembley of colloidal spheres and oxygen reactive ion etching (RIE) is utilized to prepare double layer polymer/metal masks. These can then be used for nanostructure fabrication, either as etch- or evaporation masks or both. Using the same fundamental fabrication procedure, nanostructures in most materials and with a variety of different shapes can be fabricated. The distribution and size of these nanostructures are controlled by the self-assembly and RIE processes, while shapes are controlled by the different evaporation steps. In the publication, different types of nanostructures that can be produced are realized, experimentally (fig.7.1).

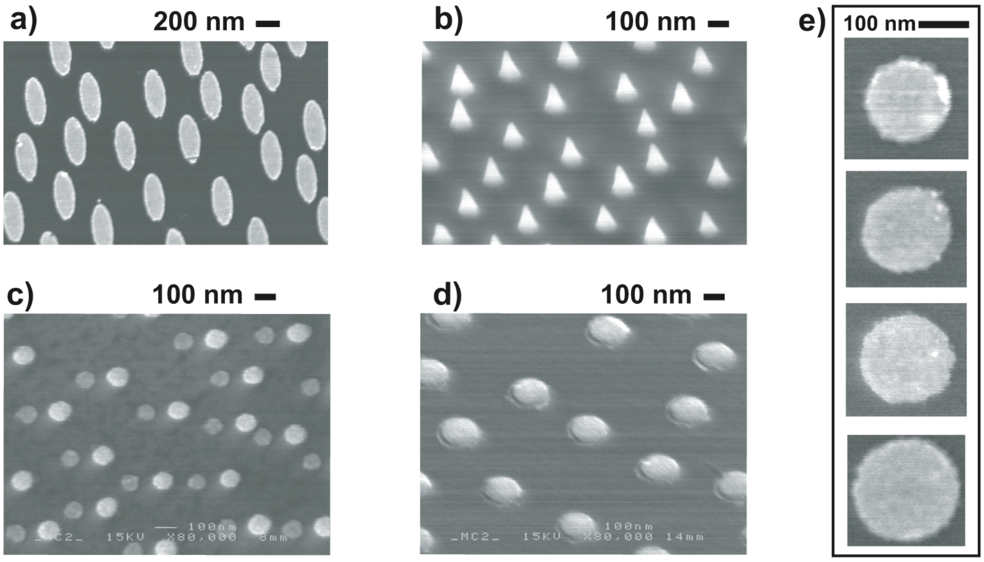

Figure 7.1 Examples on experimentally demonstrated fabrication of nanostructures using HCL: a) Elliptical and b) conical Au nanostructures. c) Pairs of Au and Ag structures and d) Au discs embedded in a TiO_2 film. e) Precise control over nanostructure diameter, achieved through etching of the supporting polymer film.

Furthermore, the paper illustrates the applicability of the developed nanofabrication technique with two practical examples. The first application takes advantage of the opportunity to design nanostructures with sharp edges and well-defined size. Ag nanocones in close packed and well-separated patterns are produced. These samples are then used as substrates in surface enhanced Raman spectroscopy (SERS) measurements. To get a substantial enhancement of the Raman scattered light, the size of the fabricated nanocones is chosen so that the localized surface plasmon resonance (LSPR) matches the wavelength of the laser used in the SERS-experiments. Fig.7.2.a shows that a significant enhancement is achieved, both from the nanocone array and from single structures.

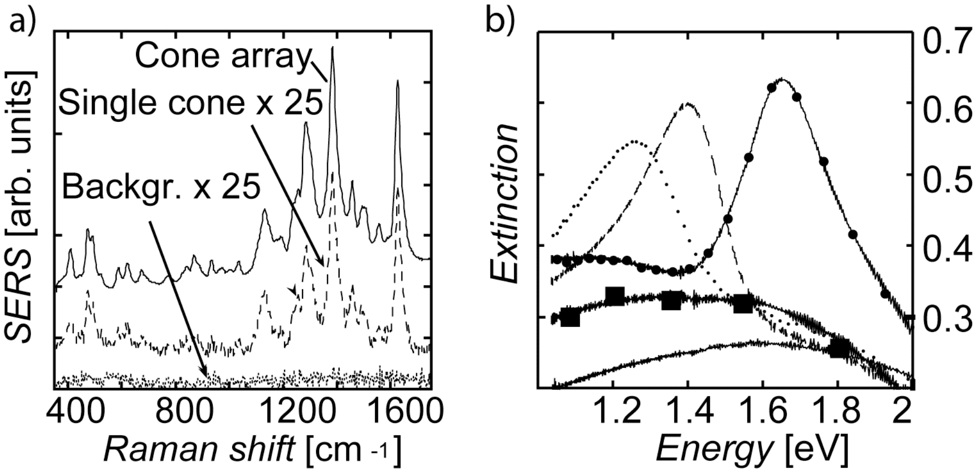

Figure 7.2 a) SERS spectra (average of five individual measurements) of benzotriazole dye adsorbed on close packed arrays as well as on well-separated single Ag nanocones. The background signal was measured from a spot in between the well-separated structures.
b) Optical extinction spectra from an array of Au nanodiscs supported on a TiO_2 film (solid circles), gold nanodiscs embedded in nanoholes (dashed) and same with SiO_2 capping layer (dotted). The spectra from TiO_2 film patterned with nanoholes (diameter 110 nm, solid line) and a flat unpatterned TiO_2 film (squares) are shown for comparison.

The other application demonstrates the advantage of having a mask suitable for both etch and evaporation processes. A polymer/Cr hole-mask is prepared on top of a thin TiO_2-film. An initial CF_4 etch-process is first applied to achieve cylindrical indentations in the TiO_2 film. Subsequent evaporation of Au, or Au and SiO_2, results in the deposition of discs at the bottom of the indentations. The optical properties of these nanostructured TiO_2-films are investigated using spectrophotometry and it is found that the LSPR of the Au discs significantly influences the optical extinction of the samples (fig.7.2.b).

7.1.2 Paper II. Patterning of highly oriented pyrolytic graphite and glassy carbon surfaces by nanolithography and oxygen plasma etching.

In Paper II, HCL is used to fabricate Au nanodiscs on two types of carbon surfaces, highly oriented pyrolytic graphite, (HOPG) and glassy carbon (GC). The nanodiscs are used as etch masks in an oxygen RIE process, where the oxygen plasma effectively removes carbon from the part of the surfaces that are not protected by the gold discs. In this way, nanopillars are etched out of the carbon surfaces (fig.7.3). It is also shown that the same HCL-technique can equally well be used to etch out pits in a HOPG surface. Significant differences are observed for the nanostructures etched out of the two different materials. From the sizes achieved by the nanostructures, the response to oxygen plasma of the two materials is determined, showing that GC is etched faster than HOPG, both in the direction parallel and perpendicular to the surface. Based on these differences, the oxidation mechanisms for the two materials are discussed.

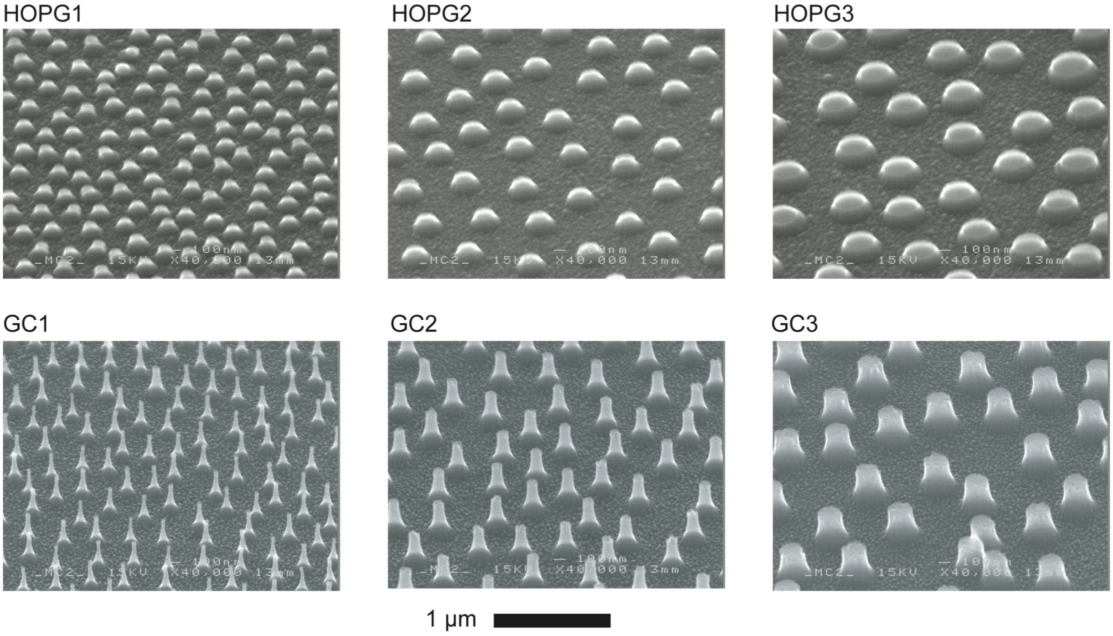

Figure 7.3 SEM images of HOPG (top row) and GC (bottom row) nanostructures fabricated with three different etch mask dimensions. Each pair of nanostructured samples (vertically) was fabricated with identical process conditions.

Furthermore, this paper crudely demonstrates that the carbon nanostructures can be transferred to another surfaces by pressing the nanostructured surface against a Si wafer. Some of the nanostructures then sticks to the Si surface and it is observed that the nanostructures have the same, layered micro structure as the original graphite sample. An initial investigation of the optical properties of the fabricated HOPG nanostructures is also undertaken. This study shows that the reflectivity of the surfaces decrease as the height of the nanostructures grows and hence establishes a relation between nanostructure size and optical properties.

7.1.3 Paper III. Resonant optical absorption in graphite nanostructures

In this paper, the optical properties of HOPG nanostructures are studied in detail. Nanostructures with different sizes are fabricated using the technique described in the previous publications and the optical properties are investigated using spectrophotometry. In addition to the experimental investigations, calculations are performed using the finite difference time domain (FDTD) method.

Both the experimental and theoretical results obtained reveal resonant optical absorption, correlating with the nanostructure sizes. The amplitude and spectral position of the optical resonances depend on the heights and diameters of the nanostructures and the same trends are observed, in both measurements and calculations (fig.7.4, a-d). Furthermore, the origin of the observed optical resonances and the size dependent trends are discussed in the context of Mie-theory and geometrical resonances. In addition, observed similarities and differences between theory and experiments are quantified and compared and possible reasons for the observed differences are elucidated.

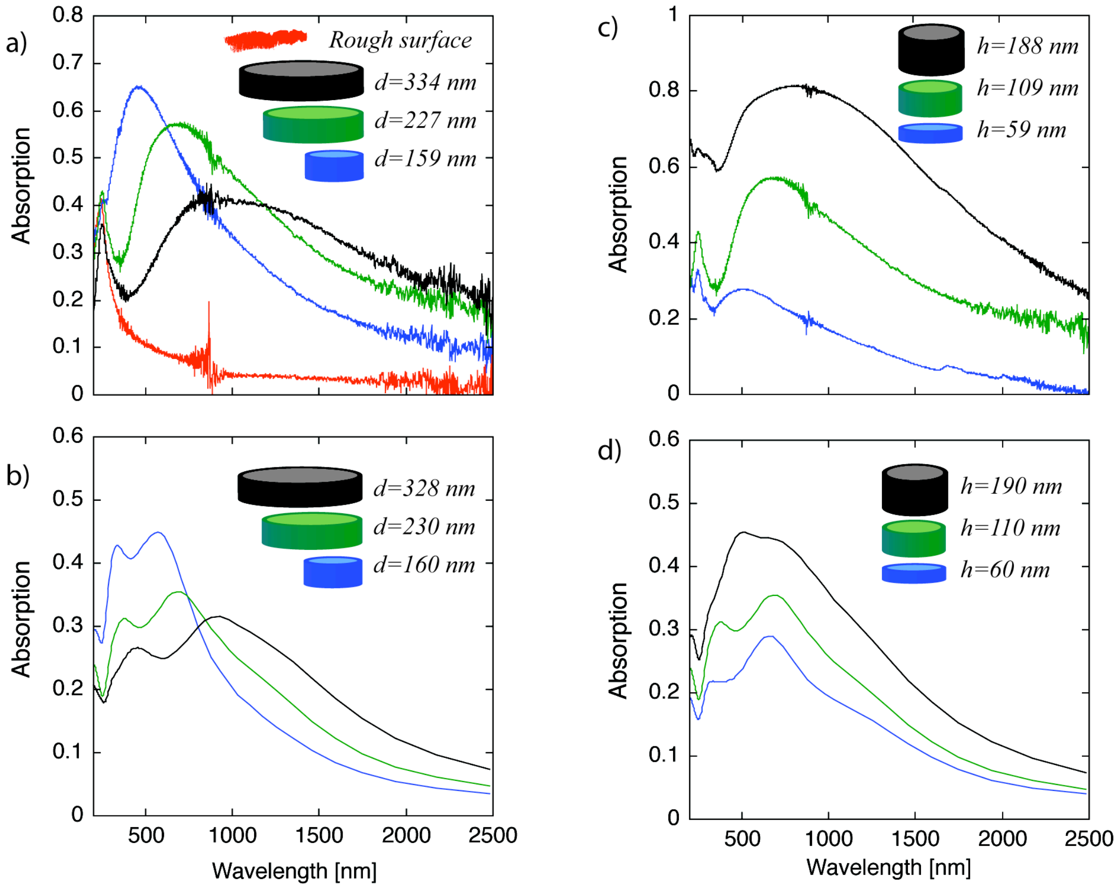

Figure 7.4 Optical absorption of HOPG nanostructures with constant height and various diameters a) experiment and b) calculations. Corresponding data for nanostructures with constant diameter and various heights for c) experimental data and d) calculations.

7.1.4 Paper IV. Raman spectroscopy of nanostructured graphite

The by now well-established procedure for fabrication of HOPG nanostructures on HOPG surfaces is used to prepare similar nanostructures as those already investigated in Paper II & III. This study continues the exploration of the physical and optical properties of the graphite nanostructures. Raman spectroscopy is used for the investigation of the mechanical and thermal properties of the samples.

The observation of sharp Raman peaks at 1580 (G-peak) and 1350 cm^{-1} (D-peak) confirms that the graphitic character of the samples is maintained during the nanofabrication process, but also that a significant disordering of the surfaces in between the nanostructures is introduced. These observations are in accordance with observations from scanning electron microscope (SEM) and atomic force microscope (AFM) measurements.

Comparing nanostructured samples with pristine HOPG, it is clear that the intensity of the Raman scattered light is different for the different samples. It is demonstrated that the nanostructures exhibiting the strongest optical absorption, at the wavelength of the irradiating laser, also exhibit the strongest Raman scattering signals (fig.7.5.a). Furthermore, for increasing laser power density, the Raman peaks are observed to shift. The G-peak of the nanostructured samples splits up into two convoluted components, whereas the other peaks maintain their original shape. Observed peak shifts for different peaks naturally divide into two categories, with two different magnitudes of the shifts (fig.7.5.b). These peak shifts are attributed to laser induced heating of the nanostructured samples, where higher temperatures induces larger shifts. The two different magnitudes of the shifts are suggested to derive from different temperatures in the selectively heated nanostructures and in the supporting substrate.

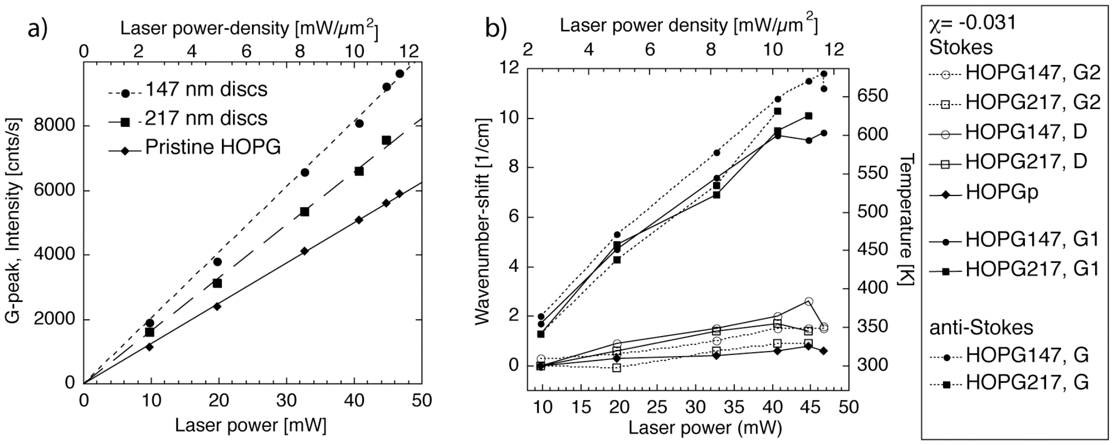

Figure 7.5 a) Intensity of the main Raman peak for two nanostructured HOPG samples and one pristine reference, for different intensities of the irradiating laser light. b) Shifts of peak positions corresponding to different Raman modes in the nanostructured HOPG and the reference samples. The main peak is split into two convoluted peaks, G1 & G2, which shifts differently with increasing laser power.

7.1.5 *Paper V. Oxidation of lithographically prepared amorphous carbon soot-models, monitored by optical spectroscopy*

The fifth paper exploits the techniques and knowledge obtained in all of the previous studies. HCL is adapted and utilized for the fabrication of amorphous carbon nanostructures, supported on fused quartz. Cr is used as an alternative to the commonly applied polymer sacrificial layer with the benefit of better temperature and UV-resistance of the evaporation masks. Six identical samples with carbon nanostructures, intended as model samples for the study of soot oxidation, are prepared by evaporation of amorphous carbon through the masks.

In similarity with the results in Paper III, amorphous carbon nanostructures are also shown to support optical resonances. Spectrophotometer measurements reveal a strong correlation between nanostructure size on one hand and position and intensity of the extinction peaks on the other hand. Oxidation in molecular oxygen at elevated temperatures is used to shrink the nanostructures, and intermediate measurements of the optical extinction spectra and nanostructure sizes are conducted. From these measurements, an empirical relation between nanostructure size and optical properties is established. The nanostructure volumes are observed to vary linearly with both intensity and position of the extinction peak.

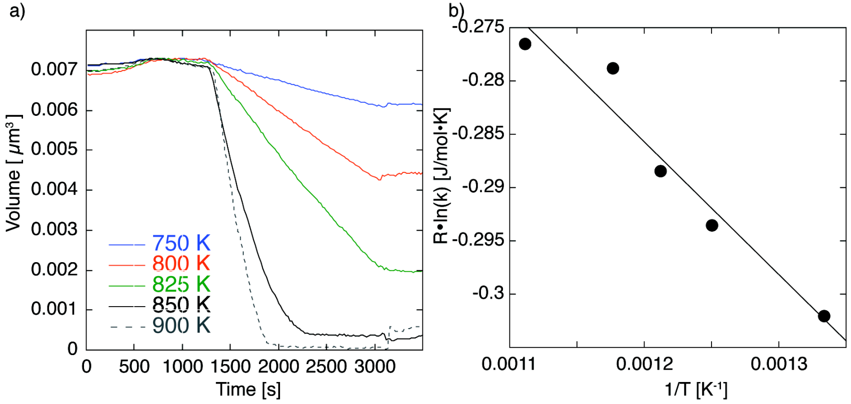

Figure 7.6 a) Volume decrease of lithographically prepared amorphous carbon nanostructures determined from optical extinction measurements. b) Arrhenius plot of the temperature dependent reaction rates. An activation energy for combustion of the nanostructures of 124 kJ/mol was determined.

A quartz tube gas-flow reactor is used for the oxidation of the nanostructures. Since this reactor is transparent in the wavelength interval where the carbon nanostructures exhibit optical resonances, these can be monitored in-situ. With the relation between extinction amplitude and nanostructure volume established, the combustions of carbon nanostructures is followed at five different temperatures (fig.7.6.a). The oxidation rates are calculated from the optically determined volume change and increasing reaction rates with increasing temperature is observed as expected. From the temperature dependent reaction rates, an Arrhenius plot is constructed (fig.7.6.b) and the activation energy for combustion of the amorphous carbon nanostructures is determined to be124 kJ/mol.

7.2 Discussion

There are several aspects of HCL, which makes it practicable in different situations. Two of the main advantages are the speed and simplicity of the technique. With relatively simple equipment, it can be used to nanofabricate large area samples. Therefore it is useful, both for experiments where large samples are may be required to yield measurable results and for fabrication of commercial products. Another of the advantages is that it facilitates fabrication of nanostructures with geometries that are difficult to achieve with other fabrication techniques. Pairs of discs with very small gaps between the individual particles and inverted ring structures are two such examples. Other interesting nanofeatures that can easily be prepared are cones and ellipses with very sharp edges. A final advantage to be mentioned is that the evaporation masks can be made entirely in metal or other materials that are durable to high temperatures. This can be useful for applications where the nanostructures are defined under very hostile conditions. Evaporation of materials often generates high temperatures and intense UV-irradiation, which can damage masks made from polymeric materials. Furthermore, many etch processes used to define nanopatterns, generate heat and/or chemical cross-linking of polymers, which further emphasizes the usefulness of non-polymeric masks.

The systematic nanofabrication approach to investigate the physical properties of carbon nanostructures has proven to be a good example of the usefulness of HCL. From the investigations of well-defined carbon nanostructures much useful information has been retrieved. The optical properties and their correlation with structure size is one of the central pieces of information gained in this work. Relying on the optical properties, Raman spectroscopy could be used to investigate the atomic arrangement and thermal properties of the nanostructures. Again, the systematic approach with nanofabrication of structures with well-defined size and separation proved useful to relate nanostructure properties to the structure geometries. Furthermore, using the same fabrication approach for different carbon materials has contributed to knowledge about the oxidation of carbon and how nanostructures decrease in size during combustion. Putting all these pieces together, it was possible to develop a versatile and useful new approach for deeper studies of combustion of carbon nanostructures. In conclusion, the bottom line of all the work presented in this thesis is the systematic approach, using nanofabrication to yield samples with well-defined properties and associated analytical work.

In addition to the applications demonstrating fabrication of carbon nanostructures, the HCL technique has been proven useful in a number of other applications. Examples of such applications are studies where HCL has been used to fabricate nanostructures for the study of optical, magnetic and chemical properties[24-30, 55-57]. Complementary to the already demonstrated uses of the technique, further studies are in progress. However, several of the more unusual nanostructures that can be fabricated still remain un-exploited.

7.3 Outlook

The preparation of elliptical nanostructures is an example of demonstrated applications where HCL has proven useful. Patterning large areas with asymmetric nanostructures is interesting both for fabrication of nanostructures in magnetic materials and for optical studies. An elliptical particle shape, with a common orientation of the individual structures, offers an opportunity to select different optical properties by using a polarized electromagnetic field when irradiating the nanostructures. By simply rotating the polarization direction (or the sample) different optical responses are achieved while all other conditions are kept constant[25, 157].

Other interesting nanostructures that have been demonstrated, but not yet fully exploited, are the nanocones. Both metallic nanocones and the sharp features in glassy carbon could be interesting in practical applications. Sharp edges are in general associated with concentration of electric and magnetic fields. Properly optimized nanocones could therefore be interesting as field emitters and for enhancement of optical spectroscopies such as SERS. Along the same line of reasoning, the fabrication procedure demonstrated in Paper II, for the fabrication of HOPG and GC pillars could potentially be useful for fabrication of probes for AFM measurements, although some other technique than HCL would have to be used to define the nanodisc etch mask. However, the fabricated GC-pillars possess many of the properties desirable for tips; mechanical strength, chemical inertness and sharpness.

Another, yet largely unexplored possibility with the HCL technique is the fabrication of multiple structures from each hole in the mask. Single and bi-metallic pairs have already been demonstrated, but this fabrication could easily be extended to include fabrication of chains of particles or to place nanostructures in the small gap between adjacent discs in a pair. The prospect of precisely controlling the gap size and the relative orientation of the nanostructures may find interest in sensing applications as well as in light harvesting and photocatalysis.

Concerning the carbon nanostructures, several interesting opportunities are currently being considered. The successful transfer of graphite nanostructures from the HOPG sample to a Si-wafer demonstrates that this approach can be used to fabricate single crystal carbon nanostructures on many surfaces. With some refinement of the transfer process, this could be used to prepare valuable samples for the study of the mechanisms of carbon oxidation. A graphite nanostructure supported on an inert substrate would provide a nanocarbon model where the number of edge sites could be very precisely estimated. Using the optical resonances of the nanostructures, the oxidation of a single well-defined structure could be followed, thus eliminating many of the uncertainties related with macroscopic samples and measurements. Furthermore, decreasing the thickness of the nanostructures, before or after transfer to another surface, offers a route towards preparation of large arrays of graphene structures.

From the Raman study, it is suggested that carbon nanostructures can be brought to high temperatures during irradiation, while the surrounding material remains at a much lower temperature. At the same time, the microstructure of the carbon nanostructures is constantly monitored. Therefore, applying intense laser irradiation to an amorphous carbon nanostructures in an inert environment could probably induce structural changes to the carbon, without damaging the surrounding material. This may be another route towards the fabrication of graphite nanostructures on, e.g., transparent supports.

The investigation of oxidation of amorphous carbon nanostructures provides a good start for further systematic studies of soot oxidation. Experiments similar to those already undertaken can easily be performed to investigate the influence of different gas compositions, catalysts or temperatures. The applied nanofabrication method can easily be used to prepare nanostructures in carbon materials with properties closer to real soot. Since the evaporation masks can endure high temperatures and hostile chemical environments, thin soot films could be deposited instead of the amorphous carbon films and the same approach as already demonstrated applied to investigate the oxidation process. This would represent a very well controlled experiment, yet with a model with properties resembling real soot. The weakness of the current experimental setup used in the oxidation experiments is probably the temperature measurements.

A final, more technical comment, on the HCL technique concerns the system used for deposition of materials. Since the conditions during deposition of both the mask and the structure materials can be used to vary the geometries and positions of the fabricated nanostructures, the evaporation system is clearly a key instrument in the fabrication process. A more flexible sample holder, than the ones used hitherto, would facilitate fabrication of many structures that have not yet been realized. For example, if the azimuth and polar angles (with the evaporation source and the sample on the z-axis and the angles measured between the sample surface normal and the z-axis) could both be varied arbitrarily, each hole in the mask could be used to deposit small arrays of nanostructures, in any desired pattern. For example linear chains in one or more directions, with the nanostructures in one and the same or different materials could be fabricated. Furthermore, by continuously changing the angle of the sample holder during the evaporation, each single hole could be used to draw the nanostructure of choice. An example is a geometry where the sample is held at a small constant polar angle, while the azimuth is continuously changed, which would result in concentric rings with the diameter determined by the applied constant angle.

8 Acknowledgements

Finally, there are a number of persons, without whom this thesis would not have been:

First and foremost, I would like to express my sincere gratitude to Professor Bengt Kasemo for all; support, encouragement, contagious enthusiasm, prompt feedback, financing the PhD-position and for creating a casual and informal environment to work in.

I am also sincerely grateful to my supervisor, Professor Dinko Chakarov. Thanks for all help with practical and theoretical work, for pushing me in tough times, and for enthusiastically encouraging me to pursue new ideas and results. Thanks also for the pleasant, casual evenings in the "library" in Lindome.

It may or may not have been a good idea to decide to finish the work with writing this thesis in the midst of the short and precious Swedish summer. On one hand, I have been left alone but on another hand, I have been left to myself. However, in spite of vacation times, I have had no problems at all to get feedback and support from both of you, Bengt and Dinko. For you, sacrificing precious summer/vacation time on this, I am extra grateful.

I would also like to thank all co-authors of the papers (all Dr. or Prof.):

Christoph, for being an excellent Swedified, Swiss office mate, suchi and fondüe chef and for pushing the writing of the HCL-paper at an early stage.

Sasha, for the hard work with finishing the HCL paper, for continuously exploring and discussing new applications of the technique and for saving us all from Christmas at Liseberg.

Michael Z., for always taking time to discuss difficult questions and for always coming up with good advice.

Yury, for Raman discussions and good companionship in the Austrian ski-slopes.

Duncan, for creating the foundation for much of the work I have done and for teaching me all there is to know about Colloidal lithography.

Tavakol, for all patient explanations from the theoretical side and for invaluable input to the nanocarbon-optics paper.

Mikael K., for many rewarding discussions about optics and Raman spectroscopy

Juan, for the extensive and enthusiastic work with Raman characterization of my little carbon pancake stacks.

Enough with co-authors, thanks also to:

Ann G and Marie G for gently, but firmly, leading me in on the scientific path.

Björn, for all the surdegs parties and interesting discussions concerning work, music, potatoes, beer etc.

Malin, for encouragement in general and for spreading an early-morning good mood.

Elisabeth B, for keeping me fit, chasing those shuttlecocks and showing me how the French do the frog dance.

Carl, for valuable discussion about everything from nanoparticle optics to music and for good company on high altitude picknicks.

Thanks also to all former and present members of the Chemical and Biological physics groups, for creating a good atmosphere to work in.

Jag vill också säga, stort tack till mor och far! Er uppmuntran och kärleksfulla omsorg har betytt mer än ni tror. Tack för att ni alltid har stått bakom mig, oavesett vad jag valt att hitta på.

Tack också till resten av familjen, för stöd, nyfikenhet och hjälp.

Sist men absolut inte minst, tack till alla fantastiska vänner, för att ni gör livet så festligt att leva.

This work was performed within the Photonano project, financially supported by SSF (Swedish foundation for strategic research, grant number 2001:0321/53)

.

9 References

[1] Kostoff RN, Murday JS, Lau CGY, Tolles WM. The seminal literature of nanotechnology research. Journal of Nanoparticle Research. 2006;8(2):193-213.
[2] Min YJ, Akbulut M, Kristiansen K, Golan Y, Israelachvili J. The role of interparticle and external forces in nanoparticle assembly. Nat Mater. 2008;7(7):527-38.
[3] Rutherglen C, Burke P. Nanoelectromagnetics: Circuit and Electromagnetic Properties of Carbon Nanotubes. Small. 2009;5(8):884-906.
[4] Zecchina A, Groppo E, Bordiga S. Selective catalysis and nanoscience: An inseperable pair. Chemistry-a European Journal. 2007;13(9):2440-60.
[5] Zach M, Hagglund C, Chakarov D, Kasemo B. Nanoscience and nanotechnology for advanced energy systems. Current Opinion in Solid State & Materials Science. 2006;10(3-4):132-43.
[6] Forster P, Ramaswamy V, Artaxo P, Berntsen T, Betts R, Fahey DW, et al. Changes in Atmospheric Constituents and in Radiative Forcing. In: Solomon S, Qin D, Manning M, Chen Z, Marquis M, Averyt KB, et al., eds. *Climate Change 2007: The Physical Science Basis Contribution of Working Group I to the Fourth Assessment Report of the Intergovernmental Panel on Climate Change*. Cambridge: Cambridge University Press 2007:131-217.
[7] Grabinski C, Hussain S, Lafdi K, Braydich-Stolle L, Schlager J. Effect of particle dimension on biocompatibility of carbon nanomaterials. Carbon. 2007;45(14):2828-35.
[8] Duffin R, Mills NL, Donaldson K. Nanoparticles - A thoracic toxicology perspective. Yonsei Med J. 2007;48(4):561-72.
[9] Hu YH, Shenderova OA, Hu Z, Padgett CW, Brenner DW. Carbon nanostructures for advanced composites. Rep Prog Phys. 2006;69(6):1847-95.
[10] Choi MJ, McDonagh AM, Maynard P, Roux C. Metal-containing nanoparticles and nano-structured particles in fingermark detection. Forensic SciInt. 2008;179(2-3):87-97.
[11] Salata OV. Applications of nanoparticles in biology and medicine. J Nanobiotech. 2004;2(3):1-6.
[12] Pierson HO. Handbook of Carbon, Graphite, Diamond and Fullerenes. 1 ed. New Jersey: Noyes Publications 1993.
[13] Kroto HW, Heath JR, Obrien SC, Curl RF, Smalley RE. C-60 - BUCKMINSTERFULLERENE. Nature. 1985;318(6042):162-3.
[14] Iijima S. Helical microtubules of graphitic carbon. Nature. 1991;354(6348):56-8.

[15] Chen ZH, Appenzeller J, Lin YM, Sippel-Oakley J, Rinzler AG, Tang JY, et al. An integrated logic circuit assembled on a single carbon nanotube. Science. 2006;311(5768):1735.
[16] Yang ZP, Ci LJ, Bur JA, Lin SY, Ajayan PM. Experimental observation of an extremely dark material made by a low-density nanotube array. Nano Lett. 2008;8(2):446-51.
[17] Highwood EJ, Kinnersley RP. When smoke gets in our eyes: The multiple impacts of atmospheric black carbon on climate, air quality and health. Environ Int. 2006;32(4):560-6.
[18] van Setten B, Makkee M, Moulijn JA. Science and technology of catalytic diesel particulate filters. Catal Rev-Sci Eng. 2001;43(4):489-564.
[19] Bond TC, Bergstrom RW. Light absorption by carbonaceous particles: An investigative review. Aerosol Sci Technol. 2006;40(1):27-67.
[20] Schnaiter M, Horvath H, Mohler O, Naumann KH, Saathoff H, Schock OW. UV-VIS-NIR spectral optical properties of soot and soot-containing aerosols. J Aerosol Sci. 2003;34(10):1421-44.
[21] Krecl P, Strom J, Johansson C. Carbon content of atmospheric aerosols in a residential area during the wood combustion season in Sweden. Atmos Environ. 2007;41(33):6974-85.
[22] Quinten M, Kreibig U, Henning T, Mutschke H. Wavelength-dependent optical extinction of carbonaceous particles in atmospheric aerosols and interstellar dust. Appl Optics. 2002;41(33):7102-13.
[23] Iati MA, Saija R, Giusto A, Denti P, Borghese F, Cecchi-Pestellini C. Optical properties of interstellar grain aggregates. J Quant Spectrosc Radiat Transf. 2004;89(1-4):43-51.
[24] Esteban R, Vogelgesang R, Dorfmuller J, Dmitriev A, Rockstuhl C, Etrich C, et al. Direct Near-Field Optical Imaging of Higher Order Plasmonic Resonances. Nano Lett. 2008;8(10):3155-9.
[25] Dmitriev A, Hagglund C, Chen S, Fredriksson H, Pakizeh T, Kall M, et al. Enhanced Nanoplasmonic Optical Sensors with Reduced Substrate Effect. Nano Lett. 2008;8(11):3893-8.
[26] Langhammer C, Yuan Z, Zoric I, Kasemo B. Plasmonic properties of supported Pt and Pd nanostructures. Nano Lett. 2006;6(4):833-8.
[27] Pakizeh T, Dmitriev A, Abrishamian MS, Granpayeh N, Kall M. Structural asymmetry and induced optical magnetism in plasmonic nanosandwiches. J Opt Soc Am B-Opt Phys. 2008;25(4):659-67.
[28] Pakizeh T, Langhammer C, Zoric I, Apell P, Käll M. Intrinsic fano interferences of localized plasmons in Pd nanoparticles. Nano Lett. 2009;9(2):882-6.
[29] Seidel YE, Muller M, Jusys Z, Wickman B, Hanarp P, Kasemo B, et al. Nanostructured, glassy-carbon-supported Pt/GC electrodes: The presence of secondary pt nanostructures and how to avoid them. J Electrochem Soc. 2008;155(10):K171-K9.
[30] Seidel YE, Schneider A, Jusys Z, Wickman B, Kasemo B, Behm RJ. Mesoscopic mass transport effects in electrocatalytic processes. Faraday Discussions. 2009;140:167-84.
[31] Bhushan B. Springer Handbook of Nanotechnology Berlin, Heidelberg, New York: Springer-Verlag 2004.

[32] Poole Jr CP, Owens FJ. Introduction to Nanotechnology: John Wiley & Sons, Inc 2003.
[33] Marrian CRK, Tennant DM. Nanofabrication. J Vac Sci Technol A. 2003;21(5):S207-S15.
[34] Gates BD, Xu QB, Stewart M, Ryan D, Willson CG, Whitesides GM. New approaches to nanofabrication: Molding, printing, and other techniques. Chem Rev. 2005;105(4):1171-96.
[35] Chen Y, Pepin A. Nanofabrication: Conventional and nonconventional methods. Electrophoresis. 2001;22(2):187-207.
[36] Tseng AA, Notargiacomo A, Chen TP. Nanofabrication by scanning probe microscope lithography: A review. J Vac Sci Technol B. 2005;23(3):877-94.
[37] Solak HH. Nanolithography with coherent extreme ultraviolet light. J Phys D-Appl Phys. 2006;39(10):R171-R88.
[38] Yang SM, Jang SG, Choi DG, Kim S, Yu HK. Nanomachining by colloidal lithography. Small. 2006;2(4):458-75.
[39] Black CT, Ruiz R, Breyta G, Cheng JY, Colburn ME, Guarini KW, et al. Polymer self assembly in semiconductor microelectronics. IBM J Res Dev. 2007;51(5):605-33.
[40] Zhang G, Wang DY. Colloidal Lithography-The Art of Nanochemical Patterning. Chem-Asian J. 2009;4(2):236-45.
[41] Hanarp P, Sutherland D, Gold J, Kasemo B. Nanostructured model biomaterial surfaces prepared by colloidal lithography. Nanostructured Materials. 1998;12(1-4):429-32.
[42] Lu Y, Liu GL, Kim J, Mejia YX, Lee LP. Nanophotonic crescent moon structures with sharp edge for ultrasensitive biomolecular detection by local electromagnetic field enhancement effect. Nano Lett. 2005;5(1):119-24.
[43] Hulteen JC, Treichel DA, Smith MT, Duval ML, Jensen TR, Van Duyne RP. Nanosphere lithography: Size-tunable silver nanoparticle and surface cluster arrays. J Phys Chem B. 1999;103(19):3854-63.
[44] Haynes CL, McFarland AD, Smith MT, Hulteen JC, Van Duyne RP. Angle-resolved nanosphere lithography: Manipulation of nanoparticle size, shape, and interparticle spacing. J Phys Chem B. 2002;106(8):1898-902.
[45] Deckman HW, Dunsmuir JH. NATURAL LITHOGRAPHY. Appl Phys Let. 1982;41(4):377-9.
[46] Aizpurua J, Hanarp P, Sutherland DS, Kall M, Bryant GW, de Abajo FJG. Optical properties of gold nanorings. Phys Rev Let. 2003;90(5):057401.
[47] Prikulis J, Hanarp P, Olofsson L, Sutherland D, Kall M. Optical spectroscopy of nanometric holes in thin gold films. Nano Lett. 2004;4(6):1003-7.
[48] Hanarp P, Sutherland DS, Gold J, Kasemo B. Control of nanoparticle film structure for colloidal lithography. Colloid Surf A-Physicochem Eng Asp. 2003;214(1-3):23-36.
[49] Wright JP, Worsfold O, Whitehouse C, Himmelhaus M. Ultraflat ternary nanopatterns fabricated using colloidal lithography. Adv Mater. 2006;18(4):421-6.
[50] Bottcher A, Heil M, Sturzl N, Jester SS, Malik S, Perez-Willard F, et al. Nanostructuring the graphite basal plane by focused ion beam patterning and oxygen etching. Nanotechnology. 2006;17(23):5889-94.

[51] Cuesta A, Martinez-Alonso A, Tascon JMD. Carbon reactivity in an oxygen plasma: a comparison with reactivity in molecular oxygen. Carbon. 2001;39(8):1135-46.
[52] Joshi A, Nimmagadda R. EROSION OF DIAMOND FILMS AND GRAPHITE IN OXYGEN PLASMA. J Mater Res. 1991;6(7):1484-90.
[53] Paredes JI, Martinez-Alonso A, Tascon JMD. Comparative study of the air and oxygen plasma oxidation of highly oriented pyrolytic graphite: a scanning tunneling and atomic force microscopy investigation. Carbon. 2000;38(8):1183-97.
[54] You HX, Brown NMD, Alassadi KF, Meenan BJ. SURFACE CHARACTERIZATION OF HIGHLY ORIENTED PYROLYTIC-GRAPHITE MODIFIED BY OXYGEN RADIOFREQUENCY PLASMAS. J Mater Sci Lett. 1993;12(4):201-4.
[55] Langhammer C, Kasemo B, Zoric I. Absorption and scattering of light by Pt, Pd, Ag, and Au nanodisks: Absolute cross sections and branching ratios. J Chem Phys. 2007;126(19):11.
[56] Langhammer C, Schwind M, Kasemo B, Zoric I. Localized surface plasmon resonances in aluminum nanodisks. Nano Lett. 2008;8(5):1461-71.
[57] Langhammer C, Zoric I, Kasemo B. Hydrogen storage in Pd nanodisks characterized with a novel nanoplasmonic sensing scheme. Nano Lett. 2007;7(10):3122-7.
[58] Ahuja R, Auluck S, Wills JM, Alouani M, Johansson B, Eriksson O. Optical properties of graphite from first-principles calculations. Phys Rev B. 1997;55(8):4999-5005.
[59] Chung DDL. Review graphite. J Mater Sci. 2002;37(8):1475-89.
[60] Johnson LG, Dresselh.G. OPTICAL PROPERTIES OF GRAPHITE. Phys Rev B. 1973;7(6):2275-84.
[61] Geim AK, Novoselov KS. The rise of graphene. Nat Mater. 2007;6(3):183-91.
[62] Wettergren K, Kasemo B, Chakarov D. Photodesorption of NO from graphite(0001) surface mediated by silver clusters. Surf Sci. 2004;593(1-3):235-41.
[63] Brown NMD, Cui NY, McKinley A. A study of the topography of a glassy carbon surface following low-power radio-frequency oxygen plasma treatment. Appl Surf Sci. 1998;133(3):157-65.
[64] Brown NMD, You HX. SURFACE-STRUCTURE OF A GLASSY-CARBON - SCANNING TUNNELING MICROSCOPY STUDY. J Mater Chem. 1991;1(3):469-72.
[65] Lei HN, Metrot A, Troyon M. MICROSTRUCTURE STUDY BY SCANNING-TUNNELING-MICROSCOPY OF GLASSY CARBONS HEAT-TREATED AT DIFFERENT TEMPERATURES. J Vac Sci Technol B. 1993;12(3):1827-31.
[66] Rao J, Lawson KJ, Nicholls JR. The characterisation of e-beam evaporated and magnetron sputtered carbon films fabricated for atomic oxygen sensors. Surf Coat Technol. 2005;197(2-3):154-60.
[67] Besold J, Thielsch R, Matz N, Frenzel C, Born R, Mobius A. Surface and bulk properties of electron beam evaporated carbon films. Thin Solid Films. 1997;293(1-2):96-102.
[68] Djurisic AB, Li EH. Optical properties of graphite. J Appl Phys. 1999;85(10):7404-10.
[69] Shyu FL, Lin MF. Plasmons and optical properties of semimetal graphite. J Phys Soc Jpn. 2000;69(12):3781-4.

[70] Jellison GE, Hunn JD, Lee HN. Measurement of optical functions of highly oriented pyrolytic graphite in the visible. Phys Rev B. 2007;76(8):085125.
[71] Greenawa.Dl, Harbeke G, Bassani F, Tosatti E. ANISOTROPY OF OPTICAL CONSTANTS AND BAND STRUCTURE OF GRAPHITE. Physical Review. 1969;178(3):1340-8.
[72] Taft EA, Philipp HR. OPTICAL PROPERTIES OF GRAPHITE. Physical Review. 1965;138(1A):A197-A202.
[73] Marinopoulos AG, Reining L, Rubio A, Olevano V. Ab initio study of the optical absorption and wave-vector-dependent dielectric response of graphite. Phys Rev B. 2004;69(24):245419.
[74] Solanki AK, Kashyap A, Nautiyal T, Auluck S, Khan MA. Band structure and optical properties of graphite. Solid State Commun. 1996;100(9):645-9.
[75] Kuzmenko AB, van Heumen E, Carbone F, van der Marel D. Universal optical conductance of graphite. Phys Rev Let. 2008;100(11):117401.
[76] Saito R, Gruneis A, Samsonidze GG, Dresselhaus G, Dresselhaus MS, Jorio A, et al. Optical absorption of graphite and single-wall carbon nanotubes. Appl Phys A-Mater Sci Process. 2004;78(8):1099-105.
[77] Bohren CF, Huffman DR. Absorption and Scattering of Light by Small Particles. New York: John Wiley & Sons 1998.
[78] Gleeson M, Kasemo B, Chakarov D. Thermal and adsorbate induced plasmon energy shifts in graphite. Surf Sci. 2003;524(1-3):L77-L83.
[79] Williams MW, Arakawa ET. OPTICAL PROPERTIES OF GLASSY CARBON FROM 0 TO 82 EV. J Appl Phys. 1972;43(8):3460-3.
[80] Pajasova L, Soukup L, Jastrabik L, Chvostova D. Optical properties of glassy carbon. 2001 Jul 23-27; Trieste, Italy: World Scientific Publ Co Pte Ltd; 2001. p. 473-7.
[81] Jager C, Mutschke H, Henning T. Optical properties of carbonaceous dust analogues. Astron Astrophys. 1998;332(1):291-9.
[82] Arakawa ET, Williams MW, Inagaki T. OPTICAL-PROPERTIES OF ARC-EVAPORATED CARBON-FILMS BETWEEN 0.6 AND 3.8EV. J Appl Phys. 1977;48(7):3176-7.
[83] Stagg BJ, Charalampopoulos TT. REFRACTIVE-INDEXES OF PYROLYTIC-GRAPHITE, AMORPHOUS-CARBON, AND FLAME SOOT IN THE TEMPERATURE-RANGE 25-DEGREES-C TO 600-DEGREES-C. Combust Flame. 1993;94(4):381-96.
[84] Ferrari AC. Raman spectroscopy of graphene and graphite: Disorder, electron-phonon coupling, doping and nonadiabatic effects. Solid State Commun. 2007;143(1-2):47-57.
[85] Malard LM, Pimenta MA, Dresselhaus G, Dresselhaus MS. Raman spectroscopy in graphene. Phys Rep-Rev Sec Phys Lett. 2009;473(5-6):51-87.
[86] Bonin N, Rao R, Rao AM, Marzari N, Menendez J. Lattice anharmonicity in low-dimensional carbon systems. Phys Status Solidi B-Basic Solid State Phys. 2008;245(10):2149-54.
[87] Thomsen C, Reich S. Doable resonant Raman scattering in graphite. Phys Rev Let. 2000;85(24):5214-7.
[88] Cancado LG, Takai K, Enoki T, Endo M, Kim YA, Mizusaki H, et al. General equation for the determination of the crystallite size La of nanographite by Raman spectroscopy. Appl Phys Let. 2006;88:163106.
[89] Tuinstra F, Koenig JL. RAMAN SPECTRUM OF GRAPHITE. J Chem Phys. 1970;53(3):1126-30.

[90] Kudelski A. Local monitoring of surface chemistry with Raman spectroscopy. JOURNAL OF SOLID STATE ELECTROCHEMISTRY. 2007;13(2):225-30.

[91] Sandler J, Shaffer MSP, Windle AH, Halsall MP, Montes-Moran MA, Cooper CA, et al. Variations in the Raman peak shift as a function of hydrostatic pressure for various carbon nanostructures: A simple geometric effect. Phys Rev B. 2003;67(3):035417.

[92] Everall N, Lumsdon J. FUNDAMENTAL REPRODUCIBILITY OF RAMAN BAND POSITIONS AND STRAIN-MEASUREMENTS OF HIGH-MODULUS CARBON-FIBER - THE EFFECT OF LASER-INDUCED HEATING. J Mater Sci. 1991;26(19):5269-74.

[93] Calizo I, Balandin AA, Bao W, Miao F, Lau CN. Temperature dependence of the Raman spectra of graphene and graphene multilayers. Nano Lett. 2007;7(9):2645-9.

[94] Tan PH, Deng YM, Zhao Q, Cheng WC. The intrinsic temperature effect of the Raman spectra of graphite. Appl Phys Let. 1999;74(13):1818-20.

[95] Everall NJ, Lumsdon J, Christopher DJ. THE EFFECT OF LASER-INDUCED HEATING UPON THE VIBRATIONAL RAMAN-SPECTRA OF GRAPHITES AND CARBON-FIBERS. Carbon. 1991;29(2):133-7.

[96] Atashbar MZ, Singamaneni S. Comparative studies of temperature dependence of G-band peak in single walled carbon nanotube and highly oriented pyrolytic graphite. Appl Phys Let. 2005;86(12):123112.

[97] Nathan MI, Smith JE, Tu KN. RAMAN-SPECTRA OF GLASSY CARBON. J Appl Phys. 1974;45(5):2370.

[98] Soukup L, Gregora I, Jastrabik L, Konakova A. RAMAN-SPECTRA AND ELECTRICAL-CONDUCTIVITY OF GLASSY-CARBON. MATERIALS SCIENCE AND ENGINEERING B-SOLID STATE MATERIALS FOR ADVANCED TECHNOLOGY 1990;11(1-4):355-7.

[99] Ferrari AC, Robertson J. Resonant Raman spectroscopy of disordered, amorphous, and diamondlike carbon. Phys Rev B. 2001;64(7):075414.

[100] Cuesta A, Dhamelincourt P, Laureyns J, Martinezalonso A, Tascon JMD. RAMAN MICROPROBE STUDIES ON CARBON MATERIALS. Carbon. 1994;32(8):1523-32.

[101] Guo WM, Xiao HN, Zhang GJ. Kinetics and mechanisms of non-isothermal oxidation of graphite in air. Corrosion Sci. 2008;50(7):2007-11.

[102] Zhu ZH, Lu GQ, Finnerty J, Yang RT. Electronic structure methods applied to gas-carbon reactions. Carbon. 2003;41(4):635-58.

[103] Hahn JR. Kinetic study of graphite oxidation along two lattice directions. Carbon. 2005;43(7):1506-11.

[104] Sanchez A, Mondragon F. Role of the epoxy group in the heterogeneous CO2 evolution in carbon oxidation reactions. J Phys Chem C. 2007;111(2):612-7.

[105] Sendt K, Haynes BS. Density functional study of the chemisorption Of O-2 on the zig-zag surface of graphite. Combust Flame. 2005;143(4):629-43.

[106] Zavodinskii VG, Mikhailenko EA. Modeling of carbon combustion in molecular and atomic oxygen. Combust Explos & Shock Waves. 2006;42(3):247-53.

[107] Smith IW. The combustion rates of coal chars: A review. Proc Combust Inst. 1982;19:1945-065.

[108] Gulbransen EA, Andrew KF. REACTIONS OF ARTIFICIAL GRAPHITE - KINETICS OF OXIDATION OF ARTIFICIAL GRAPHITE AT TEMPERATURES OF 425-DEGREES-C TO 575-DEGREES-C AND PRESSURES OF 015 TO 98 CM. OF MERCURY OF OXYGEN. Industrial Eng Chem. 1952;44(5):1034-8.
[109] Blyholder G, Eyring H. KINETICS OF GRAPHITE OXIDATION. J Phys Chem. 1957;61(5):682-8.
[110] Marsh H, Ohair TE, Reed R. OXIDATION OF CARBONS AND GRAPHITES BY ATOMIC OXYGEN AN ELECTRON MICROSCOPE STUDY OF SURFACE CHANGES. Transactions of the Faraday Society. 1965;61(506P):285-93.
[111] Otterbei.M, Bonnetai.L. REACTION OF CARBON WITH ATOMIC OXYGEN. Carbon. 1969;7(5):539-54.
[112] Sendt K, Haynes BS. Density functional study of the chemisorption Of O-2 on the armchair surface of graphite. PROCEEDINGS OF THE COMBUSTION INSTITUTE. 2004;30:2141-9.
[113] Carlsson JM, Hanke F, Linic S, Scheffler M. Two-Step Mechanism for Low-Temperature Oxidation of Vacancies in Graphene. Phys Rev Let. 2009;102(16):166104.
[114] Chen N, Yang RT. Ab initio molecular orbital study of the unified mechanism and pathways for gas-carbon reactions. J Phys Chem A. 1998;102(31):6348-56.
[115] Frankcombe TJ, Smith SC. On the microscopic mechanism of carbon gasification: A theoretical study. Carbon. 2004;42(14):2921-8.
[116] Lee SM, Lee YH, Hwang YG, Hahn JR, Kang H. Defect-induced oxidation of graphite. Phys Rev Let. 1999;82(1):217-20.
[117] Incze A, Pasturel A, Chatillon C. Oxidation of graphite by atomic oxygen: a first-principles approach. Surf Sci. 2003;537(1-3):55-63.
[118] Allouche A, Ferro Y. Dissociative adsorption of atmospheric molecules at vacancies on the graphite (0001) surface of samples exposed to plasma. JOURNAL OF NUCLEAR MATERIALS. 2006;363:117-21.
[119] Backreedy R, Jones JM, Pourkashanian M, Williams A. A study of the reaction of oxygen with graphite: Model chemistry. FARADAY DISCUSSIONS 2001;119:385-94.
[120] Zhu ZH, Finnerty J, Lu GQ, Yang RT. A comparative study of carbon gasification with O-2 and CO2 by density functional theory calculations. Energy Fuels. 2002;16(6):1359-68.
[121] Domingo-Garcia M, Lopez-Garzon FJ, Perez-Mendoza M. Modifications produced by O-2 plasma treatments on a mesoporous glassy carbon. Carbon. 2000;38(4):555-63.
[122] Sohda Y, Tanenbaum DM, Turner SW, Craighead HG. Fabrication of arrayed glassy carbon field emitters. J Vac Sci Technol B. 1997;15(2):343-8.
[123] Tallant DR, Parmeter JE, Siegal MP, Simpson RL. THE THERMAL-STABILITY OF DIAMOND-LIKE CARBON. Diamond and related materials. 1995;4(3):191-9.
[124] Yanezlimon JM, Ruiz F, Gonzalezhernandez J, Chao BS, Ovshinsky SR. LOW-TEMPERATURE CRYSTALLIZATION OF SPUTTERED CARBON-FILMS. J Appl Phys. 1995;78(5):3015-9.
[125] Krasheninnikov AV, Banhart F. Engineering of nanostructured carbon materials with electron or ion beams. Nat Mater. 2007;6(10):723-33.

[126] Takai K, Enoki T. Fabrication of graphitic nanowire structure by electron beam lithography. PHYSICA E-LOW-DIMENSIONAL SYSTEMS & NANOSTRUCTURES. 2007;40(2):321-3.
[127] Lu X, Huang H, Nemchuk N, Ruoff RS. Patterning of highly oriented pyrolytic graphite by oxygen plasma etching. Appl Phys Let. 1999;75(2):193-5.
[128] Youn SW, Takahashi M, Goto H, Maeda R. Microstructuring of glassy carbon mold for glass embossing - Comparison of focused ion beam, nano/femtosecond-pulsed laser and mechanical machining. Microelectron Eng. 2006;83(11-12):2482-92.
[129] Choi S, Park H, Lee S, Koh KH. Fabrication of graphite nanopillars and nanocones by reactive ion etching. Thin Solid Films. 2006;513(1-2):31-5.
[130] Du RB, Ssenyange S, Aktary M, McDermott MT. Fabrication and Characterization of Graphitic Carbon Nanostructures with Controllable Size, Shape, and Position. Small. 2009;5(10):1162-8.
[131] Hou PX, Liu C, Cheng HM. Purification of carbon nanotubes. Carbon. 2008;46(15):2003-25.
[132] Tan PH, Dimovski S, Gogotsi Y. Raman scattering of non-planar graphite: arched edges, polyhedral crystals, whiskers and cones. Philos Trans R Soc Lond Ser A-Math Phys Eng Sci. 2004;362(1824):2289-310.
[133] Wang WH, Lin YT, Kuo CT. Nanofabrication and properties of the highly oriented carbon nanocones. DIAMOND AND RELATED MATERIALS. 2004;14(3-7):907-12.
[134] Taflove A, Hagness SC. Computational electrodynamics : the finite-difference time-domain method. 3 ed. Boston: Artech House 2005.
[135] Borghesi A, Guizetti G. Graphite. In: Palik ED, ed. *Handbook of optical constants of solids*. Orlando: Academic press 1991.
[136] Ausman LK, Schatz GC. Whispering-gallery mode resonators: Surface enhanced Raman scattering without plasmons. J Chem Phys. 2008;129(5):10.
[137] Ward AD, Zhang M, Hunt O. Broadband Mie scattering from optically levitated aerosol droplets using a white LED. Opt Express. 2008;16(21):16390-403.
[138] Michel B, Henning T, Jäger C, Kreibig U. Optical extinction by sperical carbonaceous particles. Carbon. 1999;37:391-400.
[139] Keller A, Loepfe M, Nebiker P, Pleisch R, Burtscher H. On-line determination of the optical properties of particles produced by test fires. FIRE SAFETY JOURNAL. 2004;41(4):266-73.
[140] Hull P, Shepherd I, Hunt A. Modeling light scattering from Diesel soot particles. Appl Optics. 2004;43(17):3433-41.
[141] Gu MX, Pan LK, Tay BK, Sun CQ. Atomistic origin and temperature dependence of Raman optical redshift in nanostructures: a broken bond rule. J Raman Spectrosc. 2007;38(6):780-8.
[142] Arora AK, Rajalakshmi M, Ravindran TR, Sivasubramanian V. Raman spectroscopy of optical phonon confinement in nanostructured materials. J Raman Spectrosc. 2007;38(6):604-17.
[143] Puech P, Puccianti F, Bacsa R, Arrondo C, Monthioux M, Bacsa W, et al. Thermal transfer in SWNTs and peapods under UV-irradiatlon. Phys Status Solidi B-Basic Solid State Phys. 2007;244(11):4064-8.
[144] Pathak S, Shenoy VB. Size dependence of thermal expansion of nanostructures. Phys Rev B. 2005;72(11):113404.

[145] Yin Y, Walsh AG, Vamivakas AN, Cronin SB, Stolyarov AM, Tinkham M, et al. Tunable resonant Raman scattering from singly resonant single wall carbon nanotubes. IEEE J Sel Top Quantum Electron. 2006;12(6):1083-90.
[146] Maher RC, Cohen LF, Gallop JC, Le Ru EC, Etchegoin PG. Temperature-dependent anti-Stokes/Stokes ratios under surface-enhanced Raman scattering conditions. J Phys Chem B. 2006;110(13):6797-803.
[147] Katumba G, Mwakikunga BW, Mothibinyane TR. FTIR and Raman Spectroscopy of Carbon Nanoparticles in SiO2, ZnO and NiO Matrices. Nanoscale Res Lett. 2008;3(11):421-6.
[148] Dresselhaus MS, Dresselhaus G, Saito R, Jorio A. Raman spectroscopy of carbon nanotubes. Phys Rep-Rev Sec Phys Lett. 2005;409(2):47-99.
[149] Pimenta MA, Gomes AP, Fantini C, Cancado LG, Araujo PT, Maciel IO, et al. Optical studies of carbon nanotubes and nanographites. PHYSICA E-LOW-DIMENSIONAL SYSTEMS & NANOSTRUCTURES. 2006;37(1-2):88-92.
[150] Cancado LG, Pimenta MA, Neves BRA, Medeiros-Ribeiro G, Enoki T, Kobayashi Y, et al. Anisotropy of the Raman spectra of nanographite ribbons. Phys Rev Let. 2004;93(4): 047403.
[151] Zhang YY, Son H, Zhang J, Kong J, Liu ZF. Laser-heating effect on Raman spectra of individual suspended single-walled carbon nanotubes. J Phys Chem C. 2007;111(5):1988-92.
[152] Stanmore BR, Brilhac JF, Gilot P. The oxidation of soot: a review of experiments, mechanisms and models. Carbon. 2001;39(15):2247-68.
[153] Vander Wal RL, Yezerets A, Currier NW, Kim DH, Wang CM. HRTEM Study of diesel soot collected from diesel particulate filters. Carbon. 2007;45(1):70-7.
[154] Du ZY, Sarofim AF, Longwell JP, Mims CA. KINETIC MEASUREMENT AND MODELING OF CARBON OXIDATION. Energy Fuels. 1991;5(1):214-21.
[155] Oehrlein GS. Reactive Ion Etching. In: Rossnagel SM, Cuomo JJ, Westwood WD, eds. *Handbook of plasma processing technology*. New Jersey: Noyes Publications 1990:196-232.
[156] Campion A, Kambhampati P. Surface-enhanced Raman scattering. Chem Soc Rev. 1998;27(4):241-50.
[157] Hagglund C, Zach M, Kasemo B. Enhanced charge carrier generation in dye sensitized solar cells by nanoparticle plasmons. Appl Phys Let. 2008;92(1):013113.